

T
D65-89
SHR

**CHARACTERIZATION OF InGaAsP
SUPERLATTICE SYSTEMS USING ROCKING
CURVE SIMULATIONS**

A THESIS

*submitted in fulfilment of the
requirements for the award of the degree*

of

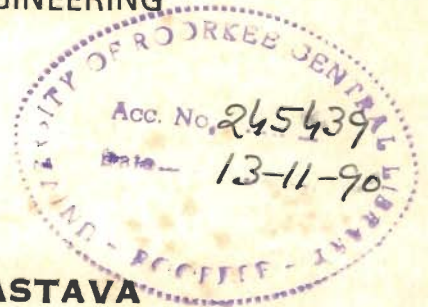
DOCTOR OF PHILOSOPHY

in

ELECTRONICS AND COMPUTER ENGINEERING

By

MAHESH CHANDRA SHRIVASTAVA



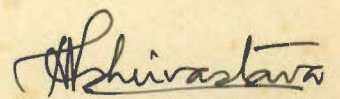
DEPARTMENT OF ELECTRONICS AND COMPUTER ENGINEERING
UNIVERSITY OF ROORKEE
ROORKEE-247 667 (INDIA)

AUGUST, 1989

CANDIDATE'S DECLARATION

I hereby certify that the work which is being presented in the thesis entitled **CHARACTERIZATION OF InGaAsP SUPERLATTICE SYSTEMS USING ROCKING CURVE SIMULATIONS** in fulfilment of the requirement for the award of the Degree of Doctor of Philosophy, submitted in the Department of **ELECTRONICS AND COMPUTER ENGINEERING** of the University of Roorkee, Roorkee is an authentic record of my own work carried out during a period from 18.10.1985 to 1 .8.1989 under the supervision of Dr. S. Swaminathan.

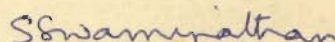
The matter embodied in this thesis has not been submitted by me for the award of any other Degree.


(M.C. SHRIVASTAVA)

Candidate's Signature

This is to certify that the above statement made by the candidate is correct to the best of my knowledge.

Date : 10-8-1989


(DR. S. SWAMINATHAN)

Reader,
Electronics & Computer Engg. Deptt.,
University of Roorkee,
ROORKEE

Signature(s) of Supervisor's

The candidate has passed the Viva-Voce examination held on
at The thesis is recommended for award of the Ph.D.
Degree.

Signature of Guide/s

Signature of External Examiners

ABSTRACT

Semiconductor superlattices and quantum-well heterostructures form an important class of electronic and optoelectronic materials since the properties of these layered structures are in many ways superior to those of bulk materials. While most superlattices and quantum-well heterostructures are grown using lattice-matched materials, structures composed of lattice^{mismatched} heterolayers are also of considerable interest since the loosening of the lattice-matching constraint allows increased flexibility in choosing constituent materials.

Although strained-layer superlattices (SLS) were first studied in the early 1970's, a significant fraction of strained-layer work has occurred in the past years. Comprehensive reviews of strained-layer structures in several different semiconductor material systems are available. Progress in the fabrication of pseudomorphic semiconductor structures has led to the development of photoexcited lasers, quantum-well injection lasers, light-emitting diodes, photodetectors and high electron mobility transistors, which utilize strained layers. Although electronic and optoelectronic devices often utilize SLS quantum-well heterostructures, studies of pseudomorphic material properties tend to emphasize on superlattice structures composed of multiple interacting strained layers. In properly designed strained-layer structures, the mismatched layer is so thin that the difference in lattice constants of the constituent materials is accommodated by elastic strain rather than by the generation of misfit dislocations. Thus, strained-layer structures of high crystalline quality can be fabricated from semiconductors differing significantly in their bulk lattice constants, provided layer thicknesses do not exceed strain-dependent critical values. Variety of epitaxial growth methods like LPE, VPE, MOCVD, MBE are available for fabrication of high quality structures.

Characterization of grown SLS is possible with optical and electrical measurements, transmission electron microscopy, and double crystal X-ray diffraction, etc. Double crystal X-ray diffraction is a nondestructive method. The rocking curves obtained experimentally can not give all the necessary and required structural details of the individual layers. If the SLS structures undergoes any thermal treatment, diffusion of impurity, ion-implantation etc., then a knowledge of the effects of such processes near the interface is important. Also these processes cause disordering of the SLS structures due to intermixing.

The use of X-ray double crystal diffraction technique in characterizing multilayer structure by means of experimental rocking curves is, however, complicated since the rocking curves in general are of complex nature in which there is no longer one-to-one correlation between diffraction peaks and individual layers in the structure. This problem is overcome by using dynamical scattering theory to generate simulated rocking curves based on an assumed material structure. The theoretical and experimental rocking curves are then matched by an iterative process whereby the assumed distribution of strain in the layers is modified until a good fit is obtained with the experimental data.

A careful study of existing literature shows that kinematical theory as well as dynamical theory of X-ray diffraction are two well known models based on which rocking curves can be simulated. The kinematical theory model has been used by a number of workers in view of its simplicity, while very few have worked with dynamical theory and no dynamical treatment have been used for the study of impurity diffused or ionimplanted SLS. The kinematical theory, however, is not applicable to heteroepitaxial layer or implanted layers with thicknesses that are a significant fraction of the extinction distance. The kinematical theory ignores extinction effects. When the reflecting power is more than about 6% the kinematical theory is not suitable.

Keeping in view all these points in the present studies, a dynamical theory has been preferred. Two dynamical models are presented. One is based on Takagi-Taupin's derivation and the other one based on Abeles' matrix method. In the simulation, a one dimensional strain variation is assumed normal to the sample surface i.e. the epilayers are elastically strained under a tetragonal distortion and are lattice-matched in the plane of the sample surface. For this type of unidirectional strain variation the well known Takagi-Taupin equations have been simplified and solved for epilayers of SLS structure, to give the ratio of the diffracted to incident beam amplitudes. For the calculation of layer reflectivity the epilayers in the SLS structure is divided into thin uniform laminae each of constant lattice-parameter and the reflectivity calculated by starting at the substrate and working upwards through each layer to the top layer. Finally rocking curves were convoluted with the reference crystal rocking curve. Some illustrative examples of simulated rocking curves using different combinations of composition, thickness, and number of periods of SLS structures have been shown. Further rocking curves of a number of SLS experimental specimens namely InGaAs/GaAs, InGaAs/InP, and GaAsP/GaP reported in the literature have been simulated and a comparison is made. Initial data from experimental rocking curves were used to calculate rocking curves for SLS structure. The input data are slightly adjusted about their initial values until a reasonable fit with experimental curve is achieved. For the initial data a knowledge of thickness, number of periods, mismatch variation of layers within each period is required. These can be obtained from SLS growth conditions. From such a comparison an accurate assessment of composition, mismatch, thickness of period and number of molecular layers have been achieved.

The simulation technique has also been successfully applied to characterize thermally annealed and Zn diffused disordered InGaAs/GaAs SLS. For thermally

annealed super-lattices the composition in the real space, assuming a simple linear diffusion mechanism in a single well has been considered while for Zn diffused disordered superlattice the interstitial and substitutional mechanism has been used to calculate the composition profiles.

Further, modification of this technique have been used to assess the strain/damage depth distribution in an ionimplanted SLS structure. In this approach the strained-material is modeled as a series of laminae each with a perpendicular strain and damage assumed uniform. Damage is assumed as a random displacement of atoms from their lattice sites. This was taken to have the form of a spherically symmetric Gaussian function with standard deviation U . The lattice damage and additional strain in Beryllium implanted GaAsP/GaP SLS structure have been assessed by comparison of an experimental with simulated rocking curve.

In the Abeles' matrix method a 2×2 matrix is described to compute reflection and transmission of light by plane layered media in which the refractive index is isotropic and varies only in the direction normal to the layers. The method can be used to find solutions for dynamical theory of X-ray diffraction if variation of X-ray refractive index normal to any sets of Bragg planes of interest is known. In the present thesis Abeles' dynamic approach has been successfully applied to simulate rocking curves for the SLS structures. Rocking curves simulated for different composition, thickness of epilayers, and number of periods of SLS structures have been studied extensively and compared with those simulated by Takagi-Taupin's model. Comparison showed that the Abeles' approach need less computation time and gives more sharp peaks. The approaches of Takagi-Taupin and Abeles' were both used to simulate rocking curves for an experimental InGaAs/GaAs SLS structure. The satellite peak intensities

thus calculated were compared with those calculated from kinematical approach and experimental data. A three crystal X-ray scan of InGaAs/InP superlattice structure reported in the literature have also been simulated using the Abeles-Takagi approach and a comparison is made with kinematical step model. On the basis of the comparison final conclusions are made.

ACKNOWLEDGEMENTS

The author expresses his deep sense of gratitude and indebtedness to Dr.S.Swaminathan, Reader, Department of Electronics and Computer Engineering, University of Roorkee, Roorkee for his inspiring guidance, kind cooperation and invaluable help during the course of investigation, without which this work would not have been possible.

The author is highly thankful to Dr.R.Mitra, Professor and Head of Electronics and Computer Engineering Department, for his valuable suggestions.

The author is grateful to Dr.T.P.Pearsall, Dr.A.T.Macrauder of AT&T Bell Lab., and Dr.N.Holonyak Jr. of University of Illinois at Urbana-Champaign for their assistance in connection with the preparation of the thesis.

Thanks are due to Dr.C.R.Wie of State University of New York, for many helpful suggestions, and assistance in providing experimental rocking curve.

The author also wishes to thank Mr.O.P.Dubey, Mr.S.Tiwari, Mr.K.Valecha, and Mr.P.K.Bansal and friends who have directly or indirectly helped him in completing the task.

The author conveys his sincere thanks to the Government of Madhya Pradesh, and to the Director, S.G.S.Institute of Tech. & Science, Indore, for having sponsored his candidature under Quality Improvement Programme of Ministry of Human Resource Development, Government of India.

The author is thankful to Sri R.P.Singh for his neat and efficient typing of the manuscript.

Most of all the author wishes to express grateful thanks to his parents for their blessings, all members of his family especially to his wife Smt. Shail and children Rikki and Chinku for their extreme perseverance and encouragement.

CONTENTS

Page No.

	CANDIDATE'S DECLARATION	
	ABSTRACT	
	ACKNOWLEDGEMENTS	
	CONTENTS	
CHAPTER		
I	INTRODUCTION AND STATEMENT OF PROBLEM	
	1.1 Introduction	1
	1.2 Characterization methods	6
	1.3 Motivation for the present work	7
	1.4 Problem formulation	8
	1.5 Organization of the thesis	9
II	REVIEW OF METHODS OF GROWTH OF SUPERLATTICES	
	2.1 Introduction	11
	2.2 Growth of superlattice structures	12
	2.2.1 Compositional superlattices	14
	2.2.2 Doped superlattices	15
	2.2.3 Strained-layer superlattices	16
	2.3 Molecular beam epitaxy	17
	2.4 Metalorganic chemical vapour deposition	21
	2.5 Conclusion	25

III	REVIEW OF METHODS OF CHARACTERIZATION OF SUPERLATTICES	
	3.1 Introduction	26
	3.2 Photoluminescence	27
	3.3 Transmission electron microscopy	30
	3.4 Auger spectroscopy	34
	3.5 Raman scattering	37
	3.6 Rutherford back scattering	41
	3.7 X-Ray double crystal diffraction	43
	3.8 Discussions	49
IV	THEORY OF X-RAY DIFFRACTION	
	4.1 Introduction	51
	4.2 Kinematical theory of X-ray diffraction	53
	4.3 Bragg law and condition of diffraction	53
	4.4 Dynamical theory of X-ray diffraction	57
	4.4.1 The periodic complex dielectric constant	58
	4.4.2 Solutions of Maxwell's equations	61
	4.4.3 Boundary conditions for solutions of Maxwell's equations	68
	4.5 Pendellosung	70
	4.6 Rocking curve profile	72
	4.7 Distorted crystals	74
	4.8 Discussions	79

V	COMPUTER SIMULATION OF ROCKING CURVES AND THEIR COMPARISON WITH EXPERIMENTAL CURVES	
	5.1 Introduction	80
	5.2 Kinematical simulation	
	5.3 Dynamical simulation model	84
	5.3.1 Determination of structure factor	94
	5.3.2 Composition of x and y	95
	5.3.3 Dispersion corrections	96
	5.3.4 Effect of tetragonal distortion	99
	5.4 Comparison of experimental and simulated rocking curves	111
	5.5 Conclusions	117
VI	CHARACTERIZATION OF THERMALLY ANNEALED AND Zn DIFFUSED SUPERLATTICES FROM ROCKING CURVE SIMULATION METHOD	
	6.1 Introduction	119
	6.2 Disorder due to thermal annealing	121
	6.3 Rocking curve simulation	123
	6.4 Disorder due to Zn diffusion	125
	6.5 Rocking curve simulation for Zn diffused SLS	126
	6.6 Calculation from experimental rocking curves	128
	6.7 Chan's model calculation	129
	6.8 Conclusion	134
VII	EFFECTS OF IONIMPLANTATION ON SUPERLATTICES	
	7.1 Introduction	135
	7.2 Characterization methods	136

7.3	Rocking curve simulation	137
7.4	X-Ray rocking curve analysis	141
7.5	Conclusion	143
VIII	DYNAMICAL SIMULATION USING ABELES' MATRIX METHOD	
8.1	Introduction	144
8.2	Abeles' matrix method	145
8.3	Refractive index n for X-rays.	147
8.4	Abeles-Takagi model	149
8.5	Comparison of experimental and simulated rocking curves	154
8.6	Three crystal X-ray scan simulation	159
8.7	Conclusion	160
IX	GENERAL DISCUSSIONS AND CONCLUSIONS	163
	REFERENCES	168
	PUBLICATIONS	191

LIST OF FIGURES

1.1	Lattice constant variation with bandgap energy for various III-V alloys	2
1.2	Superlattice structure and superlattice buried device	4
2.1	Molecular beam epitaxy line diagram	18
2.2	Metalorganic chemical vapour deposition process diagram	23
3.1	Low-temperature excitonic photoluminescence spectrum measured in a strained InGaAs/GaAs MQW sample	29
3.2	Transmission electron microscope micrograph of a InGaAs/InP superlattice	33
3.3	Auger depth profile of a Zn diffused InGaAs/GaAs SLS structure	36
3.4	Raman spectrum of a strained layer superlattice InGaAs/AlGaAs	40
3.5	SLS backscattering spectra for 3MeV He incident along the $\langle 100 \rangle$ channeling and random directions as a function of Zn fluence (■) Before implant, (□) $1 \times 10^{13}/\text{cm}^2$, (+) $4 \times 10^{13}/\text{cm}^2$, (x) $8 \times 10^{13}/\text{cm}^2$, (o) $4 \times 10^{14}/\text{cm}^2$, (●) random.	42

3.6	A double crystal technique in the (+ -) or parallel setting	44
3.7	An experimental rocking curve of a InGaAs / GaAs SLS structure	46
4.1	Model of X-ray diffraction in kinematical treatment	52
4.2	Reflection sphere and Bragg plane	52
4.3	Construction of dispersion surface	65
5.1 to 5.4	Effect of increasing composition on the simulated rocking curves	85
5.5	Effect of increasing number of periods of a superlattice on simulated rocking curve	87
5.6	Effect of increasing well and barrier thicknesses of superlattice on simulated rocking curve	87
5.7	Comparison of experimental and kinematically simulated rocking curve of a InGaAs/GaAs SLS specimen	88
5.8	Comparison of experimental and kinematically simulated rocking curve of a InGaAs/GaAs SLS specimen	89

5.9	Schematic diagram of the dynamical X-ray scattering on superlattice. K_0 and K are incident and reflected wave vectors, and h is the scattering vector, Δ represents one period	92
5.10	Tetragonal distortion in a unit cell	100
5.11 to 5.14	Effect of increasing composition on the dynamically simulated rocking curves	104
5.15 to 5.19	Effect of increasing number of periods on the simulated rocking curves.	106
5.20 to 5.24	Effect of increasing number of periods on the simulated rocking curves when the well and barrier thicknesses are equal.	108
5.25 to 5.26	Comparison of experimental and dynamically simulated rocking curves of InGaAs/GaAs SLS	112
5.27 to 5.28	Comparison of experimental and dynamically simulated rocking curves of InGaAs/InP superlattices.	114
5.29	Comparison of experimental and dynamically simulated rocking curves of a GaAsP/GaP SLS	116
6.1	Composition/depth profile of a InGaAs/GaAs thermally annealed SLS	122

6.2	Comparison of experimental and dynamically simulated rocking curves of a thermally annealed InGaAs/GaAs SLS for 15h, 39h, 72h annealing at 850°C	124
6.3	Logoni and Kick-out mechanism of III-V semiconductor	124
6.4	Comparison of experimental and dynamically simulated rocking curves for Zn diffused InGaAs/GaAs SLS	127
6.5	Experimental rocking curves of a thermally annealed and Zn diffused InGaAs/GaAs SLS.	130
6.6	Evolution of satellite intensities as a function of the annealing time.	139
7.1	Comparison of experimental and dynamically simulated rocking curves of an Be implanted GaAsP/GaP SLS	139
7.2	Strain/damage depth profile for a Be implanted GaAsP/GaP SLS obtained from simulation	140
8.1 to 8.2	Effect of increasing composition on simulated rocking curves of InGaAs/GaAs SLS	152

8.3 to	Effect of increasing composition on simulated	
8.4	rocking curves of InGaAs/InP superlattice	153
8.5 to	Effect of well and barrier thickness variation	
8.6	on the simulated rocking curves of InGaAs/InP superlattices	154
8.7	Comparison of experimental results (full curve) with Abeles-Takagi method (broken curve) and Takagi-Taupin method (dotted curve) applied to the InGaAs/GaAs SLS	157
8.8	Comparison of experimental results (full curve) with Abeles-Takagi and Takagi-Taupin simulation methods applied to InGaAs/InP superlattice.	157
8.9	Comparison of experimental and simulated InGaAs/InP three crystal X-ray scan.	161

CHAPTER 1
INTRODUCTION AND PROBLEM FORMULATION

InGaAsP material system have, in recent years, found potential application as optoelectronic sources for low loss optical fibre transmission. This is due to fact that the attenuation of optical fibre is relatively low for sources emitting radiation in the spectral region 1.0-1.4 μm . Further such material systems have the advantage that it is possible to grow thin epitaxial layers on InP substrates with exact lattice match over a band gap region from 1.35 eV to 0.74 eV corresponding to wavelength range from 0.92 μm to 1.68 μm as shown in Figure 1.1. The boundaries joining the binary compounds give the ternary energy gap and lattice constant, while the quaternary field is indicated by the shaded region.

It has been observed that the presence of lattice mismatch between the substrate and epilayer gives rise to misfit dislocations at the interface [153]. Further more layers with dislocations that result from lattice mismatch have been found to have reduced luminescent efficiency in the region of dislocation [154]. It is therefore evident that the lattice matching across a heterojunction interface is essential for the development of efficient and reliable optoelectronic devices. For GaAs based systems the lattice matched alloy span the energy range from 1.42 eV to 1.91 eV [107].

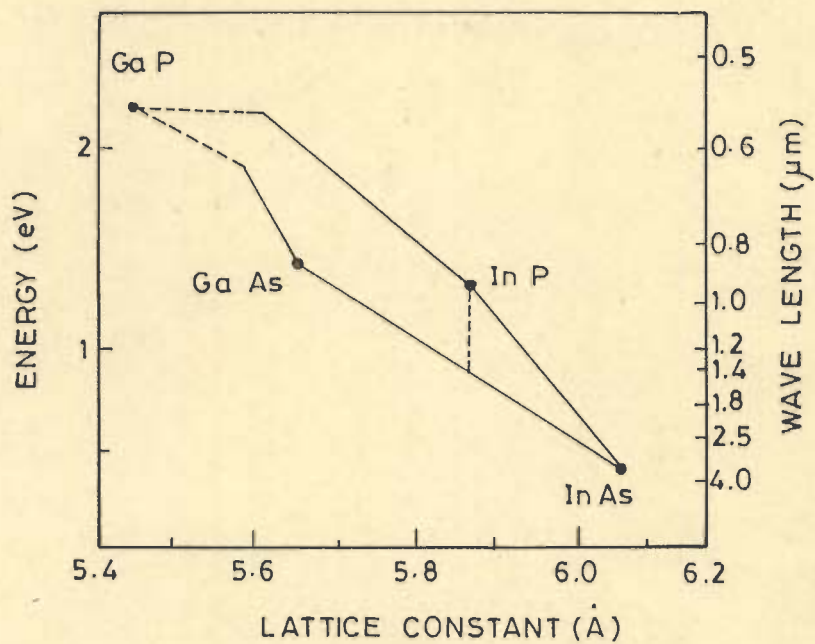


FIG. 1.1

Epitaxy has progressed from single layer growth on a substrate using liquid phase epitaxy, e.g. GaAs over GaAs substrate [107] to growth of extremely thin multilayers using more recently developed molecular beam epitaxy and metalorganic chemical vapour deposition techniques [107]. Epitaxial superlattices consist of multiple thin layers arranged in a periodic fashion one example is shown in Figure 1.2 where the superlattice period consist of two layers InGaAs and InP arranged over a substrate InP. Most of the early investigations concentrated on a limited number of material combinations for the growth of superlattices. The selection was limited by the number of material pairs with closely matched lattice parameters, e.g. GaAs/AlAs, InGaAs/InP. However, since the thickness of the individual layers in the superlattice are extremely small any lattice mismatch at the interface can be elastically accommodated by strain and the resulting structure called the strained-layer superlattice (SLS) has been found to have new and interesting properties. Biaxial tension/compression in such SLS can produce unique properties not found in lattice matched superlattice systems [102].

SLS structures can be grown from a wide variety of material systems. Recent interest in such structures has been motivated by their potential use in multijunction photovoltaic cell [31,36], photoexcited lasers [21], quantum-well injection lasers [89,90], lightemitting diodes [16,80],

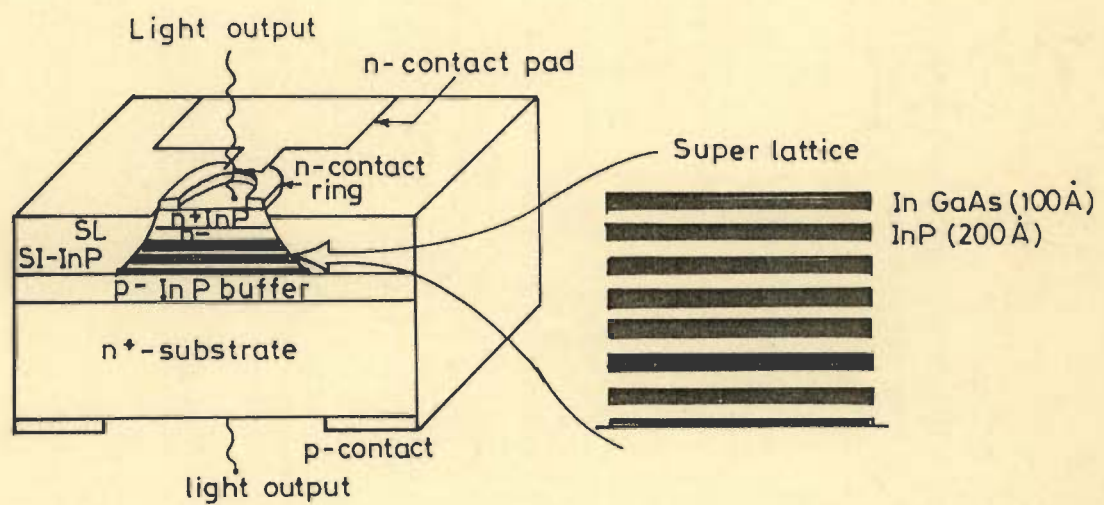


FIG. 1.2 SUPERLATTICE & SUPERLATTICE- BURIED DEVICE

photodetectors [8], and high-electron mobility transistors [119].

As far as growth of superlattices is concerned SLS is first studied in the early 1970s. A significant fraction of SLS work has occurred in the past few years. GaAs, InP, and GaP substrates have been used by many workers to grow InGaAsP SLS systems [11,15,101,109,114]. Molecular beam epitaxy (MBE) and metalorganic chemical vapour deposition (MOCVD), are the processes used to grow the superlattice structures [114,66,102]. With MBE it is just possible at least in the laboratory to spray a semiconductor wafer with just one layer of atoms at a time. This approach obviously guarantees a virtually perfect and uniform crystal structure [31,107].

Mechanical strain in an SLS can be introduced by alternate thin layers of materials whose crystal lattice differ in their atomic spacing. Within elastic limits adjacent layers contract or expand to match the atomic spacing of the substrate. It has been observed that compressive strain increases the band gap of an SLS layer, and the tensile strain decreases it [31]. Alloying a semiconductor alters its band gap and lattice constant. For example Gallium arsenide has a band gap of 1.4 eV, replacing some of the Gallium atoms with aluminium atoms creates the alloy GaAlAs which can have a band gap as high as 1.8 eV depending on

the concentration of aluminium. It is possible to create a graded alloy with a band gap that varies continuously from 1.4 eV to 1.8 eV. Such alloying ternaries like InGaAs, GaAsP, GaAlAs are used in the fabrication of superlattices.

During the superlattice-buried device fabrication these SLS structures undergo various processes such as thermal annealing, impurity diffusion, and ionimplantation. These processes change the superlattice composition. In other words, an $\text{In}_x\text{Ga}_{1-x}\text{As}/\text{GaAs}$ SLS after thermal annealing becomes $\text{In}_{x-y}\text{Ga}_{1-x+y}\text{As}/\text{In}_y\text{Ga}_{1-y}\text{As}$ alloy and this will change the SLS properties. This is because of interdiffusion of Ga from GaAs and In from $\text{In}_x\text{Ga}_{1-x}\text{As}$ across the interface. Similarly impurity diffusion and ionimplantation of superlattices also create disorder due to enhanced interdiffusion [28,29,84,85]. Such disordering due to diffusion and thermal annealing and ionimplantation of SLS structures has been studied in detail in this thesis.

1.2 CHARACTERIZATION METHODS

Superlattice structures are usually characterized after they undergo various fabrication processes. Number of characterization methods are present:

- (a) Photoluminescence (PL) spectrum can reveal band gap, compositional variation and disorder in the superlattice structure.

- (b) Superlattice epilayer thickness and structural perfection may be confirmed by TEM.
- (c) Auger electron spectroscopy can provide the compositional variation deep inside the superlattice.
- (d) Raman spectrum analysis can provide the information concerning the superlattice period and the individual layer width.
- (e) Rutherford back scattering can provide the concentration of the species at a certain depth and is useful to monitor lattice disorder produced by various implants.
- (f) X-ray double crystal diffraction can separate images of epilayers from the substrate thereby identifying the location of any defects. The technique also enables a very precise plot of the rocking curves which provides invaluable information about the assessment of the thickness, compositional variation in the epilayers and of their crystalline perfection. For superlattice structures complicated rocking curves are obtained. This is a nondestructive method and no sample preparation is required.

1.3 MOTIVATION FOR THE PRESENT WORK

Experimental X-ray double crystal diffraction method though a non-destructive method for the material characteri-

zation, however, can not provide details about the individual layer for a multilayer structure as in a superlattice structure. To assess the details regarding the number of monolayers, composition of each layer, thickness etc., theoretical calculation or computer simulation of experimental rocking curves is necessary.

There are two models on the basis of which rocking curves can be simulated, namely kinematical and dynamical theory of X-ray diffraction. Kinematical theory has been applied by a number of workers for the analysis of single epilayer [112,123], and for superlattices [124]. This theory has certain limitation and ignores extinction effects. Therefore in the present investigations dynamical theory has been used. No dynamical treatment has been applied to analyze the superlattice structure after they (SLS) undergo thermal annealing, Zn diffusion, and ionimplantation processes. In the present thesis effects of such processes on the SLS have been analyzed.

1.4 PROBLEM FORMULATION

The salient features of the present study may be stated as:

- (1) Develop a model on the basis of Takagi's dynamical theory of X-ray diffraction for the analysis of superlattice structure.

- (2) Modelling for thermally annealed and Zn diffused SLS structure and to simulate rocking curves for the disordered SLS, and to calculate the interdiffusion coefficient from the simulated rocking curves.
- (3) Modification of the model of case (1) for the assessment of strain/damage depth distribution in the case of an ionimplanted SLS structure and to simulate rocking curves.
- (4) Develop a model and simulate rocking curves for the SLS structure on the basis of Abeles' matrix method. This model is further used to simulate three crystals X-ray scan simulation of the superlattice structures.

1.5 ORGANIZATION OF THE THESIS

The thesis consists of nine chapters in all. The principal crystal growth methods like molecular beam epitaxy (MBE), metalorganic chemical vapour deposition (MOCVD) which are used to grow SLS structures have been reviewed in chapter two. There are various methods of SLS characterization e.g. Photoluminescence, Transmission electron microscopy, Auger electron spectroscopy, Raman scattering, Rutherford back scattering, and X-ray double crystal diffraction etc. A review of these methods is presented in chapter three.

Chapter four describes the kinematical and dynamical theory of X-ray diffraction, which are used to simulate

rocking curves. Simulation of rocking curves for various SLS specimens are generated by changing the composition, number of periods, and thicknesses of SLS structures. Both kinematical and dynamical simulations are presented in chapter five. Some of the experimental rocking curves which are reported in the literature have been simulated and their results are analyzed.

Chapter six describes the effects of thermal annealing and Zn diffusion in the InGaAs/GaAs SLS structures, rocking curves are simulated for thermally annealed and Zn diffused InGaAs/GaAs SLS. Interdiffusion coefficient of In-Ga has been obtained from such simulation studies [132] and compared with values calculated by analytical method [130,131]. Chapter seven also discusses the effects of ionimplantation on SLS. Strain/damage depth distribution for a Be implanted GaAsP/GaP SLS has been obtained by simulating rocking curves and achieving a close fit to the experimental one [133]. In chapter eight another dynamical simulation model based on Abeles' matrix method have been developed to simulate superlattice rocking curves, and also to simulate three crystal X-ray scan. Few SLS specimens rocking curves were generated. An experimental rocking curve, and a three crystal X-ray scan of InGaAs/InP superlattice have been analyzed. General discussion and conclusions arising out of the results obtained from the various studies conducted on the SLS, are made in chapter nine.

CHAPTER 2
REVIEW OF METHODS OF GROWTH
OF SUPERLATTICES

2.1 INTRODUCTION

Technology projection often emphasise materials as a particularly fertile area for potential revolutionary developments. Further, elaboration usually refers to new "materials" in the expectation that new phenomena would result. Historically this concept has been proven many times, and today a promising source of new materials based to a large extent on epitaxial growth is emerging. This is the area of complex, multilayer/multimaterial epitaxial structures. This also includes compositional superlattices which find wide application as photodetectors, laser sources for fibreoptic communications.

Epitaxy has progressed from single layer growth on a substrate of same composition to multiple layer growth over a substrate with different compositions. In recent years efforts to reduce the dimensions of semiconductor devices and circuits demanded tighter control over epitaxial processes. Junction abruptness became an important measure of the capabilities of an epitaxial growth technique. It has been found that extremely thin layers of good crystalline quality can be grown by molecular beam epitaxy or metalorganic chemical vapour deposition methods. On the rapid development of MBE with its inherent capability for deposition control at the monolayer level provides the growth of a new generation of multilayer

structures. MOCVD which has almost the same degree of deposition as MBE but greater throughput, is also a powerful technique for growth of SLS structures with abrupt transitions. In the present chapter different types of superlattices and growth methods have been reviewed.

2.2 GROWTH OF SUPERLATTICE STRUCTURES

Optoelectronic semiconductor devices are constructed using hundreds or thousands of superthin layers. In recent years, however, new techniques of semiconductor crystal growth have given engineers and physicists extremely precise control over layer thickness. Alternate monolayer deposition of $(\text{AlAs})_1 (\text{GaAs})_1$ layered structure grown by MBE [98], and $(\text{InAs})_1 (\text{GaAs})_1$ grown by MOCVD [42] have been reported. Monolayer growth by MOCVD is achieved by decreasing the deposition rate and by rapidly changing the gas composition. This layered structure of $(\text{InAs})_1 (\text{GaAs})_1$ has average alloy composition $\text{In}_{0.5}\text{Ga}_{0.5}\text{As}$ which is closely matched to InP [42]. To accomplish alternate monolayer growth, the deposition rate must be small. Superlattices grown by alternate deposition of monolayers of GaAs and AlAs have also been reported [98]. Similarly strained-layer superlattices of InGaAs/GaAs [66], GaAsP/GaP [49] have also been grown using MBE and MOCVD details of which are as listed in table 2.1.

Table 2.1 : SUPERLATTICES

Structure	Prepara-	Application	Reference
<u>Compositional</u>			
$\text{Ga}_x\text{Al}_{1-x}\text{As}/$ GaAs	MBE MOCVD	Multiple Quantum well lasers, modulation doped structures	[25,83,108, 148]
InAs/GaSb	MBE	Semiconductor/semi- metal transition	[120]
$\text{Ga}_x\text{In}_{1-x}\text{As}/$ InP	MOCVD	Enhanced mobility	[15,44]
<u>Doping</u>			
GaAs(n,p)	MBE	Tunable properties, increased recombination life time	[110]
GaAs(i)/ $\text{Ga}_x\text{Al}_{1-x}\text{As}(n,p)$	MBE	Mobility enhancement (electron and holes)	[110]
<u>Strained layer</u>			
$\text{In}_x\text{Ga}_{1-x}\text{As}/$ GaAs	MBE MOCVD	High electron mobi- lities	[8,66,114]
$\text{GaAs}_x\text{P}_{1-x}/\text{GaP}$	MOCVD	Band gap allows for easy optical cha- racterization	[47,91]
$\text{Ga}_x\text{As}_{1-x}\text{P}/$ GaAs	MOCVD	Green solid state lasers, alternate colour LEDs	[49]

2.2.1 COMPOSITIONAL SUPERLATTICES

Compositional semiconductor superlattices were recognized as early as 1970 to offer potentially useful electronic properties [107]. These structures have justifiably been considered to be new composition of matter, i.e. their properties are not simple interpolations between the properties of the constituent layers. This is the feature that motivates much of the research on superlattices.

Most of the early studies on the compositional superlattices were based on GaAs/AlAs because of the small lattice mismatch [62,84] of this favourable combination. These studies have led to useful electronic device developments such as the modulation doped superlattices [83] in which only the aluminium containing layers of a GaAs/ $\text{Al}_x\text{Ga}_{1-x}\text{As}$ superlattice are doped. Because of the band structure at the interfaces, the carriers originating through ionization of the dopant atoms can lower their potential energy by "spilling over" into the undoped GaAs layers where their mobility is not degraded by scattering from the ionized impurities, which remain in the Al-rich layers. These structures exhibit exceptionally high electron mobilities [136], especially at lower temperatures (77K), where ionized impurity scattering is the dominant scattering mechanism.

Quantization effects which occur when the alternating layer dimensions become small form, the basis for special electronic and optical devices based on superlattices. Such effects are utilized in the multiple quantumwell laser to obtain lower threshold current densities and a reduced sensitivity of this parameter to temperature [58]. These devices are prepared from superlattices containing multiple GaAs and AlAs or GaAlAs layers grown by either MBE or MOCVD.

2.2.2 DOPED SUPERLATTICES

Both theoretical and experimental development of doping superlattices has been pioneered in the Federal Republic of Germany. These structures offer the promise of unique electrical and optical characteristics resulting from their special energy band configurations, and they are not subject to the restrictions imposed by the necessity of lattice matching in compositional superlattices [83]. With doping superlattices the special separation of electrons and holes due to the periodic space charge potential of the ionized impurities leads to the concept of an "indirect gap in real space". The effective width of the bandgap can be tuned by varying the nonequilibrium carrier concentration, and, since the hole and electron states are more or less separated in local space, the

recombination lifetime of excess carriers is increased. Such properties are promising for development of tunable infrared light sources operating in the desirable region. Devices fabricated in GaAs with 21 alternating 25 nm thick n-and p-layers exhibit optical gain with tunability for matching to the transmission characteristics of optical fibre [107]. Most of the results to date have been obtained with doping superlattices formed from the III-V compound semiconductors using MBE and MOCVD growth techniques.

2.2.3 STRAINED-LAYER SUPERLATTICES

The necessity of lattice matching has restricted the number of superlattice structures available for investigation. However, if the layers are kept sufficiently thin, then the mismatch can be accommodated elastically. The resulting structures are called strained-layer superlattices (SLS). SLS can be grown from a wide variety of material systems (Table 2.1). The capability of working with poorly lattice matched systems provides another degree of freedom to the device designer. Thus the optical properties, transport characteristics, and structural properties can be varied independently. In addition the strain itself can distort or modify the band structure. Examples of SLS include $\text{GaAs}_x\text{P}_{1-x}/\text{GaAs}$ [49], which are deposited by MOCVD. They are of interest for potential green solid-state lasers and alternate colour light emitting

diodes. $\text{Ga}_x\text{In}_{1-x}\text{As}/\text{GaAs}$ SLS deposited by MBE are being investigated for high speed or high frequency device applications [64]. A strained superlattice buffer layer (SSBL) composed of short period $\text{InGaAs}/\text{GaAs}$ SLS has been introduced into a lattice-matched $\text{AlGaAs}/\text{GaAs}$ system in order to reduce the internal stress [48,77]. A high quantum efficiency, a small cavity loss, and high output power operation have been achieved in narrow ridge-waveguide 770 nm graded index separate confinement heterostructure laser diode with the SSBL.

GaAsP/GaP SLS grown by MOCVD have been used to produce optical interference filters and an integrated high reflector/photodiode detector. Thus the SLS structures grown with MBE and MOCVD growth techniques are of wide interest in optoelectronic devices. In brief MBE and MOCVD growth techniques are described, in the next section.

2.3 MOLECULAR BEAM EPITAXY

Molecular beam epitaxy is a comparatively recent process for epitaxial growth of thin single crystal semiconductor structures in which an ultrahigh vacuum is used. With MBE, the thickness of crystalline layers can be precisely controlled down to a few angstrom. Layer composition can be varied and semiconductor structures can be produced that are different or impossible to make by other means.

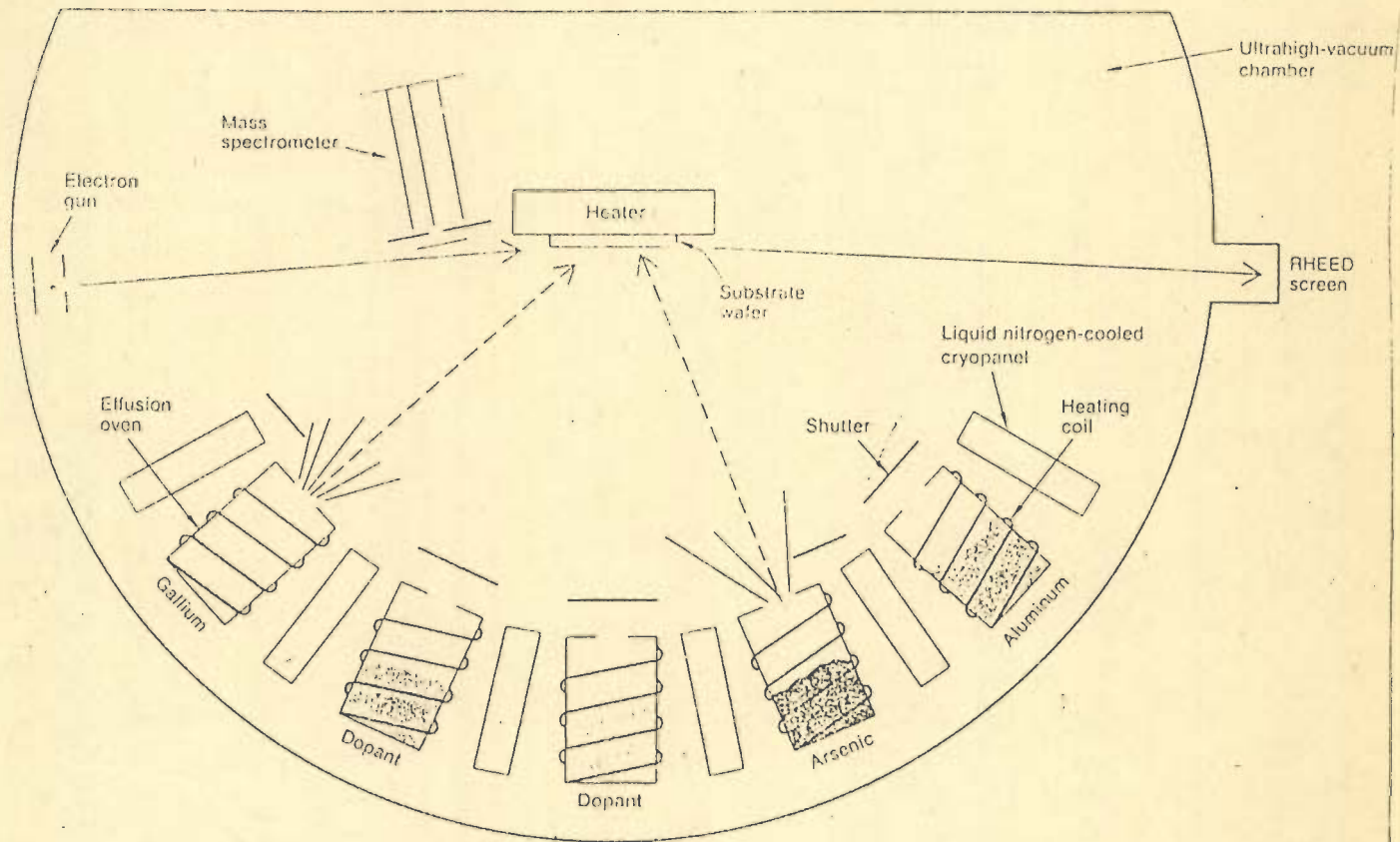


FIG. 2.1 MBE

The film constituents are deposited on a substrate crystal from atomic or molecular streams, or beams. These beams are created when the required elements are heated in effusion ovens each with an opening facing the substrate wafer. Effusion ovens are same in number as there are elements to be incorporated into the crystal structure as shown in Figure 2.1. For GaAs devices, ovens for gallium, for arsenic and for each of the doping elements are needed. The beams are turned on and off or their intensity is varied, as necessary to create the desired layer structure. As elements from the beams deposit on the substrate, the atoms and molecules take up the crystal structure of the material below. The deposited material in other words is epitaxial hence, the process name molecular beam epitaxy. It is important in MBE that the process be carried out in as perfect a vacuum as possible to prevent unwanted impurities from being incorporated into the crystal structure. Ultra high vacuum is therefore used for this purpose.

MBE makes it possible to grow high quality single crystal Schottky barriers, nanoalloyed ohmic contacts, insulating layers, and semi-insulating layers all with the same crystal lattice structure as the substrate [107]. The layers can be grown as part of a continuous process without removal of the wafer from the MBE chamber. Recently multiple interleaved layers of GaAs and AlAs and of GaAs and AlGaAs, InGaAs, GaAsP formed by MBE yielded matched

and SLS crystals.

In the growth of GaAs epitaxial layers, gallium atoms and arsenic molecules strike a GaAs substrate surface, which is heated to 500° to 600°C. All the gallium atoms adhere to the surface, but if there is an excess of arsenic, only one arsenic atom remains on the surface for each gallium atom deposited. As a result, the growing layer is stoichiometric maintaining a 1:1 ratio of gallium atoms to arsenic atoms. The flux of group III atoms thus determines the epitaxial layer growth rate [110] and that flux depends largely upon the temperature within the effusion oven for the group III element. For GaAs, the gallium beam intensity is usually adjusted to yield 1 to 3 μm of epitaxial growth per hour [107]. This requires a gallium flux of about 10^{15} atoms $\text{cm}^{-2}\text{s}^{-1}$.

For growing AlGaAs on GaAs an additional effusion oven that contains aluminium is employed. All of the Al and Ga atoms that impinge upon the substrate surface adhere, so that the ratio of Al to Ga in solid is the same as the flux ratio of Al to Ga in the effusion beam [137]. The flux of molecules or atoms emitted at the effusion oven orifice depends primarily on the vapour pressure of the element within the oven and thus upon the oven temperature, and upon the molecular weight of the effusion species.

The mechanism controlling the growth of GaAs and related alloys have been studied by modulated molecular beam techniques and by reflection high energy electron diffraction RHEED [137]. The growth of superlattices using MBE have been widely reported in the literature. Quantum well structures for example have been grown on (100) oriented GaAs substrate using computer controlled shutter operation [107]. The growth rate of the GaAs was maintained at $0.8 \mu\text{m/h}$ for structures grown here the growth temperature is within the range $550 \pm 10^\circ\text{C}$. The ratio of V to III group was 30 to maintain an arsenic stabilized surface for both GaAs and InGaAs. Similarly many single and isolated InGaAs/GaAs and other quantum wells and SLS were grown are reported [1,8,32,41,43].

2.4 METALORGANIC CHEMICAL VAPOUR DEPOSITION

Generally, growth is achieved by introducing metered amounts of group III alkyls and the group V hydrides into a quartz reaction tube which contains a substrate placed on an RF-heated carbon susceptor. The hot susceptor has a catalytic effect on the decomposition of the gaseous products and the growth therefore primarily takes place at this hot surface. At the working pressure of between 0.1 to 0.5 atm with the gas flow rate 10-20 lt per minute. The gas velocities in the neighbourhood of the susceptor are between 1 and 15 cm per second, with the result that

the gas flow is laminar. The growth process is schematically shown in Figure 2.2.

In this process, a stagnant boundary layer [107] which is adjacent to the growth surface exist. Within this layer, concentration changes occur only by diffusion. Existence of this layer has been experimentally verified [47]. The growth by MOCVD can be explained as follows:

- (1) The gas molecules diffuse across the stagnant layer to the substrate surface.
- (2) At the hot surface the metal alkyls and hydrides are decomposed, thus producing the group III and group V elemental species.
- (3) The elemental species move on the hot surface until they find an available lattice site where growth then occurs.

Any of these three processes can limit the growth rate but in general low-pressure MOCVD takes place under conditions where diffusion across the stagnant layer is the rate limiting step. If (2) and (3) limits the growth then the growth rate is strongly temperature dependent. However, where diffusion dominates, the growth rate is virtually independent of temperature and is controlled simply by the rate of arrival of the growing species at the solid-vapour interface. This arrival rate is in turn

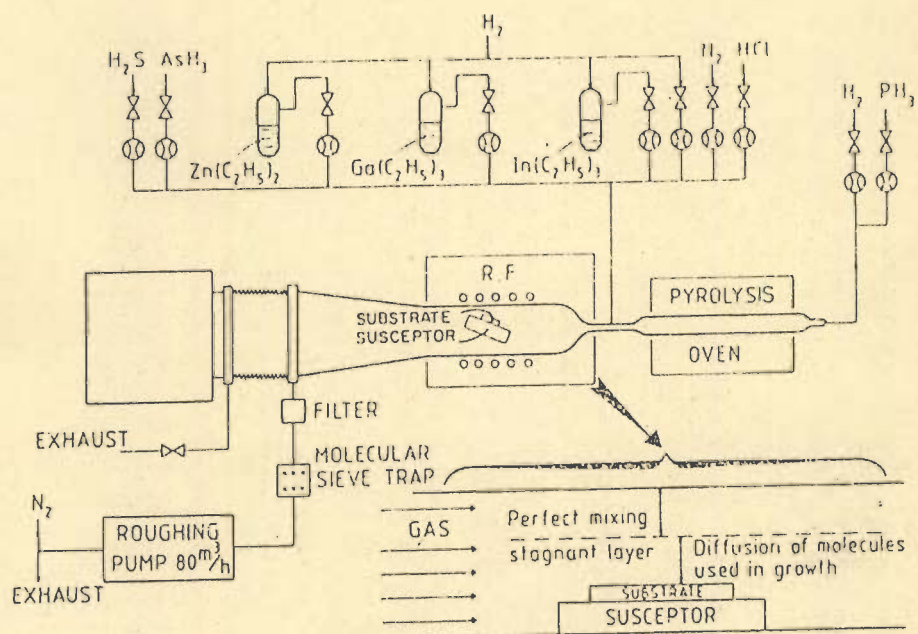


FIG. 2.2 MOCVD

controlled by the flow rates of the various species injected into the reactor, which can be metered accurately by mass flow controllers. Under normal operating conditions the growth rate is generally temperature-independent and the growth process is therefore in the diffusion limited regime. Problem of autodoping has to be considered.

Growth at low pressure increases the diffusion of dopant away from the growth surface by increasing the concentration gradient across the stagnant layer. This results in a more abrupt change in doping level which can be critical in devices which utilize very thin layers. Also as a result of the low pressure in the reactor, the gas speeds are generally higher than for other growth techniques. Thus changes of composition at heterojunctions can be quickly achieved as new gas compositions are rapidly established. The higher gas velocity also results in a more uniform stagnant layer thickness over a large area of substrate, which will ensure a good uniformity of thickness and composition [103, 107].

A number of workers have successfully used low-pressure MOCVD process to grow a wide range of III - V materials and heterostructures like GaAs, InAs, GaInAs on InP, GaInP on GaAs, and GaInAsP on InP [1,8,47,103].

2.5 CONCLUSION

All kind of superlattices described in the previous section have been successfully grown using MBE and MOCVD by many workers. Some of the general problems associated in MBE growth, back ground-gas incorporation, surface accumulation, competitive incorporation, preferential and non-congruent sublimation, interface exchange, and strain-induced interdiffusion are required to be identified. Most of the III - V SLS systems can be successfully grown.

The low-pressure metalorganic chemical vapour deposition based on the prolysis of group III elements in an atmosphere of the hydrides of group V elements would seem to be a widely applicable growth technique which is well adopted to the growth of submicrometer layers and heterostructures. Optimized growth conditions for the preparation of wide range of III - V materials and heterostructures on GaAs and InP substrates were found [1,103] because of low pressure. The low pressure growth offers an improved thickness uniformity and compositional homogeneity.

The knowledge of growth processes is necessary for the simulation of rocking curves.

CHAPTER 3
REVIEW OF METHODS OF CHARACTERIZATION
OF SUPERLATTICES

3.1 INTRODUCTION

III - V semiconductor materials possess properties which are influenced by a number of parameters. The crucial factor that permits the progress in research on such materials is in understanding the parameter which control the properties of these materials. These include chemical composition and structural perfection of materials etc. Accordingly, material characterization involves determination of composition, purity, crystallinity and perfection of atomic arrangement in the material. The impurity and defects in atomic arrangement or lattice imperfections, are to be identified which influence the property under consideration. The defect concentration and spatial locations are determined and correlated with the material property. Determination of impurity concentration is a challenging task as very small concentration of impurities at parts per billion (ppb) are to be determined.

For multilayer devices it is more urgent requirement to ascertain that compositional and thickness variations are within specified tolerances. The improvement of growth techniques coupled with the wide variety of structures, that can be obtained using semiconductors with different lattice parameters. High quality InGaAs epilayers are obtained as long as the mismatch between the substrate and the epilayer can be accommodated by elastic deformation without creating misfit dislocations at the interface. However, as the layer

thickness increases, the formation of dislocation becomes energetically favourable, which leads to an increased dislocation density at the interface. Presence of mismatch and other dislocation defects in the multilayer structures and superlattices have been found to decrease optical/quantum efficiency and life time of the devices [21].

There are various methods of measuring and analyzing structural and compositional properties of thin films. In the present chapter some of the common methods of characterization of superlattices have been reviewed.

3.2 PHOTOLUMINESCENCE

Photoluminescence (PL) has been developed as an important and powerful tool for the investigation and characterization of semiconductor materials. In photoluminescence experiments, a number of electron-hole pairs are created in excess of the thermal equilibrium number by an external exciting light. A room temperature PL measurement is made using a 6328 Å He-Ne laser for excitation.

One purpose of PL studies is the determination of the bandgap energy versus composition of $\text{Ga}_x\text{In}_{1-x}\text{As}_y\text{P}_{1-y}$ quaternary layers. As a result of these experiments a detailed knowledge of the dependence of the fundamental band gap energy on composition x and y is expected [120].

Though photoluminescence provided a convenient method to determine the relative position of the bandgap energy the absolute value of E_g is more difficult to obtain [101].

PL studies of free epitaxial layers lattice-matched on InP as well as GaAs have demonstrated that high quality material can be grown using MBE, MOCVD techniques [107]. For InGaAsP/InP heterostructures more complicated PL spectra has been observed than that of free epitaxial layer, this may be due to the impurities, compositional grading, and abruptness of the interfaces.

Photoluminescence of superlattices resulting in a peak due to emission from the wells. This is due to diffusion of the created carriers to the wells before recombination. The observed transition occurs between the first quantum energy levels of electrons and heavy holes. The corresponding energy depends on concentration strain and well width [114]. An accurate study of photoluminescence for MBE grown $\text{In}_x\text{Ga}_{1-x}\text{As}/\text{GaAs}$ have been reported [109]. Figure 3.1 shows PL data. The additional peaks at lower energies may, impart, be due to impurity or defect related bound excitons.

PL spectra for thermally annealed and impurity induced disordered superlattices are studied and reported by many workers [107, 120, 88]. For AlGaAs/GaAs superlattice [62],

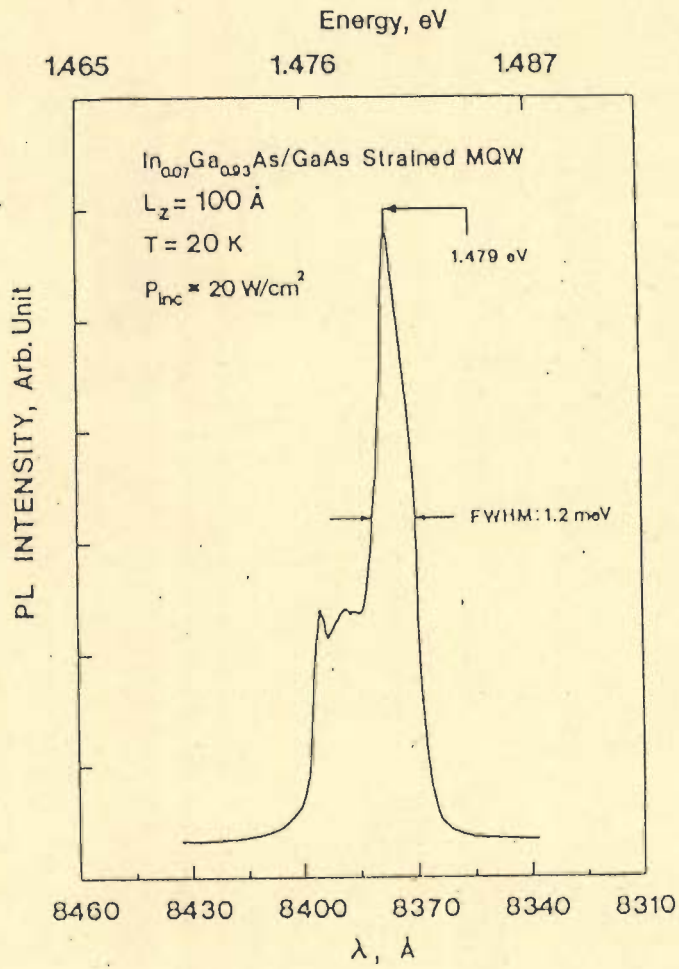


FIG. 3.1 PL SPECTRA OF SLS

InGaAs/GaAs SLS [109, 32], and ionimplanted InGaAs/GaAs SLS [1], GaAsP/GaP SLS [101] PL measurement studies have been reported in the literature.

3.3 TRANSMISSION ELECTRON MICROSCOPY

Imaging methods are superior to optical methods in the sense that since electrons can penetrate into materials more easily than visible light, a three dimensional microstructure of an opaque material may be observed without etching in succession. The depth of penetration depends on the material and the electron energy and specimen thickness of roughly about $0.3 \mu\text{m}$ at 100 KeV and about $1 \mu\text{m}$ at 1 MeV, depending on the material, can be analyzed. Using a high electron energy 100 KeV - 1 MeV makes the wavelength very short and consequently a high resolution is achieved, about 1.5 \AA .

Electron microscopy basically involves scattering processes that take place when the electron beam travels through the specimen. The scattering processes may be divided into two categories: elastic and inelastic. Elastic scattering involves interaction of the electrons and the effective field potential of the nuclei, with no energy losses. Inelastic scattering involves interaction of electrons with electrons in the specimen and results in energy losses. Diffraction patterns produced by elastic scattering

forms the basis for studying imperfections in materials. Inelastic scattering however, also produces informative diffraction effects, but they are more readily used to analyze spectroscopic data resulting from characteristic energy losses and emissions due to absorption effects of the inelastic scattering. These include Auger spectroscopy and X-ray fluorescence. A detail account of the electron optics and electron microscopy are available in many standard texts [125].

The advantage of high resolution in a TEM will have to be weighed against the high cost of the instrument. Economic utilization means that most TEM works is concentrated on specimens known to have high density of dislocations and very rarely on highly perfect crystals. The accessible thickness of the specimen is roughly upto 1 μm and if one utilizes the high resolving power of the TEM to record a micrograph at a high magnification, the information on the micrograph would actually be resulting from a very tiny volume element of the specimen. Specimens are normally in the form of foils, about 1 μm thick. TEM essentially operates in the transmission mode while optical microscopy in the reflected mode. A TEM can very easily produce the micrograph and the electron diffraction pattern for the same area of the specimen.

High resolution transmission electron microscopy has made it possible to study interfaces using lattice imaging. In the case of epitaxial semiconductor multilayer structures which contain similar materials in its layers, it is sometimes difficult to get good contrast sometimes makes it difficult to observe atomic height steps at the interface. Hetherington et al [54] have devised a near axial lattice imaging technique to overcome the lack of contrast between layers of similar materials and have applied this technique to GaAlAs/GaAs multilayers to study interfacial steps and roughness of each interface as well as the determination of the widths of each layer to an accuracy of about 1\AA . In multilayer structures, high resolution TEM is thus extremely useful for seeing sharpness of interface, dislocations generated from interface inclusions etc., and steps in the interface.

Sample preparation for TEM study is time-consuming and the level of care exercised is directly reflected in the quality of the results that can be obtained. The specimen must be thinned down to a few nanometers, with the region of interest surrounded by thicker material which can serve as a mechanical support.

Many experimental studies on the TEM characterization of superlattices are available in the literature [29,75,90]. TEM micrograph of GaAs/AlAs [75], GaAlAs/GaAs [29], and

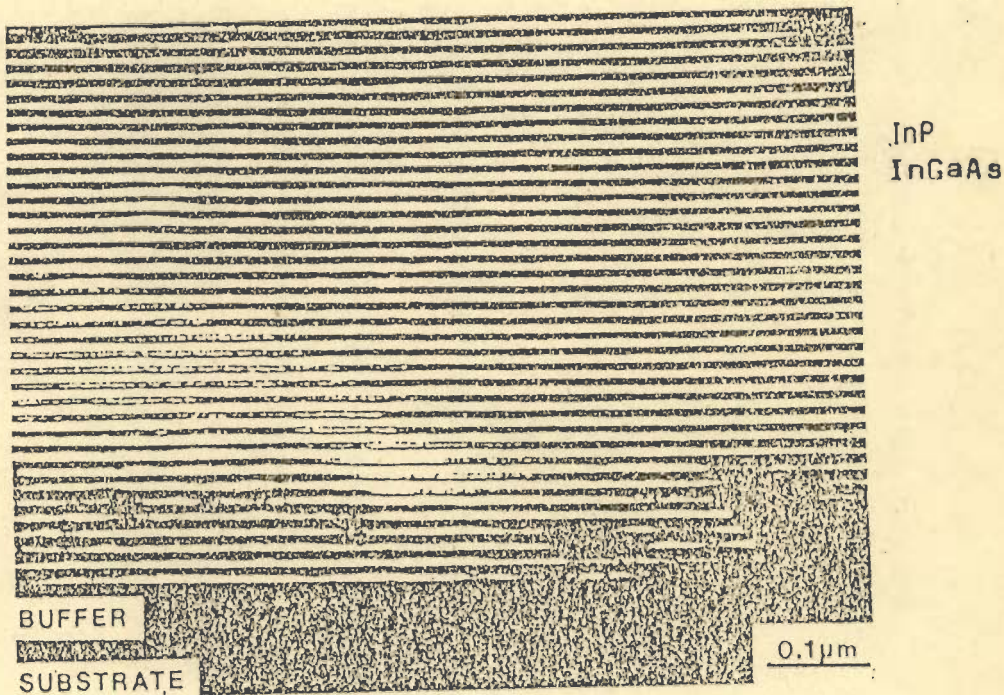


FIG. 3.2 TEM MICROGRAPH OF SLS

InGaAs/GaAs SLS [90] are reported and studied. Figure 3.2 shows a TEM micrograph for a SLS structure, this micrograph shows wells and barriers separately from the substrate. Any structural defect present can be clearly seen.

3.4 AUGER SPECTROSCOPY

Auger spectroscopy can be applied as a microanalytical technique to provide information about the chemical composition of a surface. A sample is mounted in a high vacuum and irradiated with mono-energetic electrons, allowing interaction of the incident electrons with surface atoms, due to which electrons are emitted by the Auger process from the surface. It is therefore necessary to have suitable detectors to analyze the energies of the emitted electrons and be able to separate the weak Auger signal from the general secondary electron signal. Because there are normally a number of Auger transitions with characteristic energies, shapes and patterns, the elemental resolution is good. Since electron beams are normally used, spatial resolution in the plane of surface is also good. Standard instruments are available with minimum electron beam size of 500\AA . Since Auger signal comes entirely from atoms within a few nanometers of the specimen surface, an ultra high vacuum chamber is essential to maintain an atomically clean surface. This also helps to obtain good signal with small probe diameters using high brightness field-emission

gun. The depth resolution, normal to the surface, is better than in the surface plane. The inelastic scattering cross-section for low energy electrons in solids is so large that the electron mean free path is only about a 10\AA . Therefore Auger electron spectroscopy is very sensitive to surface region of the solid. Cylindrical mirror analyzers are the most commonly used electron energy analyzers in AES spectrometers.

For optimum results, specimens to be investigated by AES are some what restricted. If the surface is to be uniformly irradiated by the electron beam, it must be fairly smooth. Also, charging effects should be minimized by a suitable choice of incident beam energy and angle. Magnetic fields in the vicinity of the specimen also produce undesirable effects. Since UHV conditions are advisable, the material should have a relatively low vapour pressure, particularly since electron bombardment causes local heating. Since UHV apparatus and sophisticated electron optics are required, equipment for Auger analysis is expensive [70, 85, 125].

Auger depth profiling, is the most popular technique, for thin film analysis. Here, composition variations in layers adjacent to a surface are revealed by sequential inert ion sputtering and AES. The surface is simply eroded away in a controlled fashion by ion bombardment and the

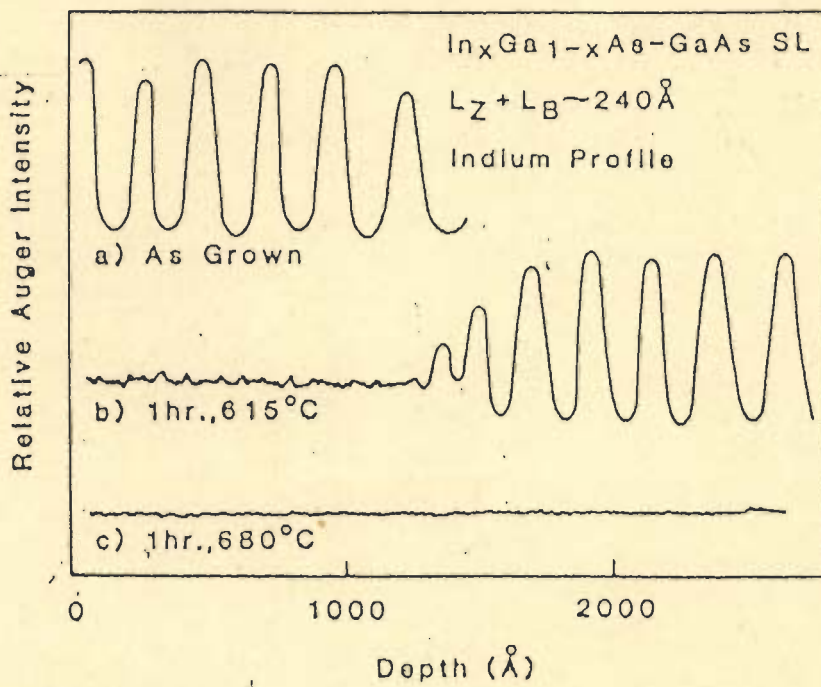


FIG. 3.3 AUGER SPECTRUM OF SLS

composition of the freshly exposed surface determined by AES. Calculation of the depth of material removed is problematic for complex surfaces. Figure 3.3 shows an Auger depth profiles of a InGaAs/GaAs SLS before and after disordering. The indium profile as a function of depth from the crystal surface clearly resolves the SLS structure of the as-grown sample. The indium profile of the SLS diffused for one hour at 615°C shows the intermixing of first few periods of SLS. The remaining layers retain the original SLS structure. The indium profile for the SLS diffused for one hour at 680°C is essentially featureless. This shows that SLS structure is completely disordered [85]. The interface width measured is approximately 12\AA , which is the limit of resolution of the apparatus, then for more accuracy the interface investigation can be made using Raman scattering or X-ray double crystal diffraction.

3.5 RAMAN SCATTERING

The Raman effect arises when a beam of monochromatic exciting radiation passes through a transparent medium that contains molecules capable of undergoing a change in polarizability. Some of the incident phonons collide with molecules in the sample. Most of the collisions are elastic in the sense that the frequency of the scattered light is unchanged from the frequency of the incident

radiation. However, a small fraction of the collisions are inelastic and involve an exchange of energy between the scatter and the incident photon. The fundamental equation for the energy interchange is -

$$h\nu_1 + E_1 = h\nu_2 + E_2 \quad (3.1)$$

or
$$\Delta E = h\nu_1 - h\nu_2 = \pm h\Delta\nu \quad (3.2)$$

where ν_1 and ν_2 are frequencies of incident phonon and the scattered radiation, respectively, and E_1 and E_2 are the initial and final energy states of the scatter. The incident phonon elevates the scattering molecule to a quasi-excited state having a height above the initial state equal to the energy of the exciting radiation [30, 120]. On the return to the ground electronic state, a vibrational quantum of energy may remain with the scatter and hence there is a decrease in the frequency of the re-emitted radiation. If the scattering molecule is in excited state, a vibrational quantum of energy may be taken from the scatter, leaving it in a lower vibrational energy state and thus increasing the frequency of the scattered radiation. These scattered lines are called Raman lines. The shift in frequency of the scattered Raman lines is proportional to the vibrational energy involved in the transition, and thus the shift is a measure of the separation of the two vibrational energy states of the molecule. The spacing between the

Raman lines are related to the vibrational-rotational spacings in the infrared absorption spectrum.

A GaInAs/AlInAs multiple quantum well structure characterized using Raman spectroscopy by Davey et al [30] in the experiment, Raman spectra were measured using the 514.5 nm line of the argon-ion laser and a spec 1403 double spectrometer fitted with an RCA C31034 photomultiplier. All measurements were made with the scattered light collected at 90° to the direction of the propagation of the laser light that was incident at an angle close to Brewster's angle and polarised in the plane of incidence. To eliminate scattering by air the sample space was purged with He gas. The spectrum consists of a series of peaks whose frequencies are directly related to the superlattice period via an appropriate form of the superlattice phonon dispersion relation.

Figure 3.4 shows the Raman spectrum for a GaInAs/AlInAs multiple quantum well structures. Three dominant peaks are observed in the high-energy optical phonon region of the spectrum at 235.0(A), 259.0(B) and 366.8(C) cm^{-1} . Peak B is due to GaInAs layers are In-rich, and A and C are due to scattering by InAs-like and AlAs-like LO phonons in the AlInAs layers. Other various superlattices have been characterized using Raman scattering are reported in the literature [30, 120, 94].

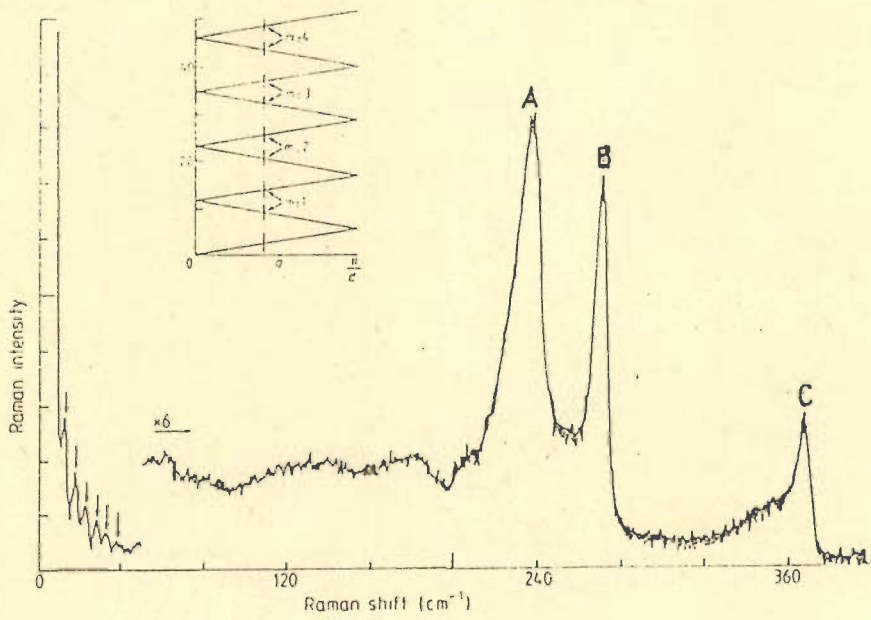


FIG. 3.4 RAMAN SPECTRUM OF SLS

3.6 RUTHERFORD BACK SCATTERING

The only technique for quantitative compositional analysis of thin films which does not require standards is Rutherford back scattering (RBS). This technique uses a beam of monochromatic H^+ or He^+ ions. The beam energy is typically between 0.3 and 3 MeV. The name actually comes from the fact that the analysis of data is the same classical analysis, which was used by Lord Rutherford in the late 1800s to analyze the elastic scattering of charged particles approaching the nuclei of atoms in a thin metal foil. This was the first experiment to indicate that most of the mass of an atom is concentrated in a charged nucleus.

Calculations based on the conservation of both energy and momentum in an elastic collision indicate the ratio of ion energy after collision, E_c to ion energy before collision E_o is [70]

$$\frac{E_c}{E_o} = \left[\frac{(m_2^2 - m_1^2 \sin^2 \theta)^{\frac{1}{2}} + m_1 \cos \theta}{m_1 + m_2} \right] \quad (3.3)$$

where, m_1 = Ion mass; m_2 = Mass of ion in sample and
 θ = Scattering angle.

For the case of collisions at a sample surface into a given angle θ , the energy of the scattered ion uniquely identifies the mass of the surface atom.

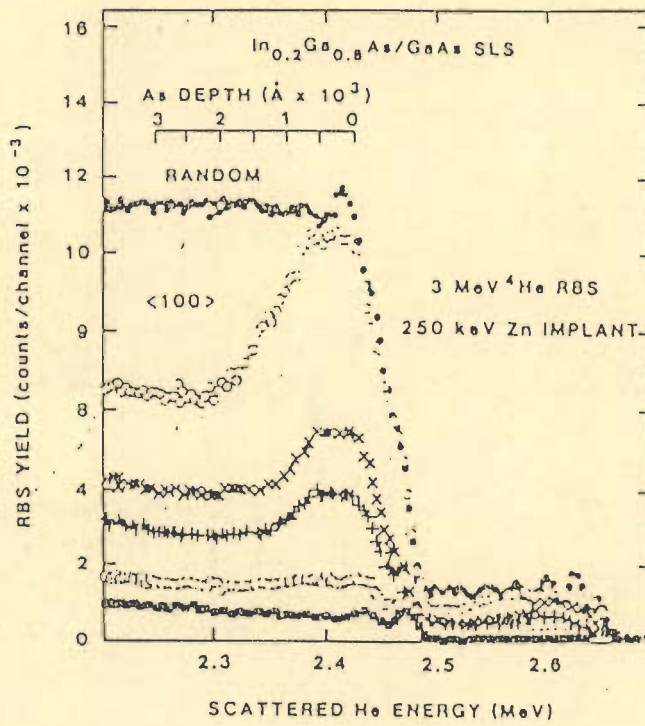


FIG. 3.5 RBS SPECTRA

In the case of a thin film in which the concentration of interest changes with depth, RBS can provide a concentration profile. RBS also used to monitor lattice disorder produced by the various implants. RBS yields for $\langle 100 \rangle$ channeling as a function of Zn fluence are shown in Figure 3.5 for an InGaAs/GaAs SLS samples reported in the literature [1]. The damage produced by the 250 keV Zn implantation introduces a dechanneling disorder which extends from the surface to $\sim 2000 \text{ \AA}$ below the surface consistent with the calculated damage depth. Similarly, a 75 keV Be^+ implanted GaAsP/GaP SLS have also been studied using RBS technique by Myers et al [91].

3.7 X-RAY DOUBLE CRYSTAL DIFFRACTION

This section will concentrate on the use of X-ray diffraction method for structural investigations. X-rays being electromagnetic waves, cause electrons to oscillate at the X-ray frequency. These oscillating electrons in turn emit radiation with the same wavelength as the incident radiation i.e. they serve to scatter the X-rays. The radiation scattered by each electron will be coherent and hence, in the case of rows of atoms, the X-rays will reinforce in certain directions and cancel in others. The directions of reinforcement are given by Bragg's law i.e.

$$\lambda = 2d \sin\theta \quad (3.4)$$

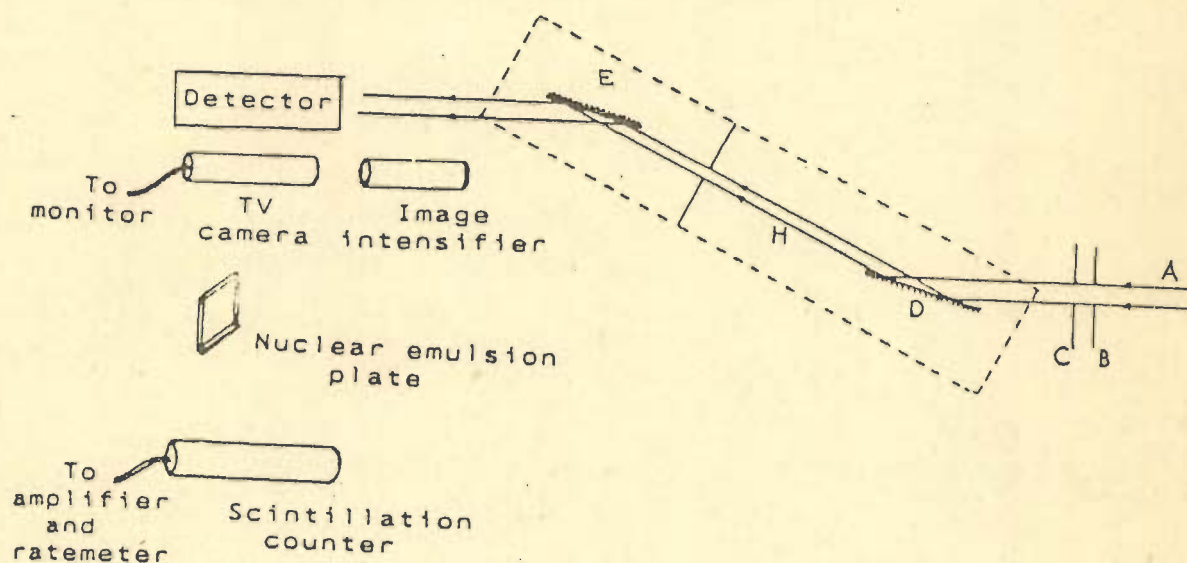


FIG. 3.6 X-RAY DOUBLE CRYSTAL DIFFRACTION

where λ is X-ray wavelength, d is the spacing between the crystal plane, and 2θ is the scattering angle [152].

As shown in Figure 3.6 a white synchrotron beam A passes through a horizontal slit B and a vertical slit C and on to a beam conditioner or a reference InP crystal D mounted on the first axis of the goniometer of the double crystal camera. The slit B and C are only to localize the area on the specimen E. If the reference crystal is a (100) InP, a (400) reflection is the most convenient to consider as the structure factors are otherwise too low for a (200) reflection and zero for a (100) reflection. Furthermore the angular spread of double crystal rocking curves for higher order reflections is larger and therefore it is more convenient to separate the substrate and epilayer peak in a rocking curve. The Bragg angle corresponding to a wavelength λ for a (400) reflections is,

$$\theta_B = \sin^{-1} (2\lambda/5.8688) \quad (3.5)$$

The reference crystal surface is aligned at an angle θ_B with respect to the incoming beam. If however, a silicon monochromator is mounted on the 1st axis, it is aligned for a (111) reflection at a wavelength λ , the Bragg angle for which is

$$\theta_B = \sin^{-1} (\lambda/6.27) \quad (3.6)$$

From the geometry of the goniometer it is possible to

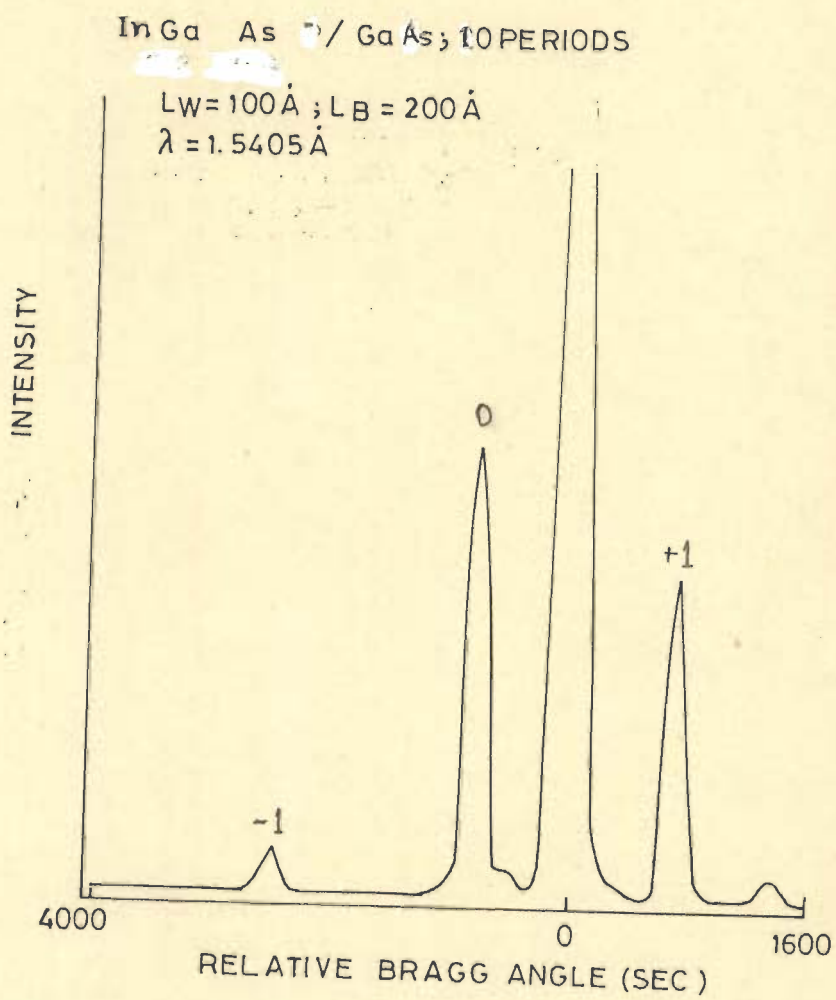


FIG. 3.7 DOUBLE CRYSTAL EXPERIMENTAL ROCKING CURVE

calculate the angle at which it is required to be adjusted to ensure that the diffracted component H heads towards the second axis. Mounted on this axis is the specimen. The parallel setting (+, -) is the most appropriate to consider. The specimen is now roughly adjusted to the required Bragg angle for (400) reflection. It is now necessary to rotate the specimen about the initial setting in order to locate the substrate and epilayer peaks of the specimen. Accurate control over the rotation of the camera axes is achieved by a software routines [125].

Detector and counters are used to detect the substrate and epilayer intensity maximas. A slit 100x500 μm is used to define a point on the specimen E. Figure 3.7 shows an experimental (400) rocking curve for an SLS structure obtained from the literature [114]. From this experimental rocking curve following information is obtained:

- (1) The substrate peak.
- (2) Peak from the average superlattice, named as zero order peak.
- (3) The satellite peaks from the super periodicity of the structure, these peaks are symmetrically located on both the sides of the zero order peak, marked as \pm first order, \pm second order, \pm third order etc.
- (4) The period of the structure is determined by measuring

the angular distance between satellite peaks or the distance between the first order peak and zero order peak.

- (5) The average of the Indium content in $\text{In}_x\text{Ga}_{1-x}\text{As}/\text{GaAs}$ SLS rocking curve is obtained by measuring the distance between the peak from the substrate and the zero order peak.

If the lattice parameter of GaAs and InGaAs are very close, the angular distance between the satellite peaks is very small and double crystal X-ray diffraction is necessary to perform accurate measurements.

$$\bar{x} = \frac{n_2}{n_1 + n_2} x \quad (3.7)$$

where n_1 and n_2 are numbers of molecular layers from GaAs and $\text{In}_x\text{Ga}_{1-x}\text{As}$ respectively, and x is the indium composition, and \bar{x} the average indium composition of the SLS structure.

Also,

$$\bar{x} = \frac{d_2}{d_1 + d_2} x \quad (3.8)$$

where d_1 and d_2 are the thicknesses of the GaAs and InGaAs layers respectively.

In MOCVD process, the growth rate is proportional to the molar fraction of organometallic compounds, so

$$d_1 = v_1 t_1; d_2 = v_1 t_2 \left(1 + \frac{x}{1-x}\right) \quad (3.9)$$

where v_1 and t_1 are the growth rate and growth time of the GaAs layer respectively, and t_2 the growth time of the InGaAs layer;

$$P = d_1 + d_2 = v_1 t_1 + t_2 \left(1 + \frac{x}{1-x}\right) \quad (3.10)$$

where P is the period of the superlattice, and from equations (3.8) and (3.10)

$$x = \frac{\bar{x}(t_1 + t_2)}{t_2 + \bar{x}t_1} \quad (3.11)$$

Thus composition can be compared from the growth parameter and X-ray diffraction studies.

3.8 DISCUSSIONS

PL measurements are frequently used to assess the composition in the epilayer. In the Auger method light elements emit Auger electrons much more efficiently than X-ray emission in the electron microprobe. Auger method needs an ultra high vacuum, which is in fact a disadvantage for routine analysis of materials. TEM on the other hand has an extremely high resolution, but the specimen have to be very thin and thin foils of a sample sometimes behave very differently from the bulk. The lower limit of dislocation density that can be studied in the TEM is about 10^4 mm^{-2} . III - V semiconductor materials for use in lasers employ high

quality epitaxial layers and substrate as far as possible and hence they are supposed to contain very little or no dislocations at all. To understand and control the growth of such materials, one requires techniques which will reveal the degree of perfection over a large area of the specimen.

In the X-ray technique, the higher penetrative power of X-rays resulting from lower scattering factors of atoms for X-ray relative to electrons means that the thickness of the semiconductors specimens that can be studied can be from, say, 10 μm and upwards depending upon various factors. The double crystal X-ray diffraction is a nondestructive method which can assess lattice mismatch and imperfections in thin epitaxial layers and superlattice structures and also provide invaluable information about their thickness and composition. In X-ray double diffraction experimental rocking curves obtained are simple and reproducible.

245-439

Central Library University of Roorki



CHAPTER 4
THEORY OF X-RAY DIFFERACTION

4.1 INTRODUCTION

When a beam of X-rays is incident upon a set of parallel planes in a crystal, the planes behave as a diffraction grating and scatter the X-rays. This scattering of X-rays is due to the individual atoms being provoked by the incident beam. The characteristics of the diffraction phenomena depend on the value of the ratio of the diffracted to incident beam energies. There are basically two theories of X-ray diffraction, namely kinematical and dynamical theory.

In the kinematical theory, the amplitude of X-rays diffracted from diffracting centres are at all times assumed very small in comparison to the incident wave amplitude. This assumption is based on the fact that the interaction of X-rays with matter is always very weak and that the scattering of X-rays by an atom is always very small and is valid for very thin crystals as well as highly deformed crystals [123,27]. The kinematical theory ignores extinction effect, hence a dynamical theory is developed which properly accounts for extinction and dispersion correction along with all the interactions between diffracted and incident beams [9,10,12,13,141]. Since rocking curves of various superlattice structures using both kinematical and dynamical approaches have been simulated and compared in the present thesis, therefore diffraction theories have been studied in detail in this chapter.

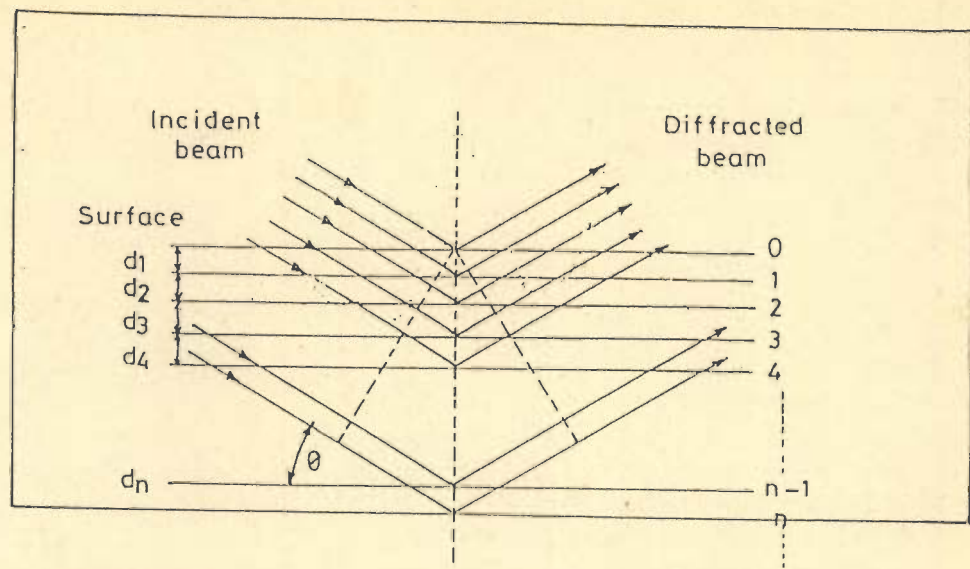


FIG. 4.1 MODEL OF X-RAY DIFFRACTION IN KINEMATICAL TREATMENT

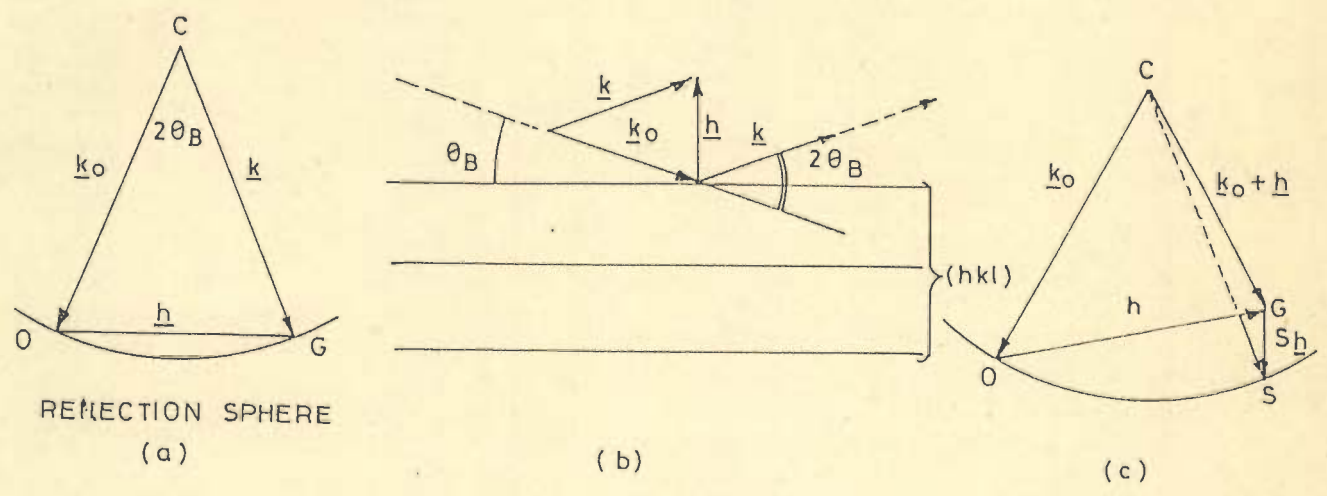


FIG. 4.2

4.2 KINEMATICAL THEORY OF X-RAY DIFFRACTION

The kinematical treatment is the most simplest approach for calculating the amplitudes of the diffracted beams. It involves, however, very daring assumptions. The assumptions are [27];

(1) An electron can only be scattered once.

(2) The depletion of the incident beam when progressing into the crystal can be ignored.

The usual kinematical treatment in the case of X-rays consist in considering the scattering by each individual scattering centre arranged on a lattice, and by summing up the amplitudes of the events, taking their phase relationship into account as shown in Figure 4.1.

4.3 BRAGG LAW AND CONDITION OF DIFFRACTION

The Bragg law can be interpreted with the help of the widely used Ewald sphere as shown in Figure 4.2 (a) the radius of the sphere is $1/\lambda$. If C is its centre and $\vec{CO} = \underline{k}_0$, then O must be the origin of the reciprocal lattice. OG is defined by the reciprocal lattice vector \underline{h} lying on the Ewald sphere, corresponding a diffracted beam with wave $\underline{k} = \vec{CG}$. The angle between \underline{k}_0 and \underline{k} is noted as $2\theta_B$, where θ_B is the Bragg angle.

Figure 4.2 (b) shows the lattice vector \underline{h} is perpendicular to the family of the lattice planes and its length is a multiple of the reciprocal of the interplanar spacing d_{hkl} .

The wave vectors \underline{k}_0 and \underline{k} of the incident and the scattered beam satisfy the well-known Bragg law.

$$\underline{k} - \underline{k}_0 = \underline{h} \quad (4.1)$$

squaring the equation (4.1)

$$k^2 - k_0^2 - 2\underline{k} \cdot \underline{k}_0 = h^2 \quad (4.2)$$

because of first assumption

$$|\underline{k}_0| = |\underline{k}| = 1/\lambda$$

then equation (4.2)

$$\frac{1}{\lambda^2} (2 - 2 \cos 2\theta_B) = \left(\frac{n}{d_{hkl}} \right)^2$$

or finally

$$2d_{hkl} \sin\theta_B = n\lambda \quad (4.3)$$

The condition of diffraction

$$\lambda < 2 (d_{hkl})_{\max} \quad (4.4)$$

This equation (4.4) puts an upper limit to the wavelength, there is also a practical lower limit, since the Bragg

angle must remain larger in order to be observed.

The wave function describing the incident beam with wave vector \underline{k}_0 is

$$\psi_0 = \exp(i\pi 2 \underline{k}_0 \cdot \underline{r}) \quad (4.5)$$

and ψ_h represents one of the diffracted beams the beam \bar{h} inside the crystal.

$$\psi_h(\underline{r}) = \phi_h(\underline{r}) \exp i2\pi(\underline{k}_0 + \underline{h}) \cdot \underline{r} \quad (4.6)$$

$$\text{and } \phi_h(\underline{r}) = \int A(\sigma) (\exp i2\pi\sigma \cdot \underline{r}) d^3\sigma \quad (4.7)$$

where $A(\sigma)$ is the Fourier transform of $\phi_h(r)$.

From the reflection sphere construction of Figure 4.2 (c), it is obtained

$$(\underline{k}_0 + \underline{h} + S_h \underline{l}_z)^2 = k_0^2 \quad (4.8)$$

The deviation parameter S_h is smaller than the dimension of h then

$$S_h = \frac{k_0^2 - (\underline{k}_0 + \underline{h})^2}{2|\underline{k}_0 + \underline{h}| \cos \alpha} \quad (4.9)$$

and the second parameter is extinction distance ξ_h

$$\xi_h = \frac{|\underline{k}_0 + \underline{h}| \cos \alpha}{2me} \frac{1}{|V_h|} \quad (4.10)$$

The change of ϕ_h with z direction is obtained

$$\frac{d\phi_h}{dz} - i2\pi S_h \phi_h \equiv \frac{i\pi}{\xi_h} \exp i\theta_h \quad (4.11)$$

If one substitutes

$$\phi_h = S_h (\exp i2\pi S_h z) \quad (4.12)$$

then,

$$\frac{dS_h}{dz} = \frac{i\pi}{\xi_h} (\exp i\theta_h) (\exp - i2\pi S_h z) \quad (4.13)$$

After taking boundary conditions $S_h(0) = 0$ at $z = 0$.

$$S_h = \frac{i\pi}{\xi_h} (\exp i\theta_h) \int_0^z (\exp -i2\pi S_h z) dz \quad (4.14)$$

then,

$$S_h = (\exp i\theta_h) (\exp - i\pi S_h z) \frac{i \sin \pi S_h z}{S_h \xi_h} \quad (4.15)$$

Or,

$$\phi_h = (\exp i\theta_h) (\exp i\pi S_h z) \frac{i \sin \pi S_h z}{S_h \xi_h} \quad (4.16)$$

For a deformed crystal

$$\frac{dS_h}{dz} = (\exp i\theta_h) \left(\frac{i\pi}{\xi_h} \right) \exp - i(2\pi S_h z + \alpha_h) \quad (4.17)$$

$$S_h = (\exp i\theta_h) \left(\frac{i\pi}{\xi_h} \right) \int_0^z \{ \exp -i[2\pi S_h z + \alpha_h(r)] \} dz \quad (4.18)$$

$$\text{The intensity } I_h = |S_h|^2 \quad (4.19)$$

4.3 RELEVANT FEATURES OF KINEMATICAL THEORY

- (1) If the crystal is very thin there are then not enough scattering centres to build up an important diffracted beam. The scattering events with the different scattering centres are so strongly out of phase that the mutual partial annihilation of the scattered wavelets presents the construction of a strong diffracted beam.
- (2) The kinematical theory, treats the scattering from each volume element in the sample as being independent of that of other volume elements, except for incoherent power losses in reaching and leaving that particular volume element [13].
- (3) The mathematical treatment is simple therefore, needs less computation time for scattering intensity calculation.

4.4 DYNAMICAL THEORY OF X-RAY DIFFRACTION

The dynamical theory, takes into account all wave interactions within the crystalline particle, and must generally be used whenever diffraction from large perfect crystals is being considered. There has been a growing number of studies of diffraction from large perfect crystals

within the last few years, due, in part, to semiconductor materials research.

The dynamical theory predicts a standing wave pattern produced by two coherent travelling plane waves with wave vectors \underline{k}_0 and \underline{k} . When such a pattern exists relative to the atomic planes, the normal photoelectric absorption is radically altered [13].

The analysis of the dynamical theory tends asymptotically towards the kinematical theory in the case of thin perfect crystals. The problem for the dynamical theory is in simple terms, to determine solutions of Maxwell's equations in a periodic medium, employing appropriate boundary conditions which are satisfied by matching to solutions which are plane waves outside the crystals.

4.4.1 THE PERIODIC COMPLEX DIELECTRIC CONSTANT

The electron density, or the density of scattering matter at any point in the crystal can be expressed as a Fourier sum over the reciprocal lattice as

$$\rho(\underline{r}) = \frac{1}{V} \sum_{\underline{h}} F_{\underline{h}} \exp(-2\pi i \underline{h} \cdot \underline{r}) \quad (4.20)$$

where V = volume element of the unit cell.

\underline{h} = reciprocal lattice vector.

= $h\underline{b}_1 + k\underline{b}_2 + l\underline{b}_3$, where h, k, l are the Miller indices of the reflection described by the reciprocal lattice point, and $\underline{b}_1, \underline{b}_2, \underline{b}_3$ are the reciprocal lattice vectors defining the unit cell in the reciprocal space

F_h = structure factor for the hkl reflection.

Assuming that the atoms behave as rigid spheres with respect to their charge densities and neglecting their thermal vibration, the structure factor can be written as,

$$F_h = \sum_n f_n \exp(2 i\pi \underline{h} \cdot \underline{r}_n) \quad (4.21)$$

where the summation is over the n atoms in the unit cell.

f_n = atomic scattering factor of the n th atom.

The refractive index according to the classical dispersion theory is given by a relationship [10].

$$n^2 - 1 = \sum \frac{4\pi \rho'(r) e^2}{m(\omega_a^2 - \omega^2)}$$

where the summation is over the number of resonators or absorption bands, or more conveniently

$$n^2 - 1 = - \frac{4\pi e^2 \rho(r)}{m \omega^2} \quad (4.22)$$

in most cases of interest, where (n^2-1) is proportional to the square of X-ray wavelength.

The polarization \underline{P} is defined by

$$\underline{D} = \underline{E} + 4\pi\underline{P}$$

and the electric displacement $\underline{D} = \epsilon\underline{E}$.

Since the susceptibility χ is defined by

$$\chi\underline{D} = 4\pi\underline{P} = \frac{\epsilon-1}{\epsilon} \underline{D}$$

it follows that

$$\chi = \frac{\epsilon-1}{\epsilon} = \frac{n^2-1}{n^2}$$

Assuming $\epsilon = 1$, this means

$$\chi = \frac{-4\pi e^2}{m\omega^2} \rho(r) \quad (4.23)$$

In a periodic medium, the susceptibility χ is periodic and can be expanded as a Fourier series over the reciprocal lattice as -

$$\chi = \sum_{\underline{h}} \chi_{\underline{h}} \exp(-2\pi i \underline{h} \cdot \underline{r}) \quad (4.24)$$

Equation (4.23) is essentially

$$\chi = \epsilon - 1 = \frac{-e^2 \lambda^2}{\pi m c^2 V} \cdot \sum_{\underline{h}} f_{\underline{h}} \exp(-2\pi i \underline{h} \cdot \underline{r}) \quad (4.25)$$

Comparing equation (4.24) and (4.25)

$$\chi_h = \frac{-e^2 \lambda^2}{\pi m c^2 V} F_h \quad (4.26)$$

The quantity e^2/mc^2 is the classical electron radius

$$r_e = 2.818 \times 10^{-13} \text{ cm}$$

4.4.2 SOLUTIONS OF MAXWELL'S EQUATIONS

Assuming that electrical conductivity is zero at X-ray frequencies and that the magnetic permeability μ is unity, Maxwell's equation, in CGS Gaussian units can be written as-

$$\nabla \times \underline{E} = - \frac{1}{c} \frac{\partial \underline{B}}{\partial t} .$$

$$\nabla \times \underline{H} = \frac{1}{c} \frac{\partial \underline{D}}{\partial t}$$

or using $\underline{D} = \epsilon \underline{E}$ and $\epsilon \approx 1 + \chi$ the above equations reduce to

$$\nabla \times \nabla \times \underline{D} = - \frac{(1+\chi)}{c^2} \frac{\partial^2 \underline{D}}{\partial t^2} \quad (4.27)$$

As χ is very small in the X-ray region, typically of the order of 10^{-5} , equation (4.27) can be written as

$$\nabla \times \nabla \times (1-\chi)\underline{D} = - \frac{1}{c^2} \frac{\partial^2 \underline{D}}{\partial t^2} \quad (4.28)$$

For the solution of the Bragg reflection problem, in the dynamical case, which must yield the same results as the kinematical theory in the limit of thin crystals, we may expect the solutions to Maxwell's equation to consist of sums of plane waves for which the allowed wave vectors are related to one another by the Laue condition.

We accordingly look for solutions for \underline{D} of the form

$$\underline{D} = \sum_{\underline{h}} \underline{D}_{\underline{h}} \exp(-2\pi i \underline{K}_{\underline{h}} \cdot \underline{r}) \exp(i\omega t) \quad (4.29)$$

Substituting equations (4.29) and (4.24) into (4.28), we finally get

$$\sum_{\underline{h}} [\chi_{\underline{h}}(\underline{K}_{\underline{h}} \cdot \underline{D}_{\underline{h}}) \underline{K}_{\underline{h}} - \chi_{\underline{h}}(\underline{K}_{\underline{h}} \cdot \underline{K}) \underline{D}_{\underline{h}}] = [k^2 - \underline{K}_{\underline{h}} \cdot \underline{K}_{\underline{h}}] \underline{D}_{\underline{h}} \quad (4.30)$$

where, $k = \frac{f}{c} = \frac{1}{\lambda}$ is the vacuum wave number.

Equation (4.29) and (4.30) are the fundamental equations of the dynamical theory and are the vector-form equivalent to the electron diffraction case obtained by solving Schrodinger's equation in a periodic medium. For the X-ray case, in general, only one reciprocal lattice point provides a diffracted wave of appreciable amplitude. We thus need to consider only two waves to have appreciable amplitude in the crystal - the incident wave and the diffracted wave from a reciprocal lattice vector \underline{h} . Equation (4.30) then becomes

$$\begin{aligned} \chi_h(\underline{K}_h \cdot \underline{D}_o) \underline{K}_h - \chi_h(\underline{K}_h \cdot \underline{K}_h) \underline{D}_o + \chi_o(\underline{K}_h \cdot \underline{D}_h) \underline{K}_h \\ - \chi_o(\underline{K}_h \cdot \underline{K}_h) \underline{D}_h = (k^2 - \underline{K}_h \cdot \underline{K}_h) \underline{D}_h \end{aligned} \quad (4.31)$$

and

$$\begin{aligned} \chi_h^-(\underline{K}_o \cdot \underline{D}_h) \underline{K}_o - \chi_h^-(\underline{K}_o \cdot \underline{K}_o) \underline{D}_h + \chi_o(\underline{K}_o \cdot \underline{D}_o) \underline{K}_o \\ - \chi_o(\underline{K}_o \cdot \underline{K}_o) \underline{D}_o = (k^2 - \underline{K}_o \cdot \underline{K}_o) \underline{D}_o \end{aligned} \quad (4.32)$$

Making the substitutions

$$\begin{aligned} C = \underline{D}_o \cdot \underline{D}_h &= 1 \text{ for } \sigma \text{ polarization} \\ &= \cos 2\theta_b \text{ for } \pi \text{ polarization} \end{aligned}$$

$$\alpha_o = \frac{1}{2k} [\underline{K}_o \cdot \underline{K}_o - k^2(1 + \chi_o)]$$

$$\alpha_h = \frac{1}{2k} [\underline{K}_h \cdot \underline{K}_h - k^2(1 + \chi_o)]$$

a non-trivial solution of equations (4.31) and (4.32) gives

$$\alpha_o \alpha_h = \frac{1}{4} k^2 C^2 \chi_h \chi_h^- \quad (4.33)$$

Equation (4.33) is an important relation linking \underline{K}_o and \underline{K}_h in the crystal and describes a dispersion surface, drawn in Figure 4.3.

OO and HH are sections of segments of spheres of radius k drawn with centres at O and H respectively of

the reciprocal lattice. In the absence of a Bragg reflection, the situation inside the crystal is that since $D_h = 0$,

$$|K_o| = k(1 + \chi_o/2)$$

The wave vectors now start on spheres $0'0''$ and $H'H''$ which have radii equal to $k(1 + \chi_o/2)$. In effect, the wave vector is corrected for the refractive index.

$$\text{As } \chi_o \text{ is small, } |K_o| = |K_h| = k$$

The Laue condition is satisfied only at, or close to the intersection of the two spheres and a strong diffraction would then occur.

In the absence of a diffracted wave, the tail of the wave vector \underline{K}_o in the crystal will fall on the spheres $0'0''$ about O , far from the Laue point L . When strong diffraction occurs, \underline{K}_o and \underline{K}_h are governed by equation (4.33) and the tail can no longer lie on the spheres. In Figure 4.3, α_o and α_h correspond to the perpendicular distances of a point A to the spheres $0'0''$ and $H'H''$. The distances are small compared to the radii of the spheres, so the section of the spheres can be approximated to a plane while calculating the perpendicular distance. The equation (4.33) for the dispersion surface is a hyperboloid of revolution with axis OH . Figure 4.3 shows a section of the hyperboloid:

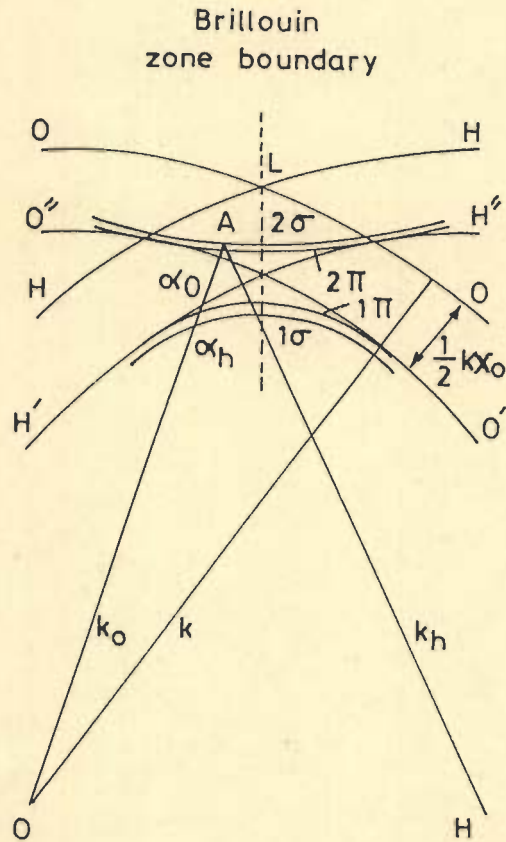


FIG. 4.3 CONSTRUCTION OF DISPERSION SURFACE

a hyperbola asymptotic to $0'0''$ and $H'H''$. There are four branches, two for each polarization state. For small Bragg angles the dispersion surfaces are very close to each other for the two polarization states, but at large Bragg angles, they show significant deviation and the effects of polarization are to be taken into account. \underline{D}_o and \underline{D}_h from equation (4.31) and 4.32) can be substituted in (4.29) to give the propagating wave in the crystal an amplitude

$$\underline{D} = \exp(i\omega t) [\underline{D}_o \exp(-2\pi i \underline{K}_o \cdot \underline{r}) + \underline{D}_h \exp(-2\pi i \underline{K}_h \cdot \underline{r})] \quad (4.34)$$

The amplitude ratio

$$\xi = \underline{D}_h / \underline{D}_o = 2\alpha / Ck\chi_h^- = Ck\chi_h / 2\alpha_h$$

and $\xi^2 = \alpha_o \alpha_h / \alpha_h \chi_h^-$

Thus the dispersion surface not only determines the wave vectors from the position of the point A, but also the ratio of the amplitudes of the waves.

The diameter of the hyperbola of Figure 4.3 is approximately $10^{-5}k$. Figure 4.3 is therefore intentionally magnified around L.

Assuming that there is no absorption, χ_o is therefore real and $\chi_h = \chi_h^*$, or in other words $\chi_h \chi_h^-$ is real. We see that the right hand side of the equation (4.33) is real. Two types of solutions are therefore possible.

If α_o and α_h are both real, then \underline{K}_o and \underline{K}_h are also both real and the appropriate solutions of equation (4.33) are represented by the four branches of the hyperboloid as already discussed and a section of which is shown in Figure 4.3. The factor $C(=1$ for σ polarized state and $=|\cos 2\theta_B|$ for the π polarized state) arises from the dependence of the scattering amplitude on the polarization of the wave. Since α_o and α_h are known at each point on the dispersion surface, ξ is also known and so a solution of the Maxwell's equation is possible to give a complete specification of the waves in the crystal. α_o and α_h are positive for branch 2; hence if χ_h and $\chi_{\bar{h}}$ are real, so that $\chi_h = \chi_{\bar{h}}$, and negative, ξ is negative. The two waves are opposite in phase.

If α_o and α_h are complex conjugates, it directly follows from the definition of α_o and α_h that

$$\underline{K}_o \cdot \underline{K}_o = (\underline{K}_h \cdot \underline{K}_h)^*$$

or $|\underline{K}_o| = |\underline{K}_h^*|$

The real part of \underline{K}_o and \underline{K}_h are thus equal, hence it follows that the tail of the wave vectors \underline{K}_o and \underline{K}_h end on the Brillouin zone boundary. We see that ξ is a complex quantity, the relative phase of the two waves in the crystal thus being determined by α_o .

Assuming χ_h to be real, with $\chi_{\bar{h}} = \chi_h$, we obtain

$$|\xi^2| = 1$$

We can thus summarize the results as follows: If the point A moves from near $0''$ towards H'' , then ξ , starting from a small negative value near $0''$, passes through -1 at the Brillouin zone boundary and approaches a large negative value near H'' . For the pair of dispersion surfaces in branch 1, ξ starts from $+\infty$ near H' , then through $+1$ at the Brillouin zone and approaches $+0$ near $0'$. When there is absorption in the crystal, χ_0 is no longer real and the allowed solutions are complicated. The real parts of the wave vector remain the same but the amplitudes of the waves are changed.

4.4.3 BOUNDARY CONDITIONS FOR SOLUTIONS OF MAXWELL'S EQUATION

Considering that the waves inside the crystal are induced by plane waves incident on the crystal from outside, all necessary boundary conditions must be satisfied.

For a plane polarized incident wave of amplitude

$$\underline{D} = \underline{D}_i \exp(-2\pi i \underline{k}_e \cdot \underline{r})$$

incident on the surface of a crystal, the Bloch waves in the crystal can be considered as a superposition of plane waves such as

$$\underline{D} = \sum_h \underline{D}_h \exp(-2\pi i \underline{K}_h \cdot \underline{r})$$

Continuity of the wave vector across the boundary requires

$$\exp(-2\pi i \underline{k}_e \cdot \underline{r}) = \exp(-2\pi i \underline{K}_h \cdot \underline{r})$$

for each plane wave (corresponding to the incident and diffracted components outside the crystal).

Thus wave vectors inside the crystal differ from that outside only by a vector normal to the crystal surface

$$\underline{K}_{oi} - \underline{k}_e = \underline{K}_{hi} - \underline{k}_e = \delta \hat{n} \quad (4.35)$$

where \hat{n} is a unit vector normal to the surface and $i = 1$ or 2 depending on the branch of the dispersion surface. Equation (4.35) means that a plane incident wave excites two tie points on the dispersion surface that are given by the points of intersection of the unit vector \hat{n} with the dispersion surface. The vector \hat{n} is drawn normal to the crystal surface from the tip of the wave vector \underline{k}_e of the incident wave. In the Laue transmission geometry, these tie points lie on the opposite branches of the dispersion surface whereas in the Bragg reflection case, they lie on the same branch of the dispersion surface. The two tie points represent the tip of the two pairs of wave vectors $(\underline{K}_{o1}, \underline{K}_{h1})$ and $(\underline{K}_{o2}, \underline{K}_{h2})$, certain complex situations are possible in the Laue case where the waves that exit from the lower surface of the crystal that is not parallel to the entrance surface need to satisfy a separate boundary condition involving an additional unit vector \hat{n} normal to the lower surface. The same is true for the Bragg case where the waves can reach the back surface of the crystal

and then return to the front surface and the two surfaces are not parallel.

4.5 PENDELLOSUNG

For a plane wave incident on a crystal there are two Bloch waves within the crystal with two different wave vectors, whose difference leads to a difference in propagation velocity. Fringes are therefore expected to occur in wedge shaped crystals due to interference effects between the Bloch waves.

For a symmetric Laue geometry, it can be shown that the intensity of both the diffracted and transmitted beams exhibits a periodic variation with crystal thickness. The period is given by the depth

$$\xi_d = [\Lambda_o (1 + \eta^2)^{\frac{1}{2}}]^{-1} \quad (4.36)$$

where Λ_o = dispersion surface diameter given by

$$\Lambda_o^2 = \sec^2 \theta_B k_B^2 C^2 \chi_h \chi_{\bar{h}}$$

and η = deviation parameter

$$= 2 \sin \theta_b k \Delta \theta / \Lambda_o$$

η is proportional to the angular deviation from the Bragg condition.

ξ_d has a maximum value at $\eta = 0$, and this is the exact Bragg condition. The extinction depth is then given by

$$\xi_g = \Lambda_o^{-1} = \cos\theta_B / Ck(\chi_h \chi_h^-)^{\frac{1}{2}}$$

$$\xi_g = \frac{\pi V_o \cos\theta_B}{r_e \lambda C(F_h F_h^-)^{\frac{1}{2}}} \quad (4.37)$$

For $\eta \neq 0$, $\xi_g' = \xi_g / (1 + \eta^2)^{\frac{1}{2}}$

As $\eta \rightarrow \infty$, $\xi_g' \rightarrow 0$, only one wave is excited within the crystal and no interference occurs. The transmitted and diffracted intensities are given by

$$I_o = \cos^2[\pi \Lambda_o t (1 + \eta^2)^{\frac{1}{2}}] / (1 + \eta^2)$$

$$I_h = \sin^2[\pi \Lambda_o t (1 + \eta^2)^{\frac{1}{2}}] / (1 + \eta^2) \quad (4.38)$$

In simple terms, a plane wave incident on a crystal excites a diffracted wave in the crystal as it is transmitted through it. Effectively energy is passed from the transmitted to the diffracted beam as the wave passes through the crystal and this phenomenon is called Pendellosung in analogy with coupled pendulum. The diffracted and transmitted intensities are complementary.

Since the intensity of both the diffracted and transmitted beams exhibits a periodic variation with the crystal thickness, if the crystal is wedge-shaped, then in the

thin region the two wavefields cannot separate enough and Pendellosung interference occurs. In the thicker regions, the wavefields diverge and interference is not observed.

The symmetrical Bragg case geometry can also be used similarly to obtain interference effects in thin crystals.

When the crystal is thick, it can be shown that the intensity in the diffracted beam becomes

$$I_h = [|\eta| - (\eta^2 - 1)^{\frac{1}{2}}]^2 \quad (4.39)$$

for a non-absorbing crystal. The intensity is thus dependent of the crystal thickness.

4.6 ROCKING CURVE PROFILE

When a perfect crystal is rotated through the Bragg angle, the intensity of the diffracted beam, as given by equations (4.38) and (4.39) for both the Laue and Bragg cases, which is a function of the deviation parameter η , thus varies. This plot of the diffracted intensity against angular deviation from the Bragg condition is called the rocking curve. It is the convolution of the perfect crystal reflection curve given by equations (4.38) and (4.39) and the divergence of the incident X-ray beam. Assuming that the incident beam is a plane wave, the rocking curve is

given simply by these equations.

Equation (4.38) can be simplified for thick crystals to

$$I_h = (1 + \eta^2)^{-1} \quad (4.40)$$

Equation (4.40) shows that the rocking curve is symmetric. If absorption is included, they tend to become asymmetric. The full width at half maximum intensity is at

$$\Delta\eta = 2$$

This corresponds to an angle

$$\Delta\theta \Big|_{\frac{1}{2}} = \frac{2}{h\xi_g} \quad (4.41)$$

where $1/d$ = magnitude of the reciprocal lattice vector

$$\xi_g = \text{extinction distance}$$

Rocking curve width of perfect crystals are of the order of a few seconds of arc.

Both h and ξ_g increase with the increasing order of reflection, weak reflection means large extinction depths, hence higher order, weak reflections have extremely narrow rocking curve widths.

Equation (4.39) plots the rocking curve for the symmetric Bragg case. As can be seen, for values of $|\eta| < 1$, the term under square root is negative. Physically, no wavefields

can be excited in the crystal and total reflection occurs. The range of total reflection is again $\Delta\eta = 2$ and is given by equation (4.40).

For a double crystal arrangement, in a non-dispersive setting, it can be shown [68] that the rocking curve for the intensity when the second crystal is rotated is the convolution of the reflectivity functions $R_1(\theta)$ and $R_2(\theta)$ of the two crystals

$$I(\theta) = \int_{-\infty}^{\infty} R_1(\alpha) R_2(\alpha - \theta) d\alpha$$

This means that even if the incident beam is not a plane wave, if both the crystals are perfect, the rocking curve is highly symmetrical; but if one of the crystals is distorted, the rocking curve would be asymmetric.

4.7 DISTORTED CRYSTALS

The simple classical theory of Section 4.4 does not explain the diffraction processes in a distorted crystal. Several theories have been proposed and one of the most successful has been that of Takagi [141].

The wave equation for the electric displacement \underline{D} induced by X-rays in a crystal should satisfy

$$\text{div } \underline{D} = 0$$

It is assumed that the wave inside the crystal is of the form

$$\underline{D} = \underline{D}(r) \exp(i\omega t)$$

where

$$D(r) = \sum_h D_h(r) \exp(-2\pi i \underline{K}_h \cdot \underline{r})$$

$D_h(r)$ is now considered to be a slowly varying function of position instead of being constant and $\underline{K}_h = \underline{K}_0 + \underline{h}$

A more convenient expansion is

$$D(r) = \sum_h D'_h(r) \exp(-2\pi i S_h(r))$$

$$\text{with } S_h(r) = \underline{K}_h \cdot \underline{r} - \underline{h} \cdot \underline{u}(r_0)$$

$$\text{where } \underline{r} = \underline{r}_0 + \underline{u}(r_0)$$

$$\text{and } \underline{K}'_h = \text{grad } S_h(r) = \underline{K}_h - \text{grad } (\underline{h} \cdot \underline{u})$$

= wave vector of the h^{th} component wave.

We define a local reciprocal lattice vector in the vicinity of r in distorted crystal by

$$\underline{h}' = \underline{h} - \text{grad } (\underline{h} \cdot \underline{u}(r_0))$$

$$\text{and } \underline{K}' = \underline{K}_{r_0} + \underline{h}'$$

That $D_h(r)$ and $D'_h(r)$ are now variable allows an ambiguity in the definitions of \underline{K}_0 ; the effect of any slight change ΔK_0

in K_o can be compensated by multiplying a factor $\exp(2\pi i \Delta \underline{K}_o \cdot \underline{r})$ to $D_h(r)$ or $D'_h(r)$ without affecting the macroscopic character, as long as $\Delta \underline{K}_o$ is sufficiently smaller than any reciprocal lattice vector.

We initially choose \underline{K}_o such that $|\underline{K}_o| = K = nk$, $n =$ mean refractive index. Substitution of the expression for \underline{D} in Maxwell's equation and neglecting second order effects gives

$$\frac{(\underline{K}_h \cdot \text{grad}) D'_h}{k^2 - k_h^2} + i\pi D'_h + \frac{i\pi K_h^2}{k^2 - k_h^2} \sum_{h' \neq h} \chi_{h-h'} D_{-h} = 0 \quad (4.42)$$

In the case of two strong waves, i.e., the case where only the transmitted and one diffracted wave have appreciable amplitude each of the above equation reduces to a set of two equations with two unknown functions:

$$\frac{\partial D'_o}{\partial S_o} = -i\pi k C \chi_h^- D'_h$$

$$\frac{\partial D'_h}{\partial S_h} = -i\pi k C \chi_h D'_o + 2\pi i k \beta'_h D'_h \quad (4.43)$$

where \hat{S}_o and \hat{S}_h are unit vectors parallel to \underline{K}_o and \underline{K}_h that is, to the incident and diffracted beam directions and

$$\begin{aligned} \beta'_h &= \frac{K_h^2 - K_o^2}{2k^2} = \frac{K_h - K_o}{k} \\ &= \frac{K_h - k(1 + \chi_o/2)}{k} \quad \text{in a non absorbing case.} \end{aligned}$$

When $\beta_h' = 0$ i.e. for a perfect crystal, equation (4.43) reduce to a simple form where they can be solved analytically.

When $\beta_h' \neq 0$, numerical integration must be performed. In any case, equation (4.43) is the basic set of equations to be solved. Taupin [143] has extended the theory of Takagi to obtain the change in the ratio of the diffracted to the incident beam amplitudes as a function of the depth below the surface.

The incident and diffracted beam amplitudes D_o and D_H can be expressed in a differential form [143]

$$i \frac{\lambda}{\pi} v_H \frac{\partial D_H}{\partial Z} = \psi_o D_H + \psi_H D_o - \alpha_H D_H \quad (4.44)$$

$$i \frac{\lambda}{\pi} v_o \frac{\partial D_o}{\partial Z} = \psi_o D_o + \psi_H D_H \quad (4.45)$$

where,

$$v_H = \eta \cdot S_H = -\sin\theta_B$$

$$v_o = \eta \cdot S_o = +\sin\theta_B$$

(assuming a symmetric Bragg case)

with η = unit vector normal to the surface of entrance

S_o = unit vector along the incident beam direction

S_H = unit vector along the reflected beam direction

θ_B = Bragg angle

λ = wavelength of the X-ray beam

D_o = complex amplitude of the incident beam at a depth Z

D_H = complex amplitude of the reflected beam at the depth Z .

$$\psi_H = \frac{-\lambda^2 R_e}{\pi V} F_h \quad (4.46)$$

$$\psi_o = \frac{-\lambda^2 R_e}{\pi V} F_o \quad (4.47)$$

with R_e = classical electron radius = 2.817×10^{-13} cm

V = volume of the unit cell

F_o = complex structure factor in the incident direction

and F_h = complex structure factor for the reflected direction

$$\alpha_H = \lambda^2 \left(\frac{1}{d_H^2} - \frac{2 \sin\theta_B}{\lambda d_H} \right)$$

with d_H = lattice plane spacing assumed a function of depth Z .

A polarization factor $c = 1$ has been used. For any c , ψ_H will be replaced by $c\psi_H$.

The ratio χ , (D_H/D_o), is related to the reflection of the system,

$$\frac{d\chi}{dZ} = \frac{i\pi}{\lambda \sin\theta_B} [c\psi_H \chi^2 + \{2\psi_o - \alpha_H(Z)\}\chi + c\psi_H] \quad (4.48)$$

By varying $\alpha_H(Z)$ symmetrically and on calculating the value of χ at the surface of the specimen, at every instant,

using numerical solutions of equation (4.48), we can compute the graph of the reflectivity for the arrangement.

In a double crystal arrangement, assuming that the first crystal is perfect, we can carry out the product of the convolution of this reflectivity for the specimen with the graph of theoretical reflectivity calculated for the perfect crystal with absorption. The absorption effects are duly taken care of by using complex structure factors in calculations. The resultant convoluted reflectivity is the double crystal rocking curve.

4.8 DISCUSSION

The application of the dynamical theory, for distorted crystals, has been briefly outlined. The amplitude of the wave field has been considered to be a slowly varying function of position. The solution of Maxwell's equation provides an expression for the ratio of the amplitude of the diffracted to the incident wave fields as a function of position within the crystal. This expression would be used to calculate the rocking curves, and the approach adopted to simulate rocking curves of multilayer and superlattice structures is outlined in chapter 5.

CHAPTER 5

COMPUTER SIMULATION OF ROCKING
CURVES AND THEIR COMPARISON WITH
EXPERIMENTAL CURVES

5.1 INTRODUCTION

Double crystal X-ray diffraction is an important tool for the assessment of epitaxial structures [39,55,57,94], and has become one of the most useful means of determining alloy compositions in superlattices [66,124,129,140]. The use of this technique in characterizing multilayer structure is, however, complicated by the complex rocking curves in which there is no longer a one-to-one correlation between diffraction peaks and individual layers in the structure. This problem may be overcome by using kinematical and dynamical X-ray scattering theories to generate simulated rocking curves based on an assumed material structure.

Kinematical diffraction theory have been used to model the rocking curves for superlattices by many workers [66,124,140]. The kinematical theory, however, is not applicable to heteroepitaxial layers or implanted layers whose thicknesses are significantly large in comparison to the extinction distance. In this case dynamical theory must be used.

In this chapter, rocking curves are generated for various superlattice specimens having different compositions, thicknesses, and number of periods. The computer simulations in this study use two different models. (i) A kinematical model has been proposed, following an approach similar

to that used by Speriosu et al [124], and (2) a dynamical model developed on the basis of Takagi-Taupin's derivation [51,143]. Some of the experimental rocking curves of the superlattice structures reported in the literature [15,66,114,85] are analyzed using these models.

5.2 KINEMATICAL SIMULATION

X-ray rocking curves of superlattices are analyzed using kinematical X-ray diffraction by Speriosu et al [124]. Several other authors have investigated the structural properties of AlAs/GaAs [140], AlGaAs/GaAs [55,140], and the InGaAs/GaAs SLS [66,114] using kinematical diffraction model.

In the kinematical theory the amplitude of X-rays diffracted from the diffracting centres are at all times assumed very small in comparison to the incident wave amplitude. This assumption is based on the fact that the interaction of X-rays with matter is always weak and that the scattering of X-rays by an atom is always very small and is valid for very thin crystals. Figure 4.1 shows model of X-ray diffraction in the kinematical treatment.

It is convenient to define X-ray strains of an epitaxial film with respect to the substrate, since these are determined directly from the rocking curve. A difference in the inter-

planar spacing of substrate and layer is

$$\Delta d = d_l - d_s \quad (5.1)$$

the difference Δd depends on the particular deformation as well as on the (hkl) planes. For the layers grown along the direction $\langle 100 \rangle$, $\langle 110 \rangle$, or $\langle 111 \rangle$ the principal strains are perpendicular and parallel to the layer. These strains are related to the difference in d spacing as

$$\frac{\Delta d}{d_s} = \epsilon^\perp \cos^2 \theta + \epsilon^{\parallel} \sin^2 \theta \quad (5.2)$$

where θ is the angle between the planes and surface. For perfectly coherent epitaxy $\epsilon^{\parallel} \equiv 0$ [124].

For diffraction calculation, a uniform epitaxial layer is described by its thickness t , structure factor F , perpendicular and parallel strains ϵ^\perp and ϵ^{\parallel} , and normal absorption coefficient μ .

For the kinematical simulation, atomically abrupt interfaces and uniform layer widths are assumed. With these assumptions the only free parameters remaining in the fitting procedure are the thicknesses of the individual layers d_A , and d_B , where A refers to an InGaAs layer and B to GaAs layer of the superlattice structure.

The kinematical model presented is based on the approach similar to that used by Speriosu et al [123,124,126]. The

closed form expression for the diffracted electric field amplitude E has been used as

$$E = \frac{\sin[M(a_A N_A + a_B N_B)]}{\sin(a_A N_A + a_B N_B)} \cdot F_S \quad (5.3)$$

where M is the number of period in the superlattice, and F_S is the superlattice structure factor given by

$$F_S = F_A \frac{\sin[a_A(N_A + 1)]}{\sin(a_A)} \cdot \exp[i(a_A N_A + a_B N_B)] + F_B \frac{\sin[a_B(N_B + 1)]}{\sin(a_B)} \quad (5.4)$$

where F_A and F_B are the structure factors for the (hkl) reflection of InGaAs and GaAs respectively obtained from standard tables [61]. N_A and N_B are defined to be the number of tetragonal unit cell spacings in each layer of superlattice period.

$$a_{A,B} = 2\pi(\theta - \theta_b^j) \cot \theta_b^s \quad (5.5)$$

where θ_b^s is the Bragg angle of the substrate, and θ_b^j are the Bragg angle corresponding to the layers A and B.

In the present calculation structure factor calculated with dispersion correction. Finally the intensity is obtained by squaring the value E . A computer program has been developed to simulate rocking curves for $\text{In}_x\text{Ga}_{1-x}\text{As}/\text{GaAs}$ SLS structure.

The rocking curves are generated and studied:

- (1) For indium composition $x = 0.1, 0.2, 0.3$ and 0.4 keeping number of periods and epilayers thicknesses fixed. Figures 5.1 to 5.4 show that generated rocking curves have the satellite peaks of different amplitude, and located at different positions.
- (2) For indium composition $x = 0.168$ and epilayers thicknesses 100\AA (well) and 200\AA (barrier), the number of periods are changed from 10 to 20 and 30. Figure 5.5 shows rocking curve for 10 periods and same has been obtained for 20 and 30 periods also.
- (3) For indium composition $x = 0.1$, the number of periods 10, and the epilayers thicknesses changed from 100\AA (well) to 400\AA and 200\AA (barrier) to 800\AA . Figure 5.6 shows that composition modulation is not attained in the SLS.

Experimental rocking curves reported in the literature for InGaAs/GaAs SLS have been simulated as shown in Figures 5.7 and 5.8. From the close fit data the composition, the epilayer thickness, and number of periods have been obtained.

5.3 DYNAMICAL SIMULATION MODEL

Dynamical simulation of rocking curves of the superlattice structure based on the Takagi-Taupin's deriva-

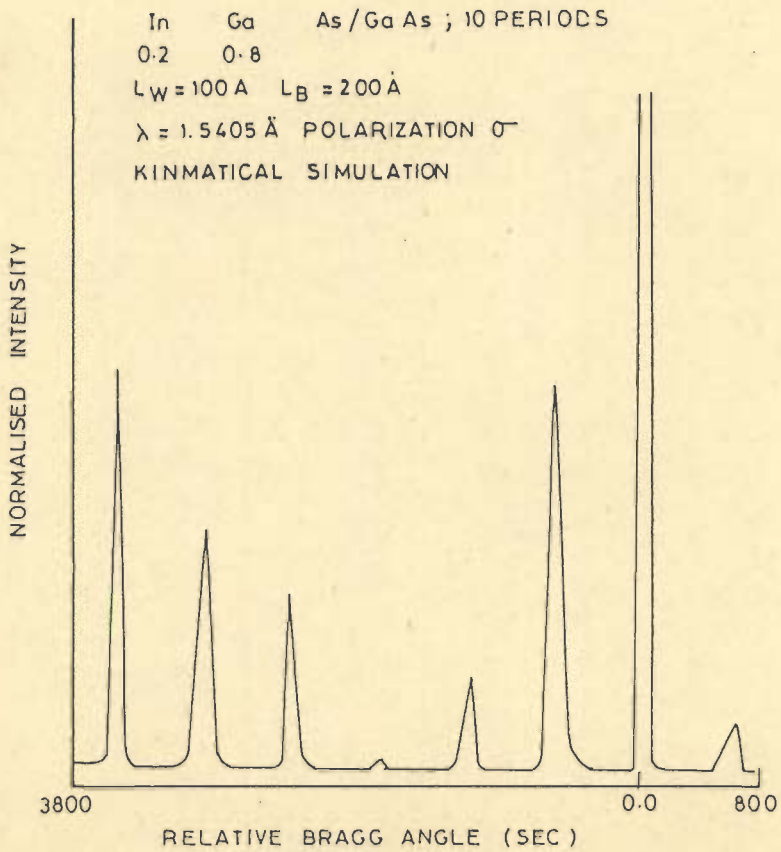
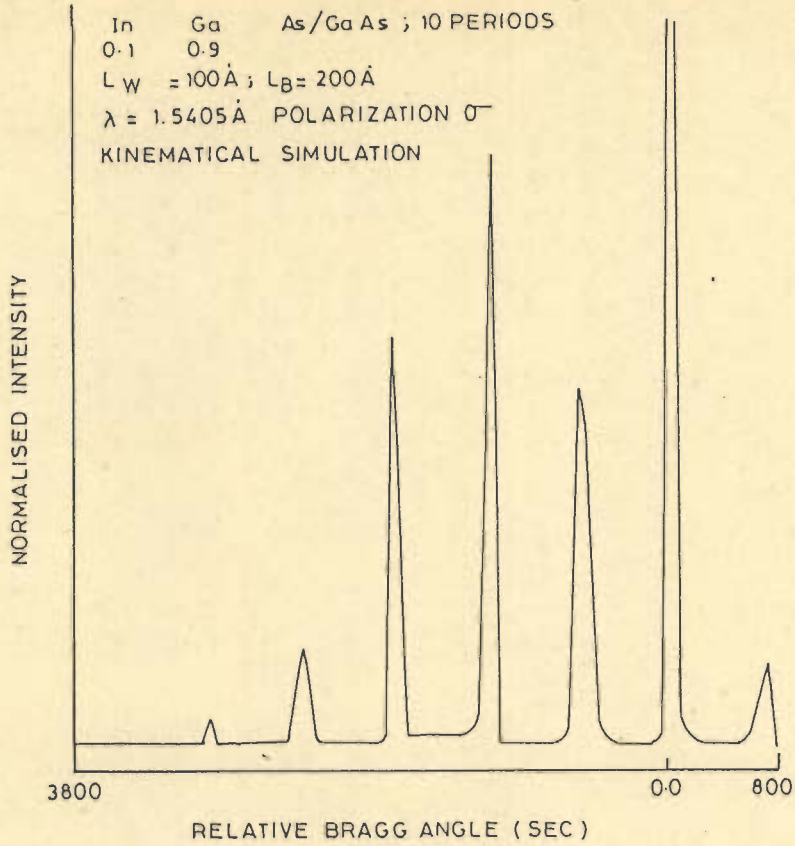


FIG. 5.1 & 5.2

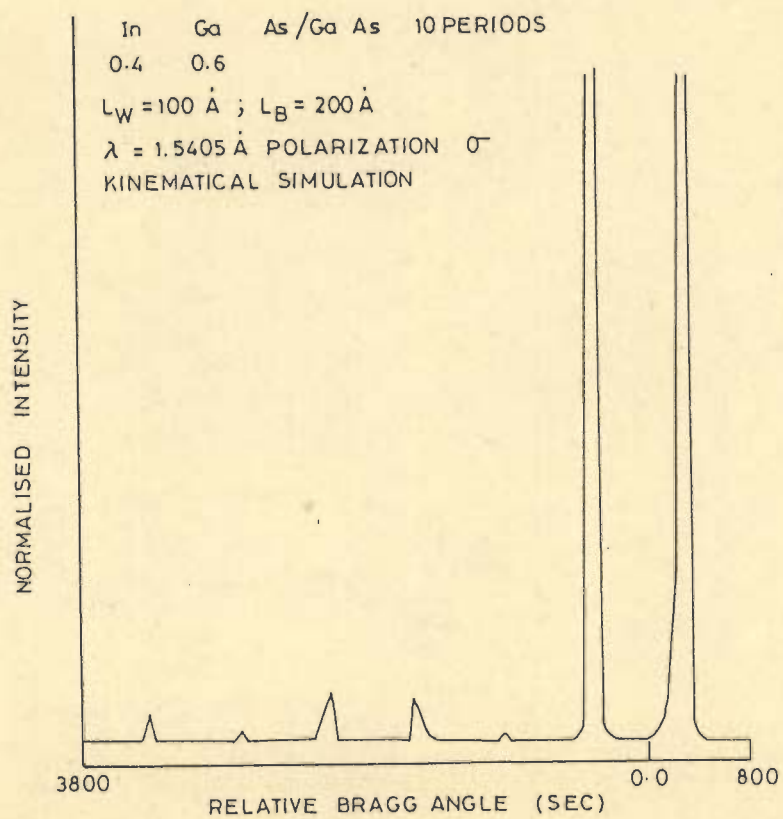
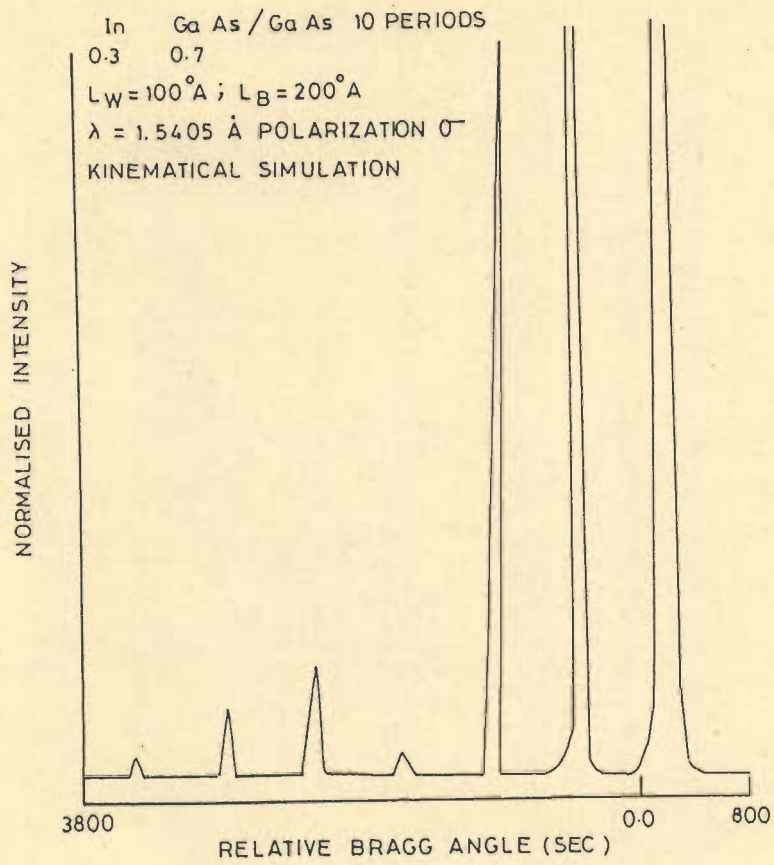


FIG. 5.3 & 5.4

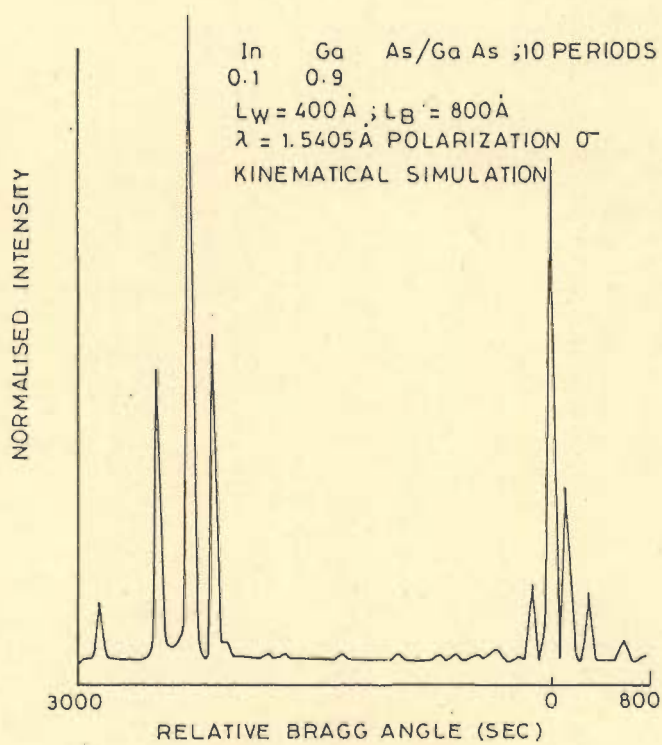
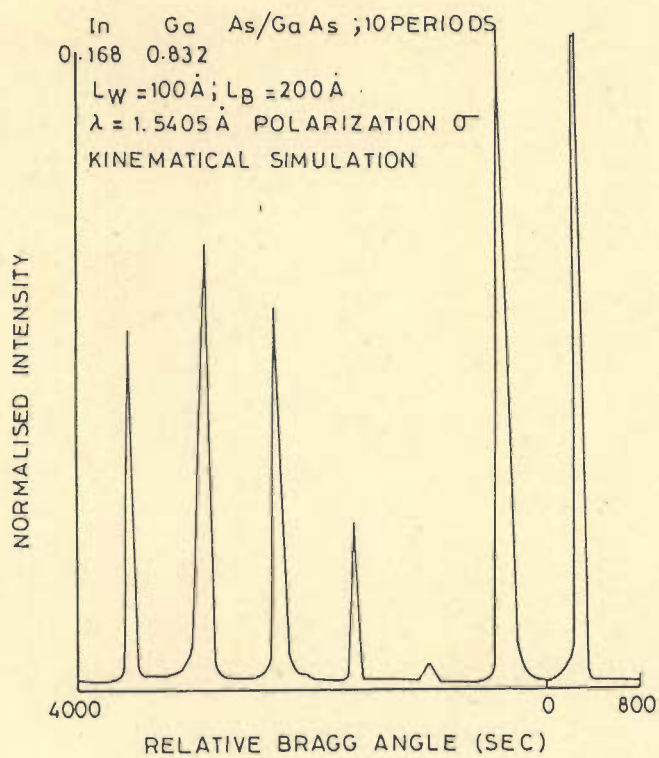


FIG. 5.5 & 5.6

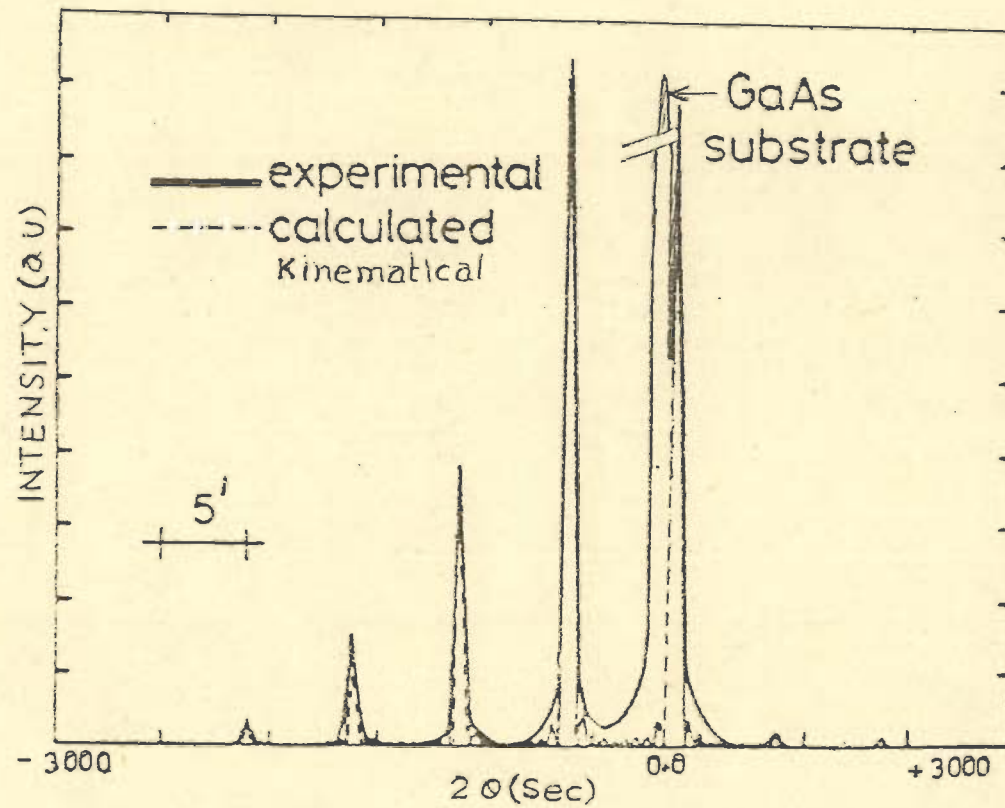


FIG. 5.7 COMPARISON OF EXPERIMENTAL & CALCULATED ROCKING CURVES

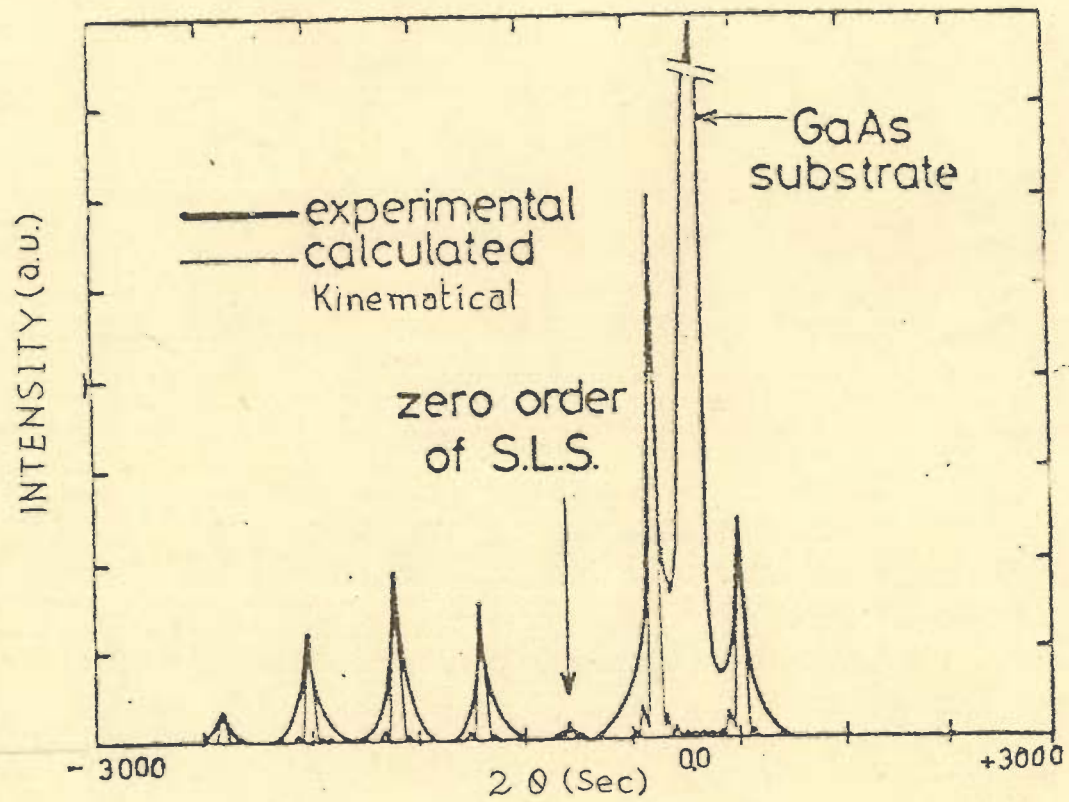


FIG. 5.8 COMPARISON OF EXPERIMENTAL & CALCULATED
ROCKING CURVES

tion [141,143] is presented in this section. In epitaxial layers the diffraction of X-rays can be modelled fairly accurately by solving Taupin's derivation which gives the ratio X of the diffracted to incident beam amplitudes as a function of depth Z below the surface in accordance with equation (4.48), i.e.,

$$\frac{dX}{dZ} = \frac{i\pi}{\lambda \sin\theta_b} [C\psi_H X^2 + \{2\psi_o - \alpha_H(Z)\}X + C\psi_H^2] \quad (5.6)$$

Equation (5.6) can be written in the form

$$\frac{dX}{dZ} = iA(B(X^2 + 1) + 2CX) \quad (5.7)$$

where $A = \pi/\lambda \sin\theta_b$

$$B = C\psi_H$$

and $C = \psi_o - \alpha_H(Z)/2$

$$\begin{aligned} \text{where } \alpha_H(Z) &= \lambda^2 \left(\frac{1}{d_H^2} - \frac{2\sin\theta_b}{\lambda d_H} \right) \\ &= -\frac{2\lambda}{d_H} \cos\theta_b \cdot (\theta - \theta_b) \end{aligned}$$

θ being the angle of incidence of the beam with the Bragg plane. ψ_o and ψ_H are related to the structure factor F by

$$\psi_o = -\frac{\lambda^2}{\pi V} \cdot R_e \cdot F_o$$

and $\psi_H = -\frac{2}{V} \cdot R_e \cdot F_H$

A solution of eqn. (5.7) based on Halliwell's approach [56,55] is followed.

A symmetrical 400 reflection rocking curve was the most appropriate to observe, as peaks corresponding to small lattice parameter mismatch could be conveniently separated and ideally displayed on the angular scale. Furthermore the structure factors for a 200 reflection are too low while for a 100 reflection they are zero. Rocking curves were therefore simulated for a 400 reflection and for superlattices of InGaAs/GaAs or InGaAs/InP grown over (100) InP or GaAs substrates.

Equation (5.7) has a solution of the form

$$X = \frac{iB \tan[AK(Z-Z_0)]}{k-iC \tan[AK(Z-Z_0)]} \quad (5.8)$$

for a thick uniform crystal such as a substrate, where the boundary condition is assumed as $X = 0$ at a point deep inside the crystal, and $K = \sqrt{C^2 - B^2}$. At the surface of the crystal

$$X(0) = \frac{-C + K \operatorname{sgn}[\operatorname{Im}(K)]}{B} \quad (5.9)$$

In order to obtain the reflectivity $R_1(\theta)$ of a single uniform thick crystal, $X(0)$ from equation (5.9) is evaluated at different values of C , which in turn, is a function of the angle of incidence, θ , of the beam. For a thick uniform crystal with several epitaxial layers over it as in a superlattice structure Figure 5.9, if we assume a boundary

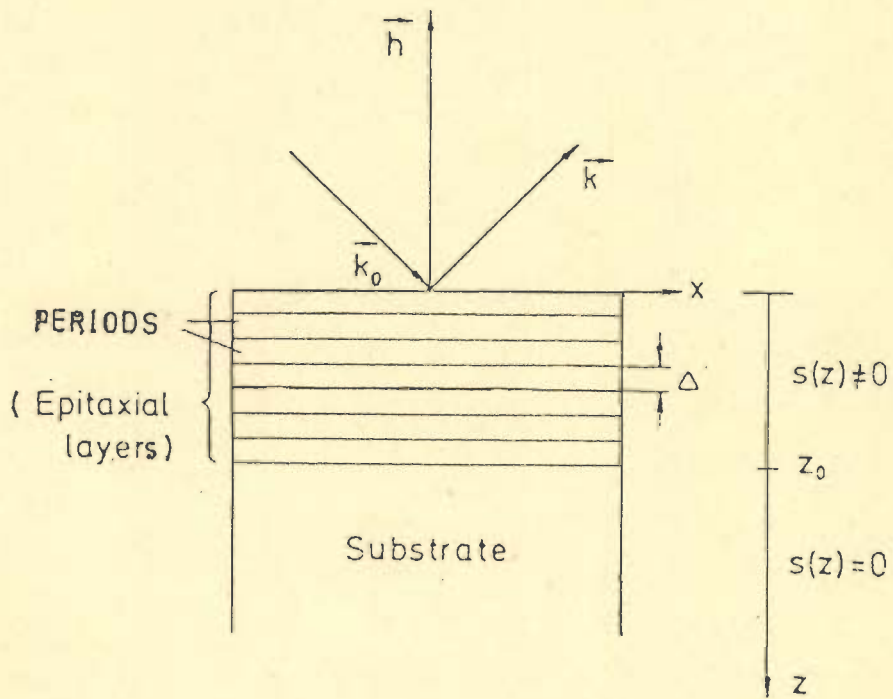


FIG. 5.9 DYNAMICAL MODEL FOR SUPERLATTICE STRUCTURE

condition that $X = X_0$ at $Z = Z_0$. then the solution for equation (5.7) is obtained as

$$X(Z) = \frac{X_0 K + i(B + X_0 C) \tan[KA(Z - Z_0)]}{K - i(C + BX_0) \tan[KA(Z - Z_0)]} \quad (5.10)$$

Equation (5.9) is first evaluated for X at the surface of the substrate. This is then matched as a boundary condition with the value of X at the bottom of the first epilayer of the superlattice period and using equation (5.10), X at the top of the layer is evaluated. The process is repeated until the amplitude ratio at the top of the superlattice is obtained. The constants B and C involve the structure factors and are considered as complex quantities to take into account the absorption effects. Accordingly the amplitude ratio X is obtained as a complex quantity. The reflectivity ratio R_2 is given by

$$R_2 = |X|^2$$

The reflectivity $R_2(\theta)$ at various angles of incidence can be obtained by following the above procedure for various appropriate values of C , C being a function of the angle of incidence, θ . To get the double crystal rocking curve $R(\theta)$ the reflectivity $R_1(\theta)$ of the first crystal (InP) is convoluted with the reflectivity $R_2(\theta)$ of the specimen [68]..

5.3.1 DETERMINATION OF STRUCTURE FACTORS

An accurate representation of the structure factors for the elements involved in a layer is essential in order to reflect the accuracy of the calculated curves, as is evident from the definitions of the constants A, B and C.

InP has a zinc blends structure with a face centred cubic lattice, with four equivalent points at $0, 0, 0$; $\frac{1}{2}, \frac{1}{2}, 0$; $\frac{1}{2}, 0, \frac{1}{2}$; and $0, \frac{1}{2}, \frac{1}{2}$. The structure factor of a material of the type $\text{In}_x\text{Ga}_{1-x}\text{As}_y\text{P}_{1-y}$, can be represented in a convenient form [125]

$$F_{400} = 4.0 [f_{\text{In}}(x) + f_{\text{Ga}}(1-x) + f_{\text{As}}y + f_{\text{P}}(1-y)] \quad (5.11)$$

where f refers to the structure factors for the element concerned. Values of f_{In} , f_{Ga} , f_{As} and f_{P} can be obtained from standard tables [61] for both the 000 and 400 reflections, and thus F_{O} and F_{H} are calculated. We, however, see from equation (5.11) that a complete knowledge of the composition x and y of the layer is required in order to calculate the structure factor for the compound. Also, f , as obtained from tables, are those calculated on the assumption that the frequency of the incident radiation is large compared with any absorption frequencies of the atom. In practice, the scattering factors will have to be duly corrected for any dispersion effects.

5.3.2 COMPOSITION OF x AND y :

In simulating a rocking curve, one of the characteristics of the layers that has to be specified, is the mismatch M defined as

$$M = \frac{a - a_0}{a_0}$$

where a = lattice parameter of the layer, and

$$\begin{aligned} a_0 &= \text{lattice parameter of the substrate} \\ &= 5.86875\text{\AA} \text{ for InP} \end{aligned}$$

The mismatch value for each layer along with its variation within the layer is thus required. In the superlattice period each layer is assumed to have uniform mismatch.

On the other hand, to determine the structure factor for a constituent layer, we require the alloy composition x and y . The alloy compositions are found to bear a definite empirical relationship with material parameters of the layer, namely the lattice parameter and the energy band gap.

For alloys of the form $\text{In}_x\text{Ga}_{1-x}\text{As}_y\text{P}_{1-y}$ the lattice parameter $a(x,y)$ can be expressed [97] as

$$\begin{aligned} a(x,y) &= xy a(\text{InAs}) + x(1-y) a(\text{InP}) + y(1-x) a(\text{GaAs}) \\ &\quad + (1-x)(1-y) a(\text{GaP}) \end{aligned} \tag{5.12}$$

by assuming a linear variation between the binary constituents [100] (Vegards law).

Equation (5.12) accordingly becomes

$$x(x,y) = 5.4512 + 0.41755x + 0.20225y - 0.0125xy \quad (5.13)$$

The band gap variation is taken from the data of Olsen et al [104]:

$$E_g(x,y) = 2.75 - 1.33y - 1.4x + 0.33xy \\ - (0.758 - 0.28y) x (1-x) - (0.21 - 0.109x) y (1-y) \text{ eV} \quad (5.14)$$

To determine x and y , both a and E_g must be known so that equations (5.13) and (5.14) can be solved. For ternary layers like $\text{Ga}_x\text{In}_{1-x}\text{As}$, $y = 1$ and the mismatch M , by itself, is sufficient to specify the lattice parameter, a , and hence, x .

5.3.3 DISPERSION CORRECTIONS

The scattering power of a bound electron of an atom may in an actual case, be more or less than that of a free electron. Furthermore, the phase of the scattered X-rays may be different.

The corrections for the scattering factor thus take the form

$$f = f_a + \Delta f' + i\Delta f'' \quad (5.15)$$

where $\Delta f'$ and $\Delta f''$ are the real and imaginary terms accounting for the dispersion correction.

Cromer and Libermann [20] have calculated $\Delta f'$ and $\Delta f''$ using relativistic scattering theory. The correction factors are available for standard X-ray wavelengths. Making use of these data [61] the correction factors for any wavelength λ can be computed using a polynomial approximation:

$$\begin{aligned} \Delta f' = & a_{11} + (\lambda - 2.291)a_{12} + (\lambda - 2.291)(\lambda - 1.935)a_{13} \\ & + (\lambda - 2.291)(\lambda - 1.935)(\lambda - 1.154056)a_{14} \\ & + \dots \end{aligned} \quad (5.16)$$

$$\begin{aligned} \Delta f'' = & a_{21} + (\lambda - 2.291)a_{22} + (\lambda - 2.291)(\lambda - 1.935)a_{23} \\ & + (\lambda - 2.291)(\lambda - 1.935)(\lambda - 1.54056)a_{24} \\ & + \dots \end{aligned} \quad (5.17)$$

the right-hand side containing as many terms as are correction data available for discrete wavelengths, like Cr $K\alpha$, Fe $K\alpha$, Cu $K\alpha$ etc. the more the number of terms, the wider being the range of application of λ for calculating $\Delta f'$ and $\Delta f''$.

The constants a_{ij} are evaluated from the data for known wavelengths.

Following the procedure outlined in the above section, the correction terms for the atomic scattering factors for In, Ga, As and P can be written in the form

$$\Delta(\text{In}) = F1 + iF2$$

$$\Delta(\text{P}) = F3 + iF4$$

$$\Delta(\text{Ga}) = F5 + iF6$$

$$\Delta(\text{As}) = F7 + iF8$$

The structure factors f_H and f_o for a 400 reflection and 000 reflection at any wavelength λ , can thus be determined for the elements In, Ga, As or P by substituting the values of f_a from standard tables. Equation (5.11) can now be used to determine F_H and F_o :

$$F_H = 4.0[(f_H)_{\text{In}}x + (f_H)_{\text{Ga}}(1-x) + (f_H)_{\text{As}}y + (f_H)_{\text{P}}(1-y)] \quad (5.18)$$

$$F_o = 4.0[(f_o)_{\text{In}}x + (f_o)_{\text{Ga}}(1-x) + (f_o)_{\text{As}}y + (f_o)_{\text{P}}(1-y)] \quad (5.19)$$

F_H and F_o can now be directly employed in equation (5.10) to evaluate X and hence $R_2(\theta)$.

Ideally, the structure factors should be corrected for thermal vibrations by multiplying by a Debye-Waller factor, e^{-M} [17].

5.3.4 EFFECT OF TETRAGONAL DISTORTION

The mismatch parameter of the epitaxial layer used in the calculation of structure factors corresponds to the relaxed lattice parameter a of the layer and is given by

$$M = \frac{a - a_0}{a_0}$$

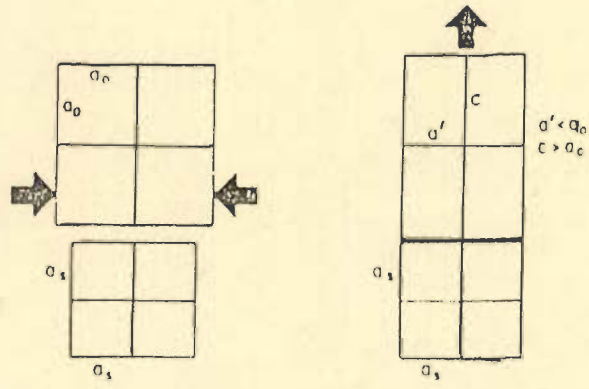
a_0 being the lattice parameter of the substrate. It is assumed that the epitaxial material has a cubic unit cell of dimension a . In actual practice when a thin epitaxial layer is grown over a substrate, lattice accommodation by a tetragonal distortion occurs as shown in Figure 5.10, as a result of which the unit cell for the layer adopts a dimension $a_l \times a_l \times c_l$, where c_l is the unit cell dimension perpendicular to the interface and a_l , the dimension parallel to the interface. For coherent layers $a_l = a_0$. The mismatch m measured experimentally corresponds to the lattice parameter c_l of the layer.

$$\text{Hence } m = \frac{c_l - a_0}{a_0}$$

Using the theory of elasticity, the stress-strain relations for the present case can be written as

$$\epsilon_1 = S_{11}\sigma_1 + S_{12}\sigma_2 \quad (5.20)$$

$$\epsilon_2 = S_{12}\sigma_1 + S_{11}\sigma_2 \quad (5.12)$$



$$\epsilon_{e1} = \frac{a_0 - c}{a_0}$$

$$a' = a_0 (1 + \epsilon_{e1})$$

$$c = a_0 (1 - \epsilon_{e1})$$

FIG. 5.10 TETRAGONAL DISTORTION

$$\epsilon_3 = S_{12}\sigma_1 + S_{12}\sigma_2 \quad (5.22)$$

where $\epsilon_1 = \epsilon_2 = \frac{a - a_1}{a}$

is the strain in the x and y directions parallel to the plane of the interface.

$\epsilon_3 = \frac{a - c}{a}$ is the strain in the z direction

perpendicular to the interface, $\sigma_1 = \sigma_2$ is the stress in the x or y directions and s_{ij} are the stiffness coefficients.

Equations (5.20) to (5.21) for the present case become

$$\epsilon_1 = \epsilon_2 = (S_{11} + S_{12})\sigma_1 \quad (5.23)$$

$$\epsilon_3 = 2S_{12}\sigma_1 \quad (5.24)$$

In terms of the Young's modulus E and Poisson's ratio ν the above stress-strain relations can be written

$$\epsilon_1 = \epsilon_2 = \frac{(1 - \nu)}{E} \sigma_1$$

$$\epsilon_3 = \frac{-2\nu}{E} \sigma_1$$

Thus $\frac{\epsilon_3}{\epsilon_1} = \frac{-2\nu}{1 - \nu}$ (5.25)

By definition, $\frac{\epsilon_3}{\epsilon_1} = \frac{a - c}{1 - a_1}$ (5.26)

Equating (5.25) and (5.26), we get

$$\frac{a_l - a}{a_l - c} = \frac{1 - \nu}{1 + \nu}$$

For coherent layers $a_l = a_o$

Hence,

$$\frac{a - a_o}{a_o} = \frac{1 - \nu}{1 + \nu} \cdot \frac{c_l - a_o}{a_o}$$

$$\text{or, } M = \frac{1 - \nu}{1 + \nu} \cdot m \quad (5.27)$$

Published data [125], are available for ν corresponding to binary compounds. For ternary and quaternary compounds, an appropriate linear interpolation between the binary constituents is made to calculate the value of ν . In general ν is approximately equal to 1/3. Accordingly $M = m/2$.

The mismatch M corresponding to the relaxed lattice parameter of the layer is thus approximately one half of the mismatch calculated from experimental rocking curves. An experimental rocking curve with a mismatch m can therefore be simulated for a mismatch $M = m/2$. In the following sections, the mismatch referred to is the mismatch M , unless otherwise indicated.

A computer program is developed for rocking curve simulation. The program permits use of various reference

crystals, and reflections. Superlattices of various InGaAsP systems are studied. Rocking curves of superlattice structures are generated:

- (1) For $\text{In}_x\text{Ga}_{1-x}\text{As}/\text{GaAs}$ SLS, where indium composition x is varied from 0.1 to 0.4 in four steps keeping number of periods 10 and period epilayer thicknesses 100\AA (well) and 200\AA (barrier) fixed. Figures 5.11 to 5.14 show that due to composition variation satellite peaks vary in position and amplitude.
- (2) For indium composition $x = 0.143$ and epilayer thicknesses of the period 100\AA (well) and 200\AA (barrier) are fixed. Number of periods are increased in steps 10, 30, 60, 80, and 150. Figures 5.15 to 5.19 show the effect of increasing number of periods. Satellite peaks amplitude vary but position remains fixed -2 order peak was observed first increases and then decreases.

Figures 5.20 to 5.24 show where the well and barrier thicknesses are equal 100\AA each, and number of periods increased 10, 20, 30, 40 and 150. The satellite peaks amplitude vary but the position remains fixed.

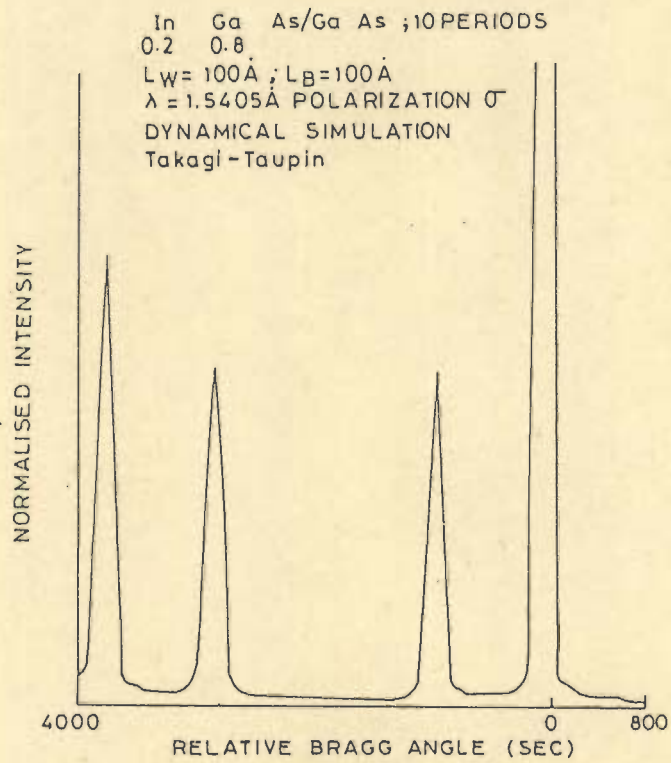
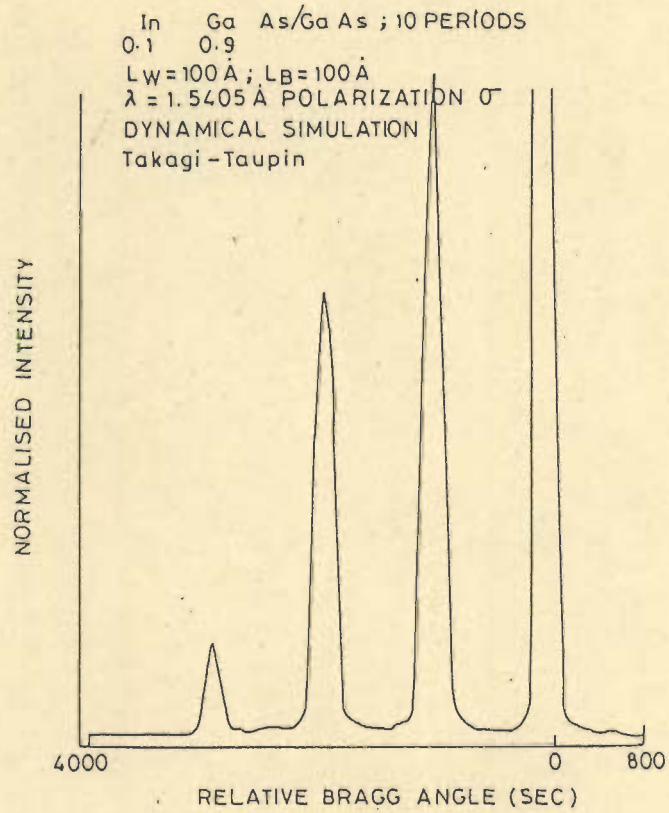


FIG. 5.11 & 5.12

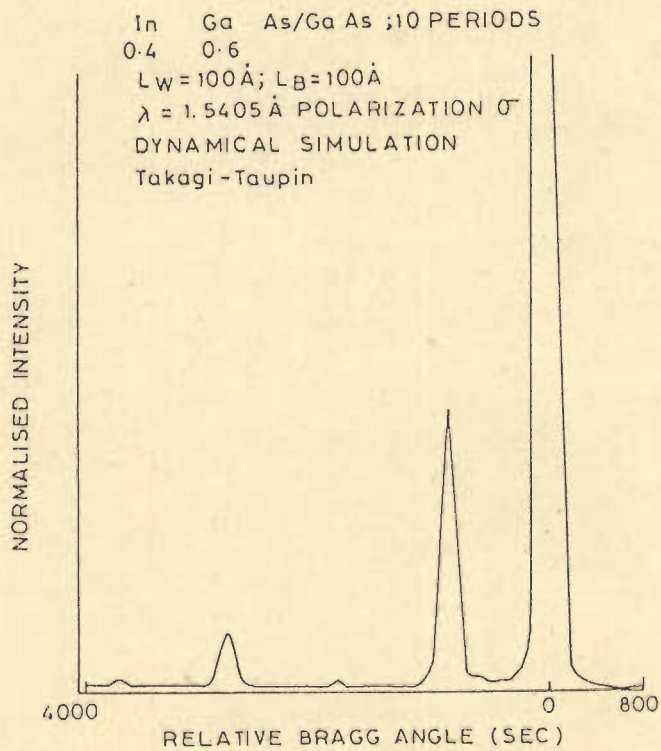
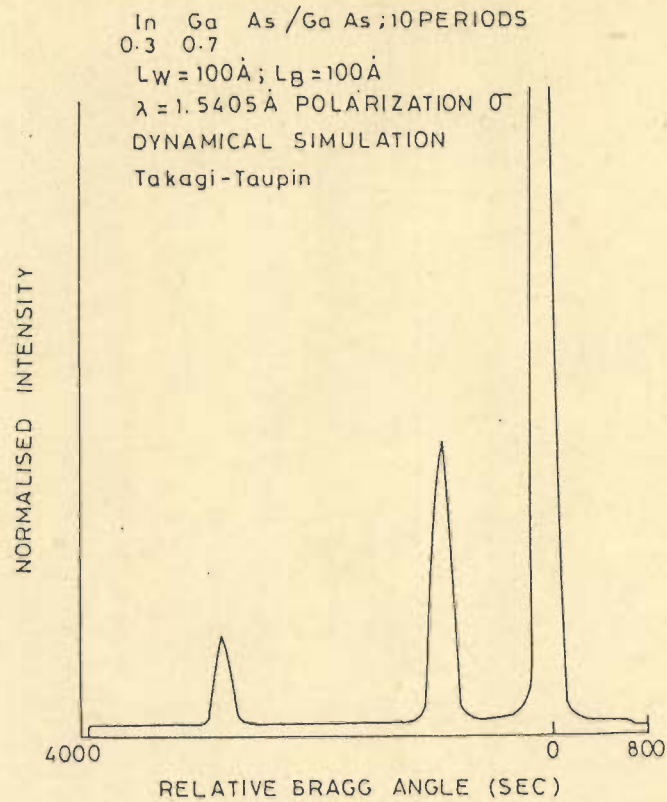


FIG. 5.13 & 5.14

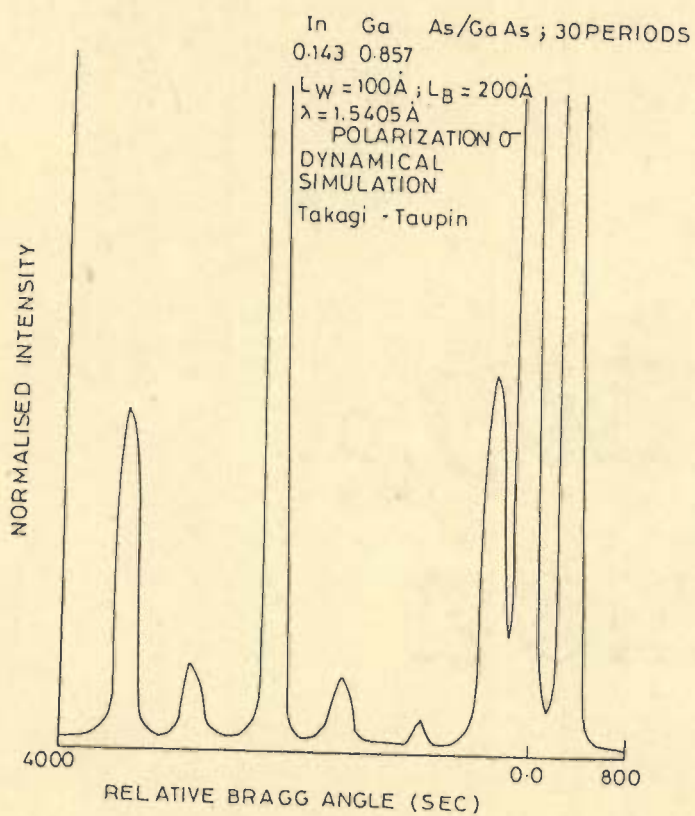
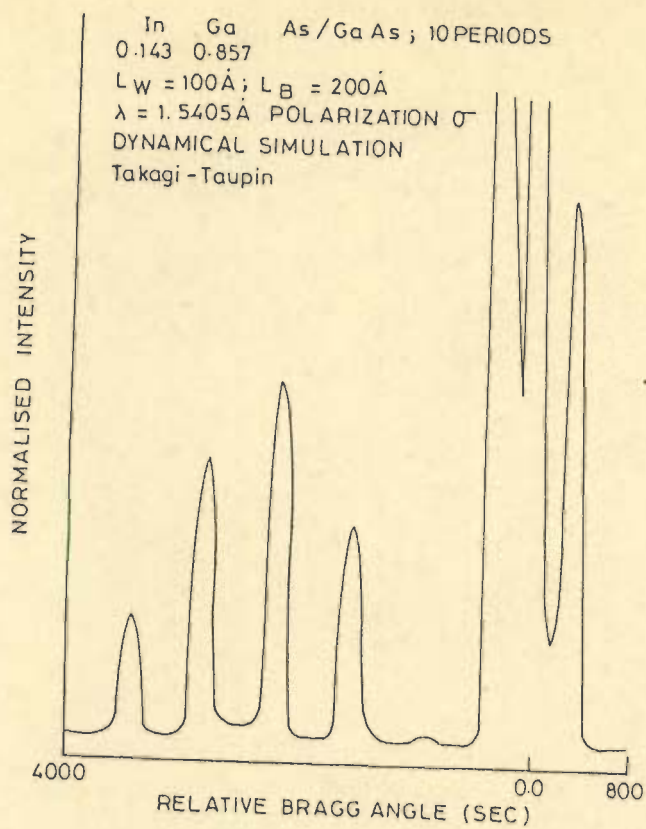


FIG. 5.15 & 5.16

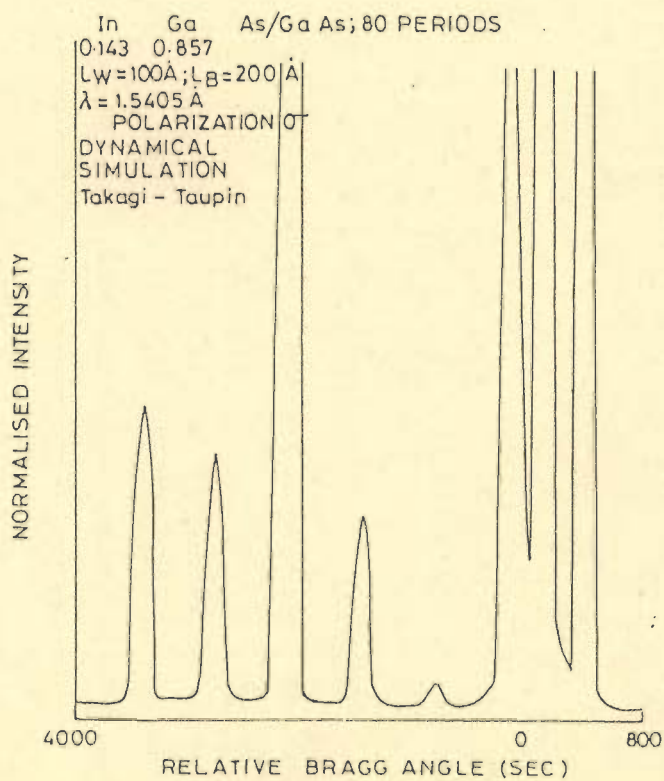
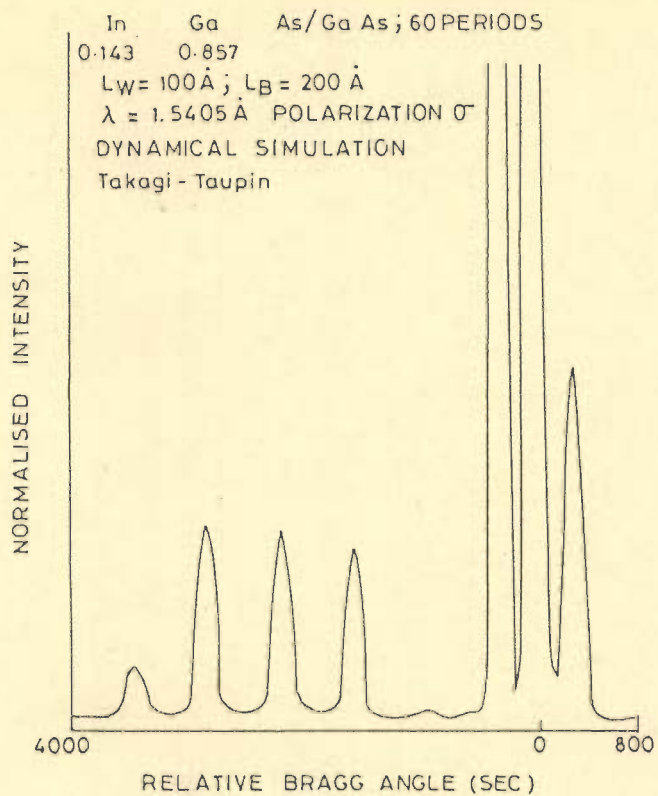


FIG. 5.17 & 5.18

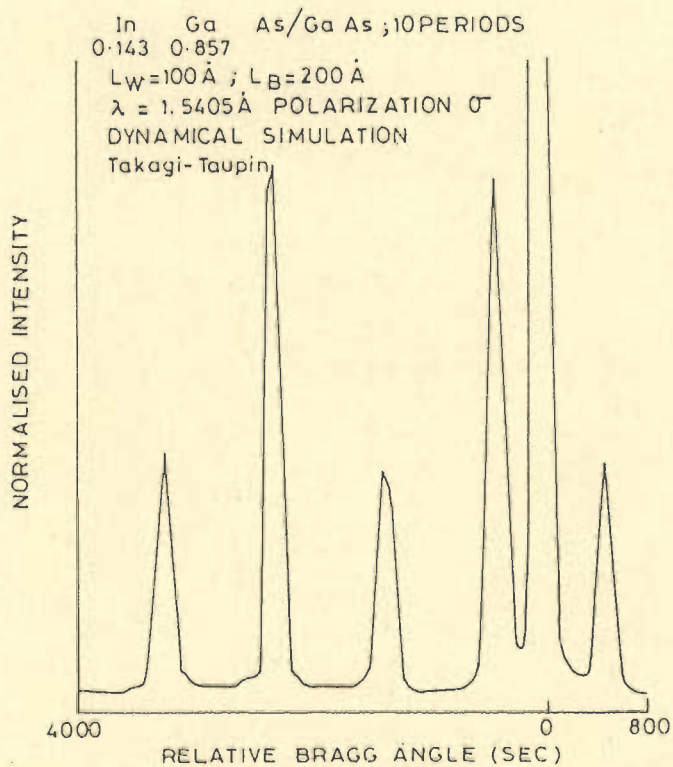
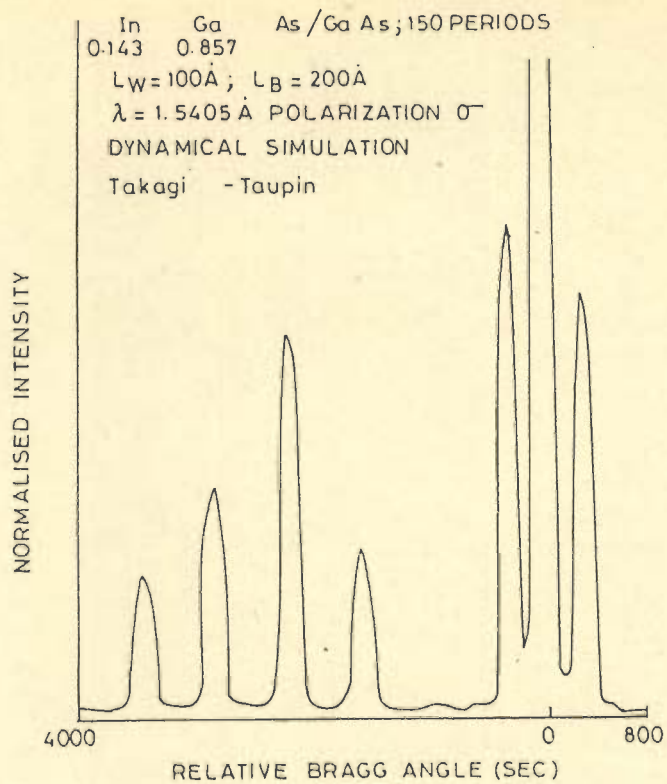


FIG. 5.19 & 5.20

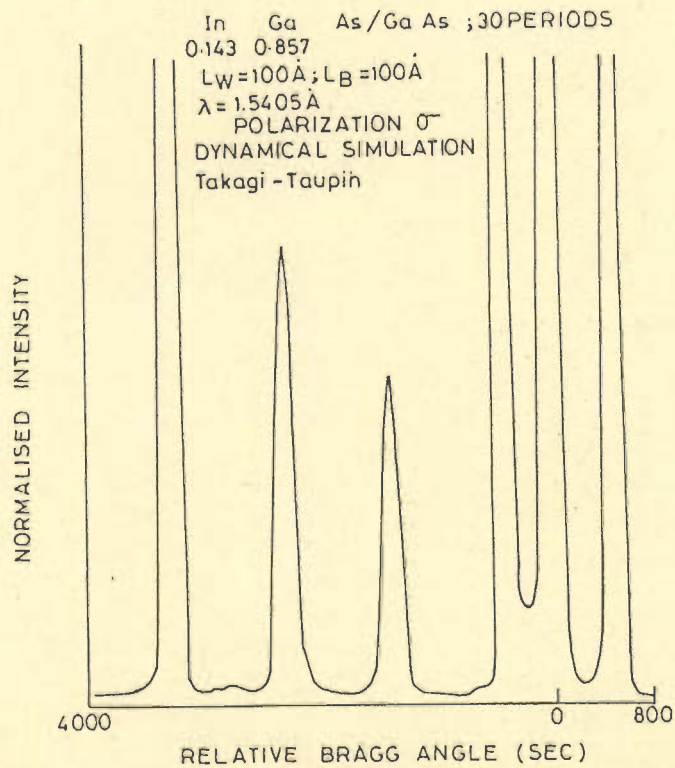
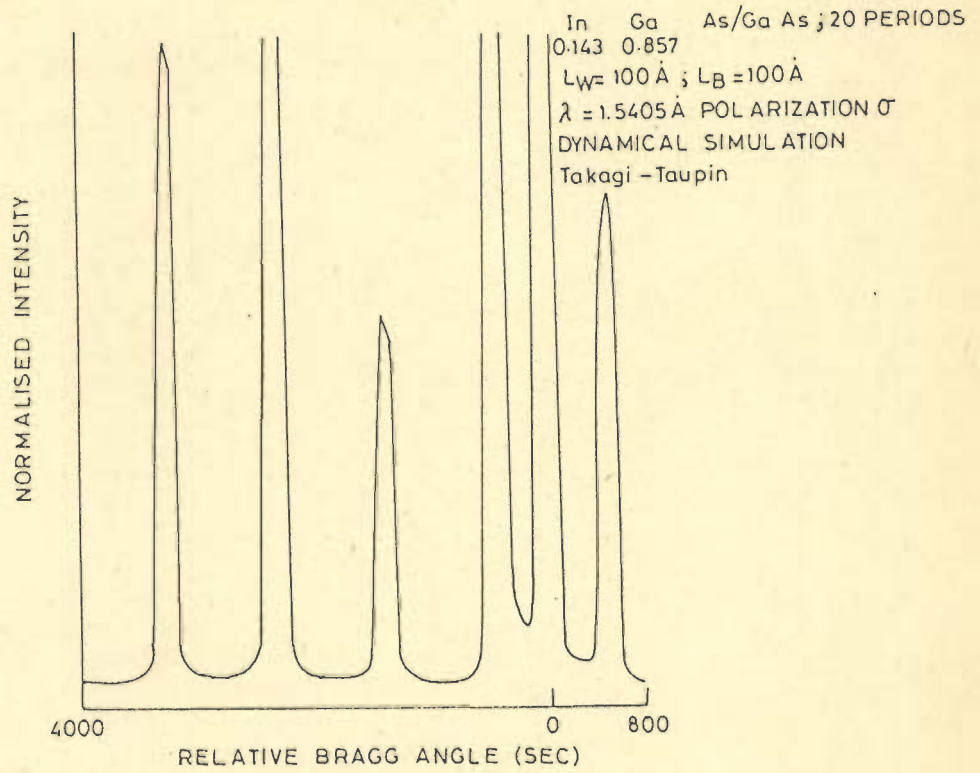


FIG. 5.21 & 5.22

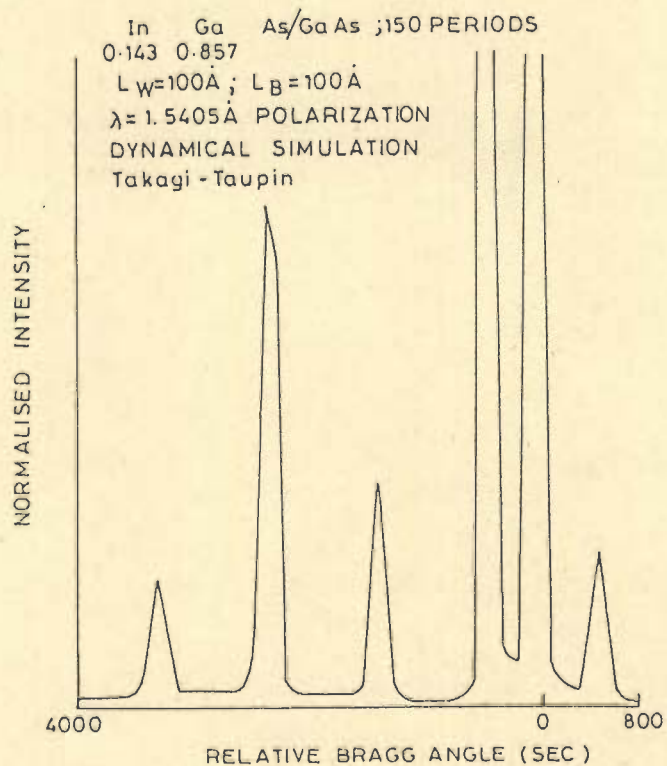
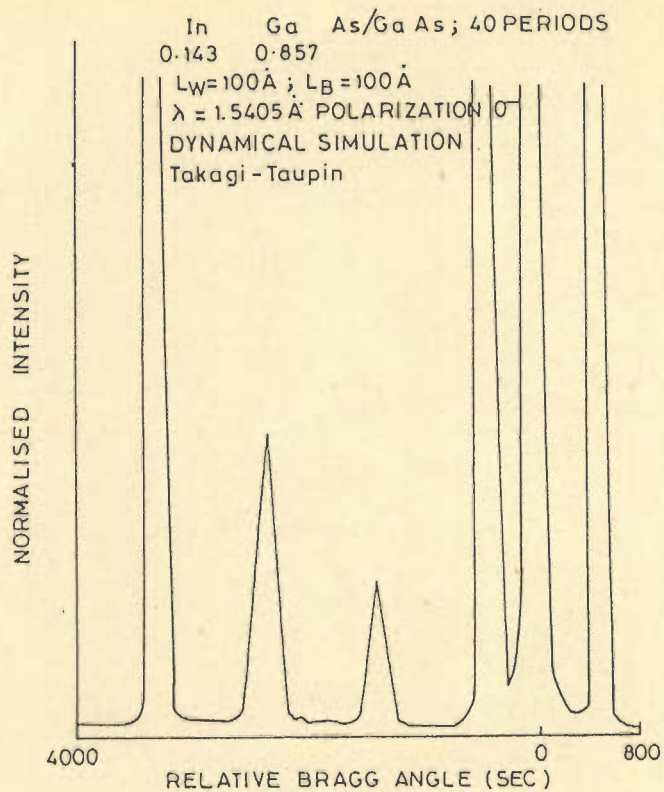


FIG. 5.23 & 5.24

5.4 COMPARISON OF EXPERIMENTAL AND SIMULATED ROCKING CURVES

Experimental rocking curves reported in the literature have been simulated and are analyzed.

(a) InGaAs/GaAs SLS [66,114]:

Figures 5.25 and 5.26 show a close fit achieved for experimental rocking curves by varying the number of monolayers. In the figures substrate peaks are seen along with the satellite peaks. From the position of the zero order peak and first order peak position superlattice period thickness is obtained and compared to with the simulation data. Presence of satellite peaks is a result of composition modulation. The calculated satellite peaks are sharp compared to experimental peaks. In simulation abrupt interfaces are assumed. Table 5.1 shows a comparison of kinematical and dynamical simulation results [129].

(b) InGaAs/InP superlattice [15]:

Figures 5.27 and 5.28 show comparison of experimental and simulated rocking curves. Simulated results are close to the experimental results. Composition modulation has been realized observing satellite peaks. Experimental rocking curves satellite peaks are wider, most of the satellite peak amplitudes

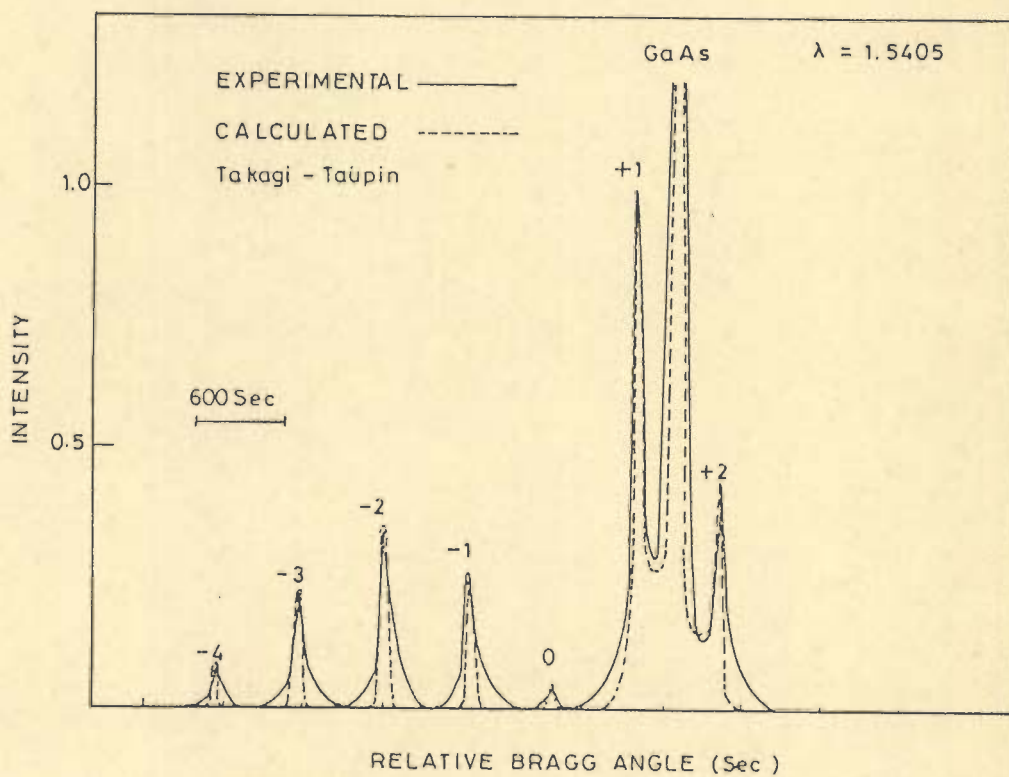


FIG. 5. 25 COMPARISON OF EXPERIMENTAL AND CALCULATED ROCKING CURVES

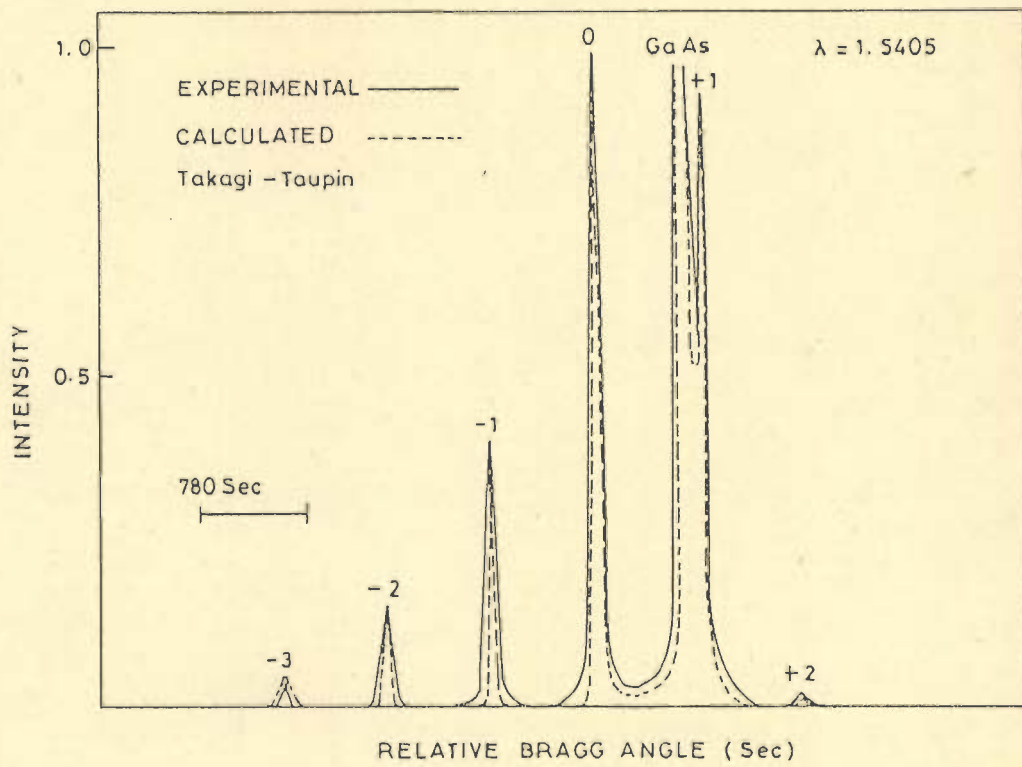


FIG. 5.26 COMPARISON OF EXPERIMENTAL AND ROCKING CURVES

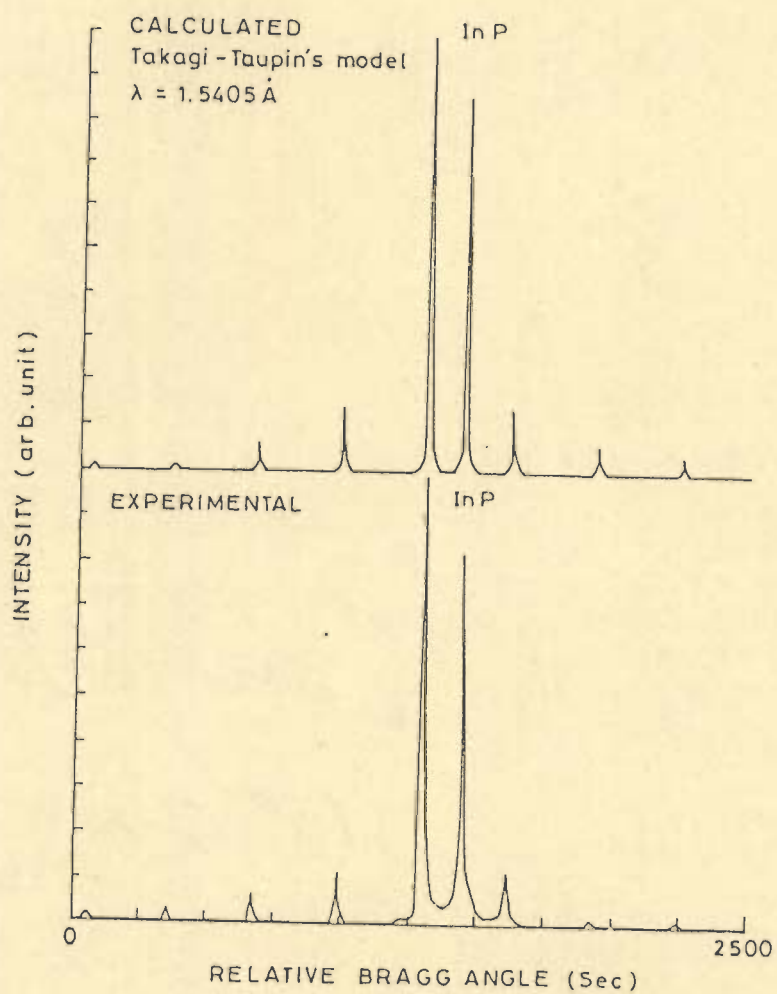


FIG. 5.27 COMPARISON OF EXPERIMENTAL AND CALCULATED ROCKING CURVES

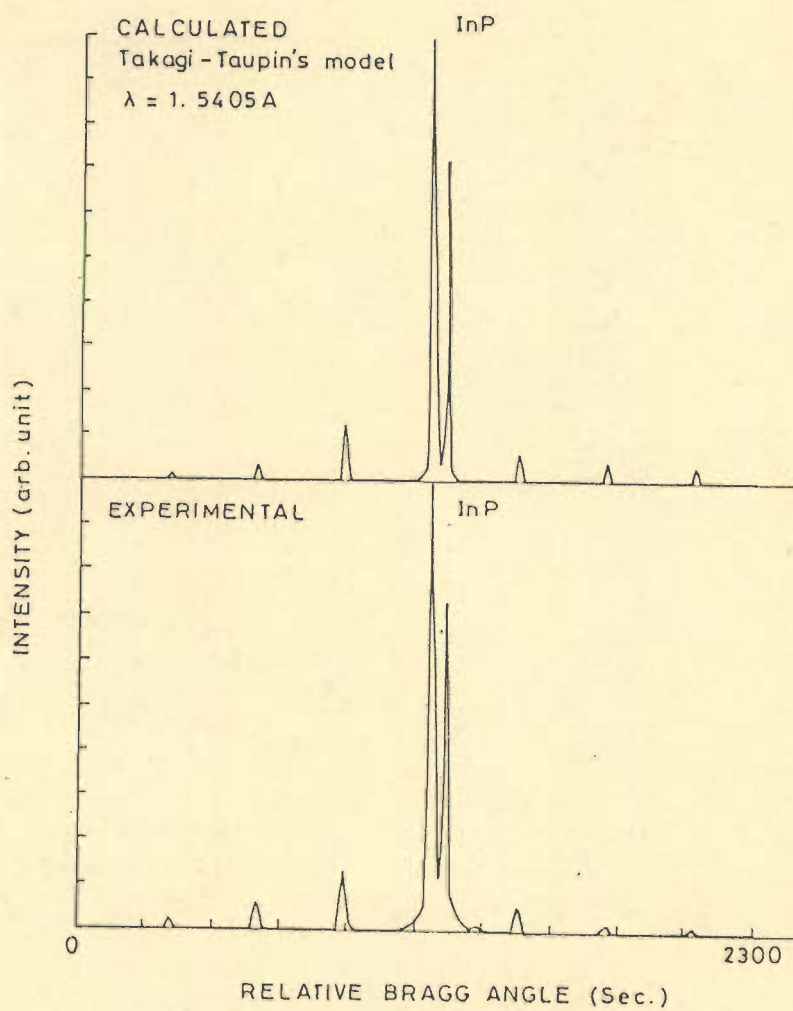


FIG. 5.28 COMPARISON OF EXPERIMENTAL AND CALCULATED ROCKING CURVES

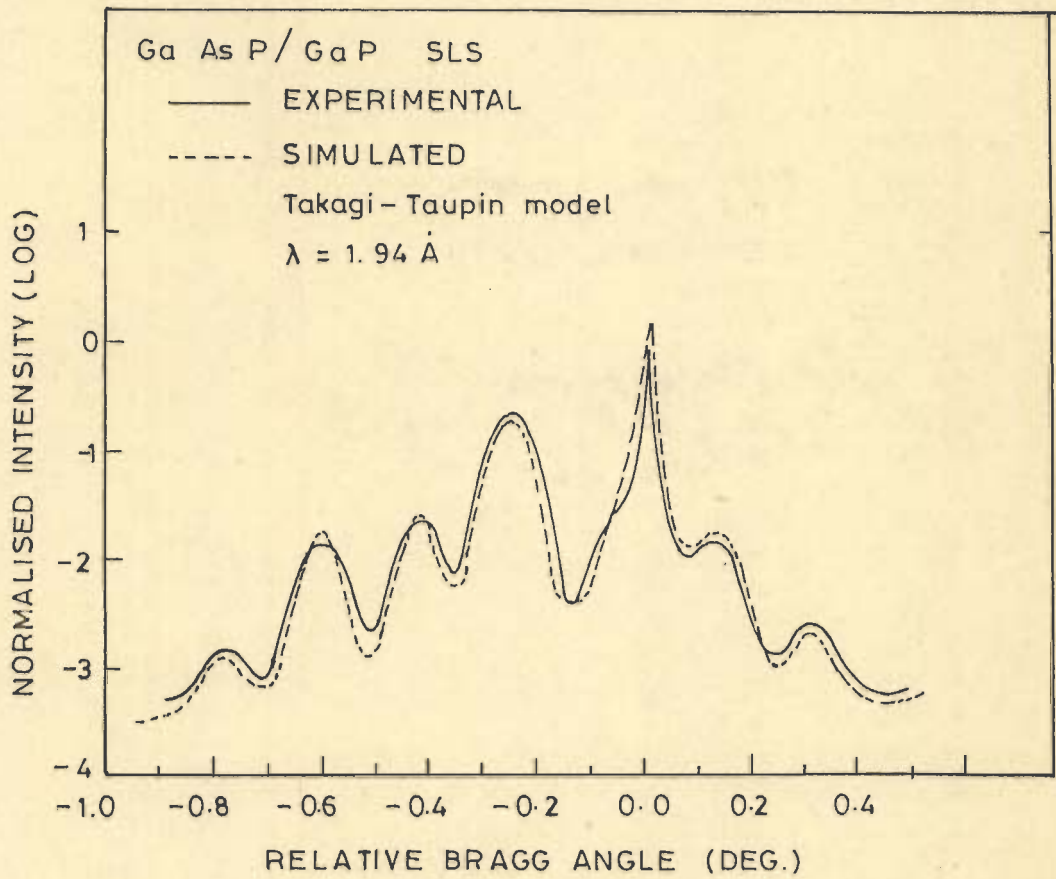


FIG. 5.29 COMPARISON OF EXPERIMENTAL AND SIMULATED CURVES

are matched with experimental results. Since the highest intensity peak within the envelope of superlattice reflections corresponds to a smaller Bragg angle than the substrate it is clear that there is a net positive strain within each period of the superlattice.

(c) GaAsP/GaP SLS [91]

Figure 5.29 shows comparison between experimental and simulated rocking curves. The rocking curve profiles are in logarithmic scale. It is clear that in addition to the substrate peak there is a family of periodic superlattice reflections due to the presence of a periodic strain in the growth direction. The spacing of the peaks gives an accurate determination of the superlattice period.

5.5 CONCLUSION

From the generation of various rocking curves it is possible to study the nature of rocking curves how they change with the changes in composition, number of periods and well and barrier thicknesses. Various rocking curves obtained from kinematical model show that it is necessary to use dynamical theory if the total layer thickness is large (greater than $1 \mu\text{m}$).

Kinematical and dynamical simulation techniques applied to same InGaAs/GaAs SLS specimen, it has been observed that the dynamical results are more close to experimental results. By matching simulated rocking curves to experimental data it is possible to determine detailed strain distribution within individual layers of the superlattices.

CHAPTER 6

CHARACTERIZATION OF THERMALLY ANNEALED AND Zn DIFFUSED
SUPERLATTICES FROM ROCKING CURVE SIMULATION METHOD

6.1 INTRODUCTION

Since the discovery of impurity induced layer disordering in 1980 by Laidig et al [83] while attempting to modify undoped AlGaAs/GaAs superlattices to doped superlattices, there has been a growing interest:

- (1) to understand disordering mechanism in the superlattices.
- (2) to understand the crystal and defect diffusion process inherent in layer disordering.
- (3) to utilize the impurity - induced layer disordering process for device fabrication.

Laidig et al [83, 84] found that for GaAlAs/GaAs quantum well heterostructure when thermally annealed at 925°C for more than two hours the quantum well disappeared and an average composition GaAlAs layer was observed. Similar results were observed using Auger spectroscopy for an AlAs/GaAs superlattice when annealed at 800°C for two hours [28, 74, 83, 93].

In another experiment Laidig et al [84] showed that the layers of an AlAs/GaAs superlattice are unstable against Zn diffusion.

The Zn diffusion yielded a bulk undamaged homogeneous material of an Al composition average to that of original

superlattice; this process occurs at much less temperature than those studied by ordinary thermal annealing. This happens due to intermixing of superlattice layers commonly called interdiffusion, which in this case is between Ga and Al. Few more experiments were performed on InGaAs/GaAs SLS and similar interdiffusion between In and Ga by thermal annealing [66] and Zn diffusion [85] have been reported. A study of layer disordering mechanism in SLS structure is therefore very important. There are number of characterization techniques that are sensitive to changes occurring at the heterointerfaces. These include Auger spectroscopy [75, 85], photoluminescence [1, 62, 120], TEM [29, 75]. Nomarsky micrograph [85], and X-ray double crystal diffraction [66, 85, 53].

In the present chapter a detail study of disordering mechanism due to thermal annealing and Zn diffusion has been made, based on which experimental rocking curve of thermally annealed and Zn diffused SLS structure as reported in the literature were used to simulate rocking curves using the dynamical theory of X-ray diffraction. By comparing the experimental and simulated rocking curves the interdiffusion of In-Ga as well as composition depth profile for various annealing time have been obtained.

6.2 DISORDERING DUE TO THERMAL ANNEALING

When an InGaAs/GaAs SLS structure undergoes thermal annealing, Gallium atoms from GaAs layer diffuses into the grain boundaries of InGaAs layer creating Ga vacancies in the GaAs. Indium diffuses into GaAs forming a new $\text{In}_y\text{Ga}_{1-y}\text{As}$ layer at the interface. In the same way gallium atom diffuses into $\text{In}_x\text{Ga}_{1-x}\text{As}$ layer. At the annealing temperature gallium and indium atoms become more mobile. For the temperature range of thermal annealing, arsenic loss is insignificant. When the annealing reaches a critical value at which the layer $\text{In}_y\text{Ga}_{1-y}\text{As}$ gets saturated with indium, further out migration of indium atom from $\text{In}_x\text{Ga}_{1-x}\text{As}$ layer is prevented even if the temperature is increased. Figure 6.1 shows the diffusion of Ga and In atoms in a single period of the SLS structure. The composition variation x in the single period of SLS structure has been obtained applying Fick's second law in one dimension as

$$\frac{\partial x(z,t)}{\partial t} = \frac{\partial}{\partial z} \left[D \frac{\partial x(z,t)}{\partial z} \right] \quad (6.1)$$

where $x(z,t)$ is the composition variation at position z and time t , and D is the diffusion coefficient. Diffusion coefficient can be deduced by applying appropriate boundary conditions, and approximated as [52, 66, 116, 139].

$$x(z,t) = \frac{1}{2}x_0 \left[\text{erf}\left(\frac{Lz/2-z}{2\sqrt{Dt}}\right) + \text{erf}\left(\frac{Lz/2+z}{2\sqrt{Dt}}\right) \right] \quad (6.2)$$

where $x(z,t)$ is the indium composition at annealing time t

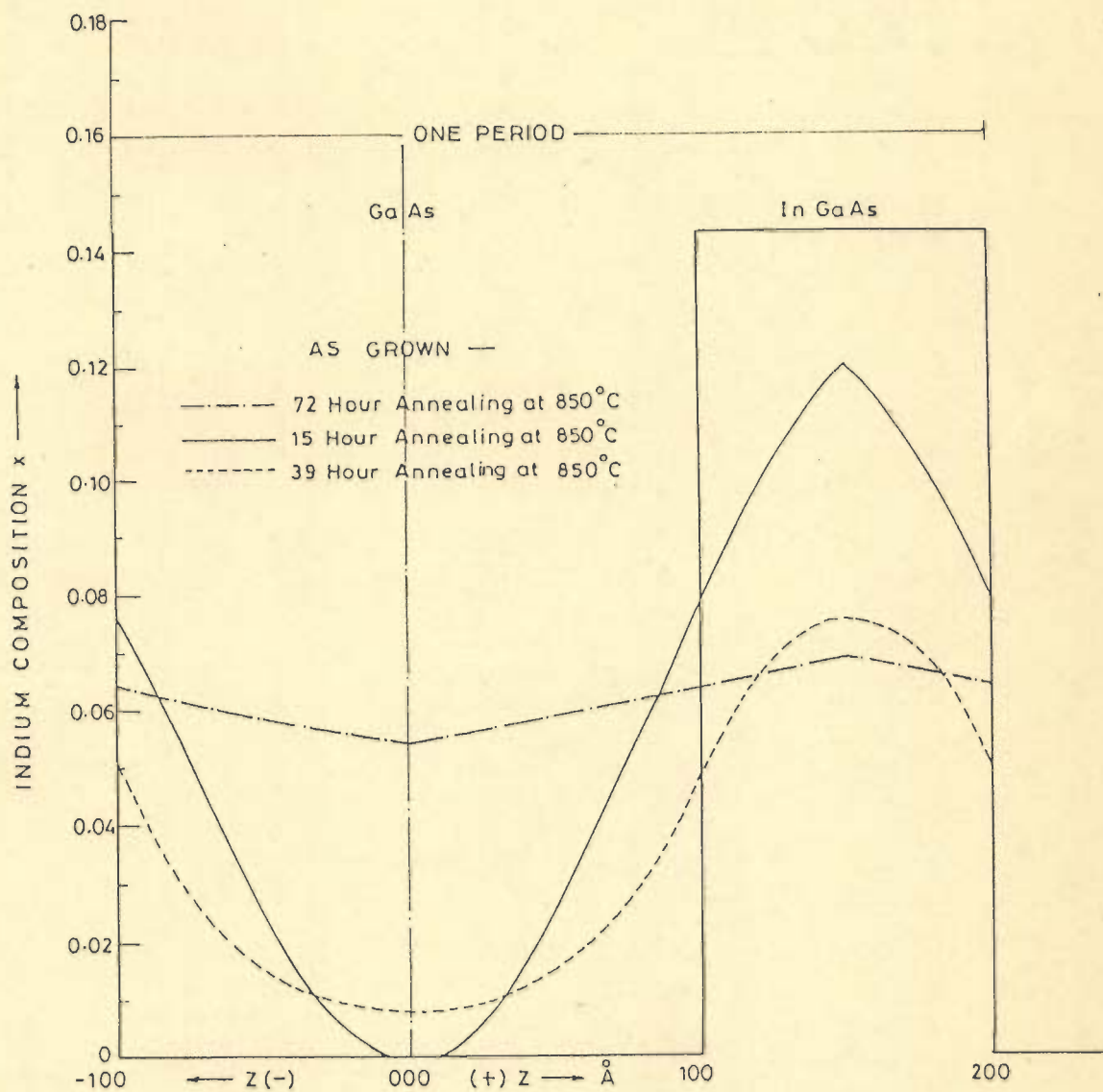


FIG. 6.1 CALCULATED COMPOSITION PROFILES WITH AND WITHOUT ANNEALING

and depth position z , $z=0$ is the centre of the quantum well. Lz is the quantum well thickness, x_0 is initial composition of indium, and D is In-Ga interdiffusion coefficient.

In the present studies $\text{In}_x\text{Ga}_{1-x}\text{As}/\text{GaAs}$ SLS structure annealed at 850°C for 15 hours, 39 hours, and 72 hours reported in the literature have been analyzed using dynamical model developed in chapter five. Assuming a suitable interdiffusion coefficient D , the annealed composition/depth profiles for 15, 39, and 72 hours have been calculated using equation (6.2) as shown in Figure 6.1.

6.3 ROCKING CURVE SIMULATION

Once the composition/depth profile for a single period is obtained, corresponding to each depth position z and composition x the structure factor F can be calculated as described in chapter five equation (5.12). Takagi-Taupin derivation is then used to calculate diffraction intensity as a function of Bragg angle. Rocking curves are simulated and a perfect match for each 15, 39, 72 hours of annealing at 850°C have been achieved as shown in Figure 6.2. The various interdiffusion coefficients D for In-Ga as used in the simulation for different annealing times are as shown in Table 6.1.

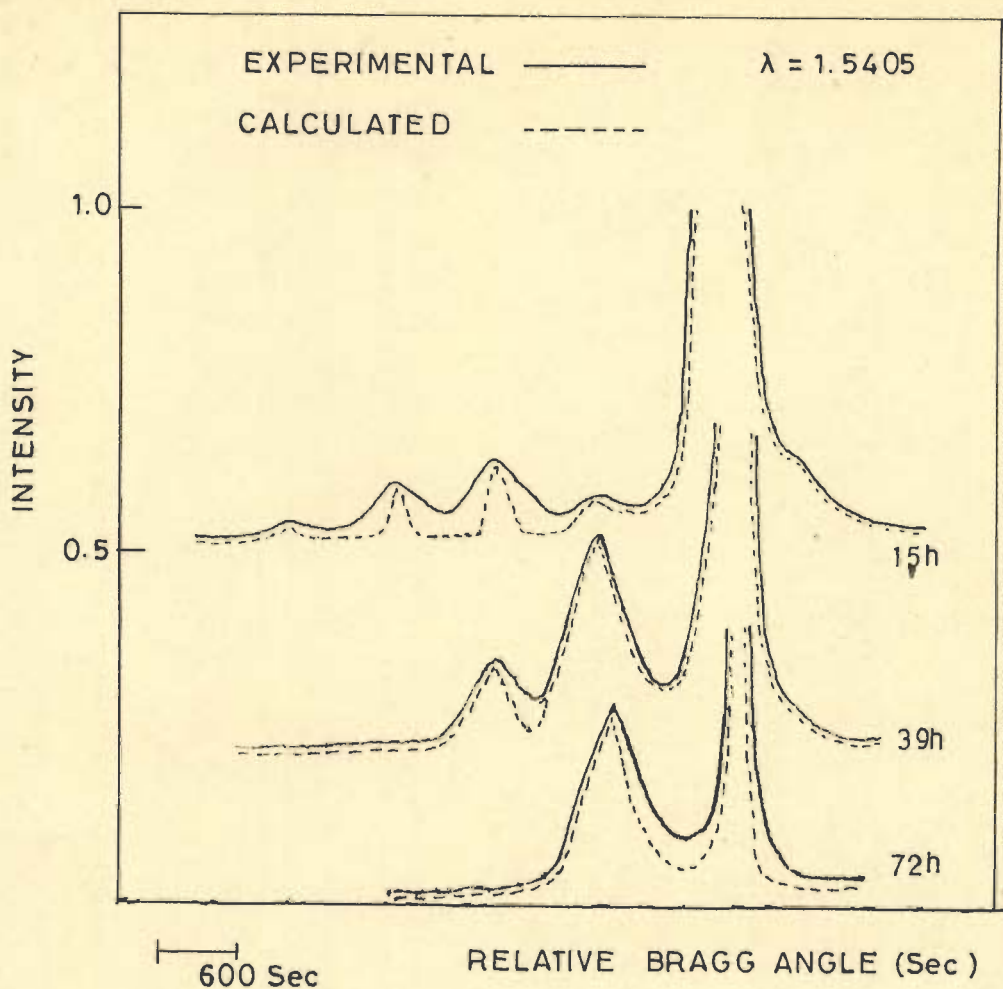


FIG. 6.2 COMPARISON OF EXPERIMENTAL AND CALCULATED ROCKING CURVES

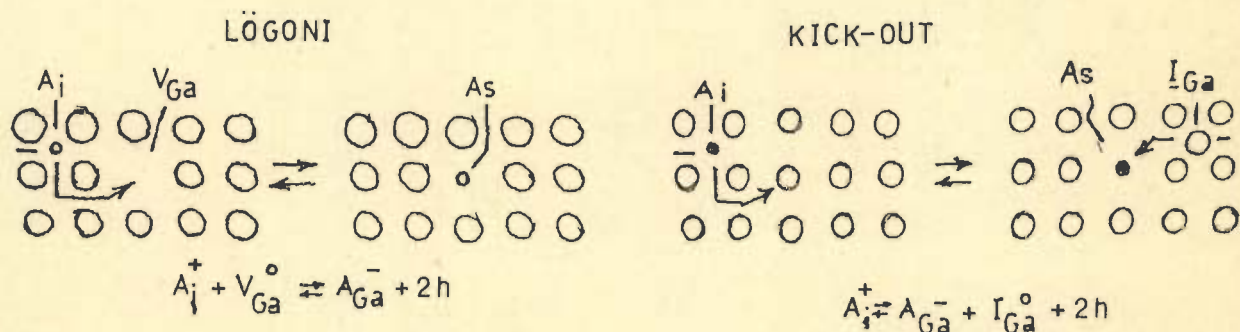
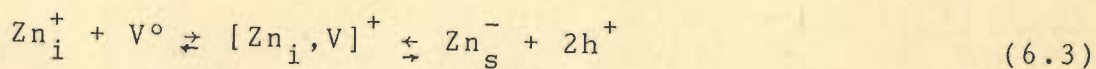


FIG. 6.3

6.4 DISORDERING DUE TO Zn DIFFUSION

The disordering of SLS structure by layer interdiffusion/intermixing caused by thermal annealing takes place at temperature greater than the crystal growth temperature. Layer disordering can be accomplished at much lower temperatures than the crystal growth temperature, e.g., by Zn diffusion which greatly enhances the interdiffusion of In and Ga atoms [29,85,86,87,116]. Recent data [86, 29] show that the interstitial-substitutional mechanism [29, 52] for Zn diffusion [117] in InGaAs/GaAs SLS [85] and in AlGaAs/GaAs superlattices [83, 74] have been reported, must be modified to include the formation of Zn-vacancy pairs represented by [29, 83]



where V° is neutral vacancy, h^+ is hole, and Zn_i , Zn_s are interstitial and substitutional Zn respectively.

In 1961, Logini [88] proposed that Zn diffuses through an interstitial substitutional mechanism in which the Zn as an interstitial acts as a donor-type defect and diffuses rapidly. In 1981, Gosele and Morehead [50] suggested that the column III interstitial is created directly by an interstitial Zn moving into a column III lattice site through a 'Kick-out' mechanism. Logini and Kick-out mechanism shown in Figure 6.3.



Since the substitutional Zn_{III}^- concentration due to Zn diffusion in GaAs is typically $5 \times 10^{19} \text{ cm}^{-3}$, equation (6.4) suggests that the Zn-diffused region will contain a high concentration of column III interstitial defects. This high concentration of column III interstitial defect offers a basis for impurity-induced layer disordering via Zn diffusion that was first discovered by Laidig et al [83, 29].

There is evidence that Zn diffusion enhances interdiffusion on the anion sublattice, as reported for a GaAsP/GaP SLS [91, 49], as well as the cation sublattice in InGaAs/GaAs SLS [87]. In SLS structures in which the layer thickness is $50\text{-}300\text{\AA}$ the interdiffusion distance necessary for mixing layers is so short that even slightly enhanced anion interdiffusion can effectively produce disordering in a short time [85, 87].

6.5 ROCKING CURVE SIMULATION FOR Zn DIFFUSED SLS

For the rocking curve simulation of Zn diffused SLS, it is required to calculate the composition/depth profile for a single period, assuming appropriate In-Ga interdiffusion coefficient D . D is assumed on the basis of experimental data of the SLS growth available [85]. The composition/depth profile is calculated as [52, 116].

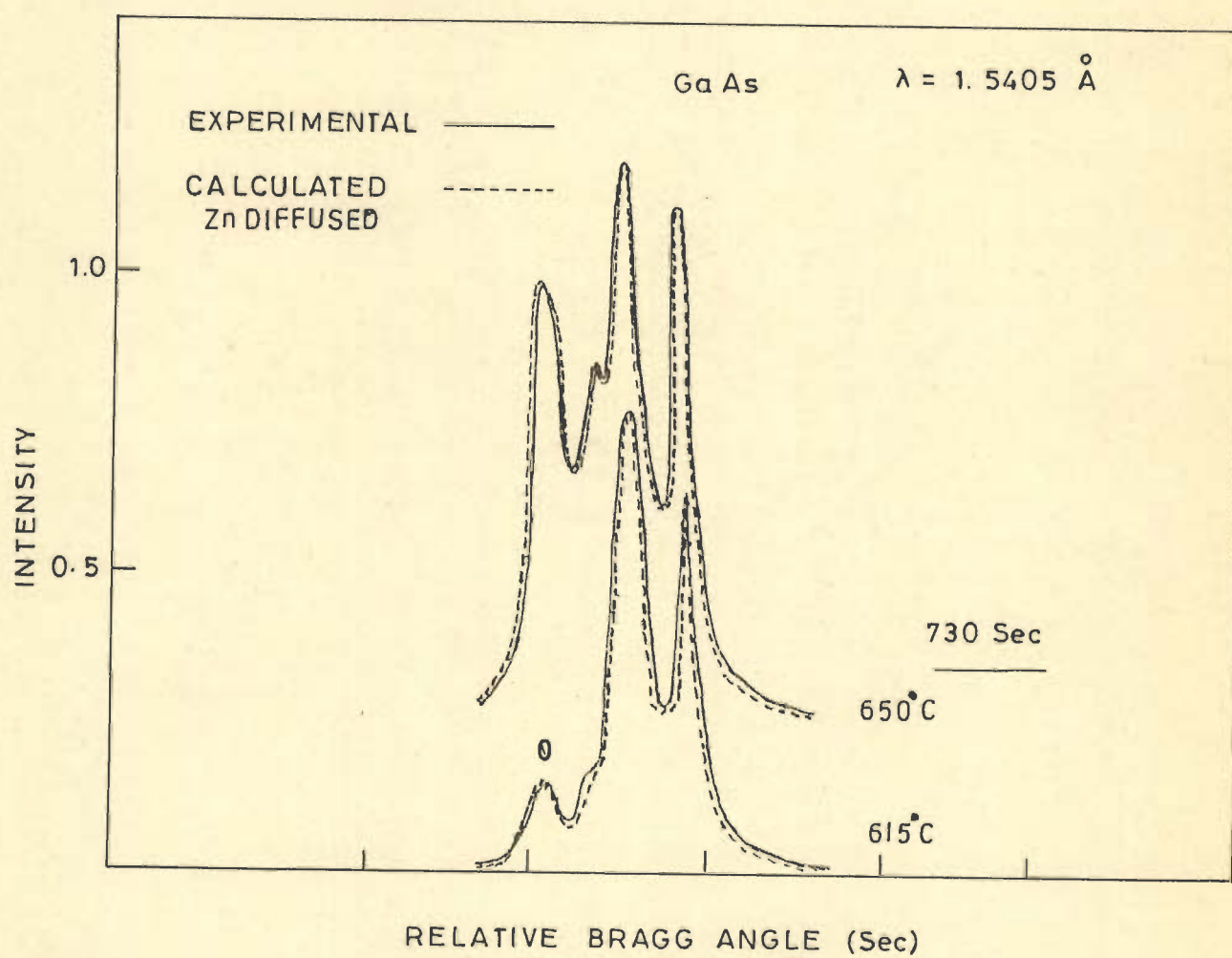


FIG. 6.4 COMPARISON OF EXPERIMENTAL AND CALCULATED ROCKING CURVES

$$x_d(t) = x_o - \frac{1}{L_z} \int_{-L_z/2}^{+L_z/2} x(z,t) dz \quad (6.5)$$

The integration gives [26]

$$x_d(t) = x_o \left\{ 1 - \operatorname{erf}\left(\frac{Lz}{2\sqrt{Dt}}\right) + \frac{2\sqrt{Dt}}{Lz\sqrt{\pi}} \left[1 - \exp\left(-\frac{Lz^2}{4Dt}\right) \right] \right\} \quad (6.6)$$

using this equation (6.6) indium composition/depth profiles are calculated for InGaAs/GaAs SLS Zn diffused at 680°C and 615°C both for one hour.

Using the same dynamical model based on Takagi-Taupin derivation rocking curves are simulated. By repeatedly changing the value of D a close fit to the experimental rocking curve reported in the literature, have been achieved as shown in Figure 6.4. Thus, In-Ga interdiffusion coefficient D have been obtained as shown in Table 6.1.

6.6 D CALCULATION FROM EXPERIMENTAL ROCKING CURVES (WITHOUT SIMULATION)

When an InGaAs/GaAs SLS is thermally annealed at a temperature of 850°C for 15, 24, 39, and 71 hours respectively. The experimental rocking curve shows changes in the amplitude of satellite peak, all the satellite peaks do not show the same evolution. The intensity of -5th and -4th order decreases rapidly whereas -1 order first increases then vanishes, the zero order satellite intensity increases

until saturation after 71 hours annealing at this stage it is the only remaining diffraction peak as shown in Figure 6.5(a). This zero order peak correspond to an average ternary InGaAs layer over a GaAs substrate, and all the superlattice periods are disordered or intermixed.

In the same way when InGaAs/GaAs SLS Zn diffused for one hour at temperature 615°C and 680°C, the experimental rocking curve show changes corresponding to each temperature as shown in Figure 6.5(b) [66]. The zero order satellite peak evolution show that SLS period completely disordered/intermixed and an average composition InGaAs layer formed on a GaAs substrate.

In both the cases (thermally annealed and Zn diffused SLS) the X-ray diffraction rocking curve measurements show that the satellite peak intensities relative to zero order peak intensity decreases with annealing time. The rate of decay of these satellite peaks is related to the interdiffusion coefficient D [14, 19, 53, 60]. In the present section Chan's modified model [19] has been used to calculate interdiffusion coefficient D .

6.7 CHAN'S MODEL CALCULATION

In order to explain interdiffusion results, the theoretical analysis is done directly from experimental rocking

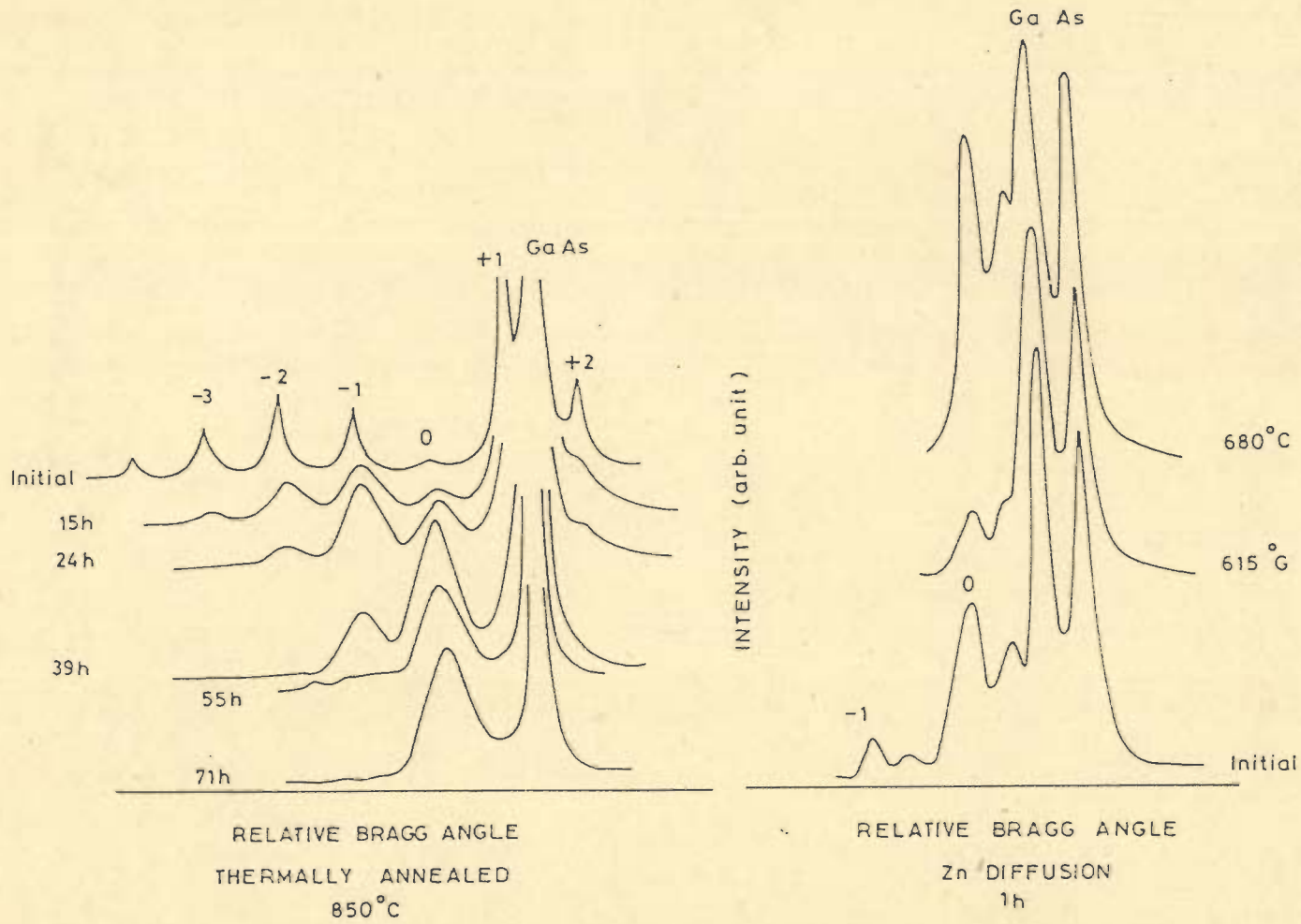


FIG. 6.5 EXPERIMENTAL ROCKING CURVES

curves. The compositional modulation can be described as a Fourier sum in direct space [60] as

$$x(z) = x_0 \left[1 + \sum Q_n \cos\left(\frac{2\pi}{\Delta} nz\right) \right] \quad (6.7)$$

where $x(z)$ is the indium composition in the growth direction z , x_0 is the average concentration, Q_n is the amplitude of the n th harmonic of the wave vector $2\pi/\Delta$ and Δ is the period of SLS. The composition profile of the SLS without thermal annealing is expressed as a square-wave modulation of composition shown in Figure 6.1. This square composition profile is changed to a graded composition after intermixing due to annealing and diffusion.

The diffusion coefficient D can be obtained by solving Fick's differential equation for time dependence of the Fourier coefficient Q_n can be obtained [19] as

$$Q_n(t) = Q_n(0) \exp[(-nk)^2 Dt] \quad (6.8)$$

where D is interdiffusion coefficient, $k = 2\pi/\Delta$. The $\log(Q_n)$ v/s time plot shows a linear variation slope of $-(nk)^2 D$ as shown in Figure 6.6. Q_n decreases linearly with annealing time. From the slope of $\log(Q_n)$ versus time t the values of D are obtained.

In table 6.1 a comparison of interdiffusion coefficients calculated directly from the experimental rocking-curves

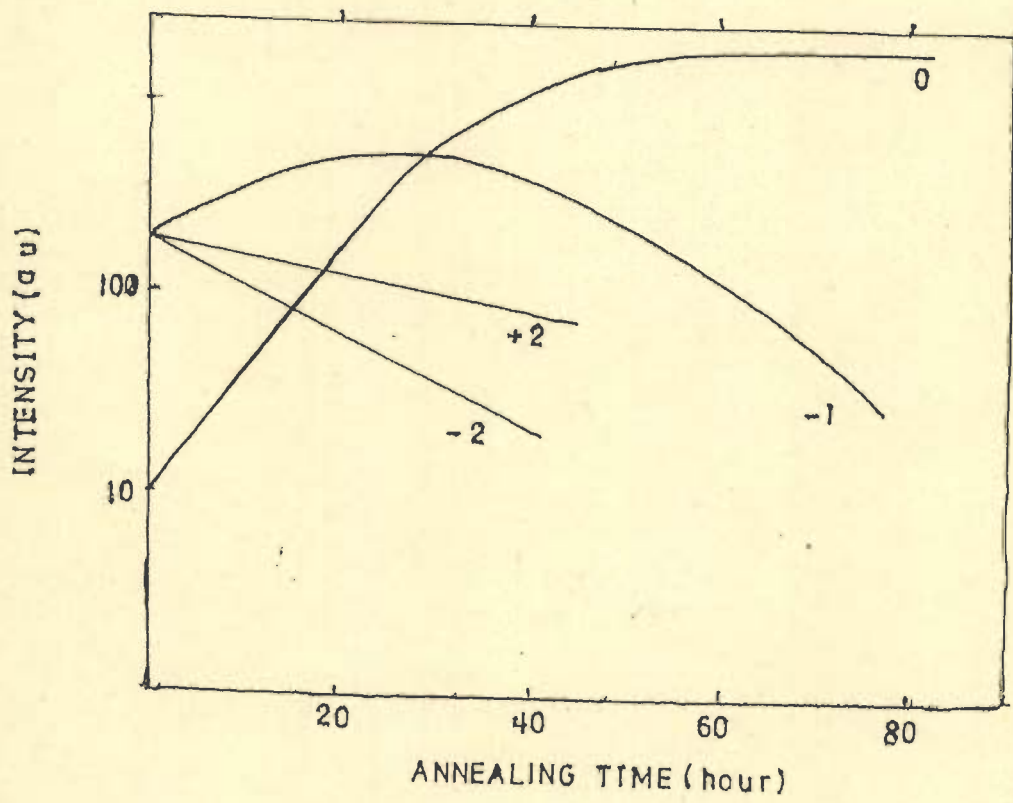


FIG. 6.6 EVOLUTION OF SATALLITE INTENSITIES

Table 6.1 : In-Ga INTERDIFFUSION COEFFICIENT D

SLS	Anneal- ing tem- perature (°C)	Anneal- ing time (h)	D calculated from experi- mental Rocking curves (cm ² /s)	D obtained from simulation [131] (cm ² /s)
	850	15	1.1×10^{-18}	2×10^{-18}
InGaAs-GaAs thermally annealed	850	24	1.9×10^{-18}	2×10^{-18}
	850	39	2.1×10^{-18}	2×10^{-18}
	850	35	3.3×10^{-18}	2.4×10^{-18}
	850	71	2.7×10^{-18}	2.4×10^{-18}
InGaAs-GaAs Zn diffused	615	1	2.4×10^{-17}	3×10^{-17}
	680	1	4.0×10^{-16}	3.2×10^{-16}

is made with those calculated from simulation method [132].

6.8 CONCLUSION

The effect of thermal annealing and Zn diffusion on X-ray rocking curves have been observed and analyzed. The compositions have been modelled in the real space, assuming

- (a) plain diffusion process for thermally annealed process and,
- (b) interstitial-substitutional mechanism for Zn diffusion process.

The diffraction profiles are calculated on the basis of dynamical model [131]. Using Chan's model the interdiffusion coefficients D have been obtained directly from experimental rocking curves and are compared with the simulated rocking curve data. The similar results have been observed, in both the methods. Interdiffusion enhancement due to Zn-diffusion process at lower temperature, and complete disorder of SLS structures have been found in the rocking curves. Calculated rocking curves are sharper than the experimental curves, it is difficult to obtain an accurate determination of the intensities of satellites +1 and +2 which rapidly merge with the substrate diffraction peak.

CHAPTER 7

EFFECTS OF IONIMPLANTATION ON SUPERLATTICES

7.1 INTRODUCTION

Studies on the effects of ion-implantation on SLS have been found useful, in order to calculate strain/damage caused by implantation process. For many optoelectronic devices ion-implantation of donor (e.g. Si and Se) or acceptor (e.g. Be, Cd and Zn) dopants would be desirable [1,106,138,149]. Ion-implantation process can however, introduce lattice damage and additional strain in SLS materials [1,91]. This strain induced in ion-implanted materials can be conveniently measured using the cantilever-beam technique developed by Eer Nisse [91]. This method utilized the strain induced bending of a sample in the form of a thin beam clamped at one end. Measurement of the bending during implantation yields quantitative measurement of the implantation induced strain in the near surface region. Analysis of the measured strain using the elastic constraints of the underlying undamaged, material permits evaluation of the resulting total stress integrated over the damage depth.

Rutherford back scattering spectrometry has been used to monitor lattice disorder produced by the various implants [1,91]. Double crystal X-ray diffraction technique has also been used to study ionimplanted crystals [106,142,149], and SLS structures [91,149]. X-ray diffraction technique has been found advantageous over other techniques because, this technique can provide information regarding implantation-induced disordering of SLS.

In this chapter effects of beryllium implantation on the GaAsP/GaP SLS structure have been characterized, using dynamical X-ray diffraction rocking curve simulation technique [133].

7.2 CHARACTERIZATION METHODS

Low-dose implantation of dopant atoms is an important part of the preparation of many (GaAs) (InP) devices. Ion-implanted crystal or SLS structure can be characterized by using cantilever beam bending, Rutherford back scattering, and X-ray double crystal diffraction [1,91,138]. Among all these methods, X-ray diffraction is the nondestructive method, and reveal high precision results regarding strain/damage, or layer disordering in the case of SLS structures.

The rocking curve simulation technique is the most accurate method of characterizing ion-implanted crystals and SLS structures [91,124,149]. In this technique experimental rocking curves are simulated and a close fit to experimental curves is obtained by varying assumed strain/damage-depth parameter.

In the next section the dynamical theory of X-ray diffraction has been applied to simulate the rocking curves for ion-implanted SLS structure.

7.3 ROCKING CURVE SIMULATION

It has been reported that ionimplantation induces lattice strain and lattice distortion in the epilayer [1,24] and in the SLS [91,124] structure also. Displacement damage from the implantation causes an expansion of the implanted surface region due to point defect generation [1,82,138].

When the homogeneity of the crystal specimen varies in only one direction i.e., in depth with no lateral variation, the change in the X-ray complex amplitude with depth is well described by Takagi-Taupin derivation [143]. An iondamaged crystal is divided into an arbitrary number of parallel laminae each having an average strain and damage uniform. Damage is random displacement of atoms from their lattice sites, and have been assumed to have the form of a spherically symmetric Gaussian function [123]. Many workers have reported that this damage linearly varies with strain

$$(\text{Damage}) U \propto \epsilon^{\perp}(\text{strain}) \quad (7.1)$$

where ϵ strain has unit of per cent and U is in \AA° .

The strain produces tetragonal distortion in the layers so that the lattice spacings along the growth direction are alternately larger (for the well) or smaller (for the barrier) than the in plane spacing of the SLS. This perpendicular strain in the growth direction is obtained in terms

of lattice spacing as

$$\epsilon^{\perp} = (a^{\perp} - a_0)/a_0 \quad (7.2)$$

where a^{\perp} is the lattice spacing of the well (ternary layer), and a_0 is the lattice spacing of barrier (substrate material).

Further it is observed from the literature that the damage reduces the structure factor in the same way as thermal vibration smear out the atomic positions [59]. Therefore modified structure factor can be obtained as

$$F_H = \exp(-q^2 \langle U^2 \rangle / 2) \quad (7.3)$$

and $q = 4\pi \sin\theta / \lambda$, therefore finally

$$F_H = \exp\left(-\frac{8\pi^2 \sin^2\theta}{\lambda^2} U^2\right) \cdot F_H^0 \quad (7.4)$$

where F_H^0 is the structure factor for undamaged crystal, θ is Bragg angle, and λ is X-ray wavelength.

Undamaged structure factor F_H^0 has been calculated as described in previous chapter 5. After knowing strain and damage of each lamella, structure factor F_H is calculated. Then applying the Takagi-Taupin derivation as discussed in chapter 5 rocking curves are simulated.

Finally the rocking curves are obtained after convoluting with a Gaussian function

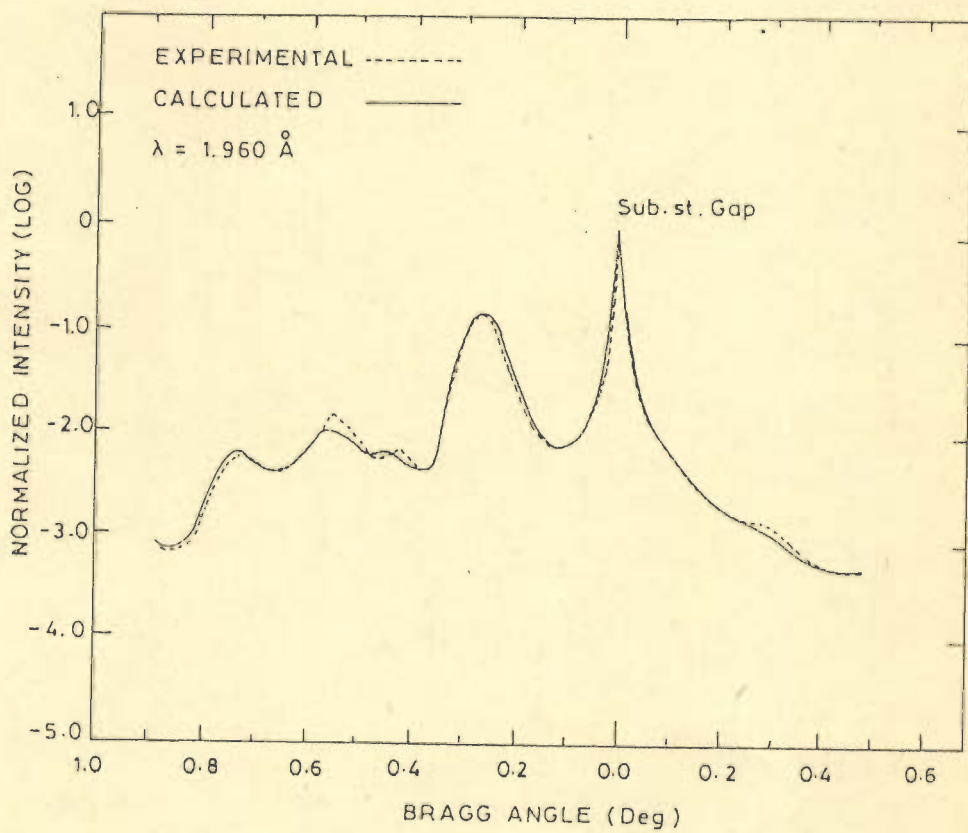


FIG. 7.1 COMPARISON OF EXPERIMENTAL AND CALCULATED ROCKING CURVES

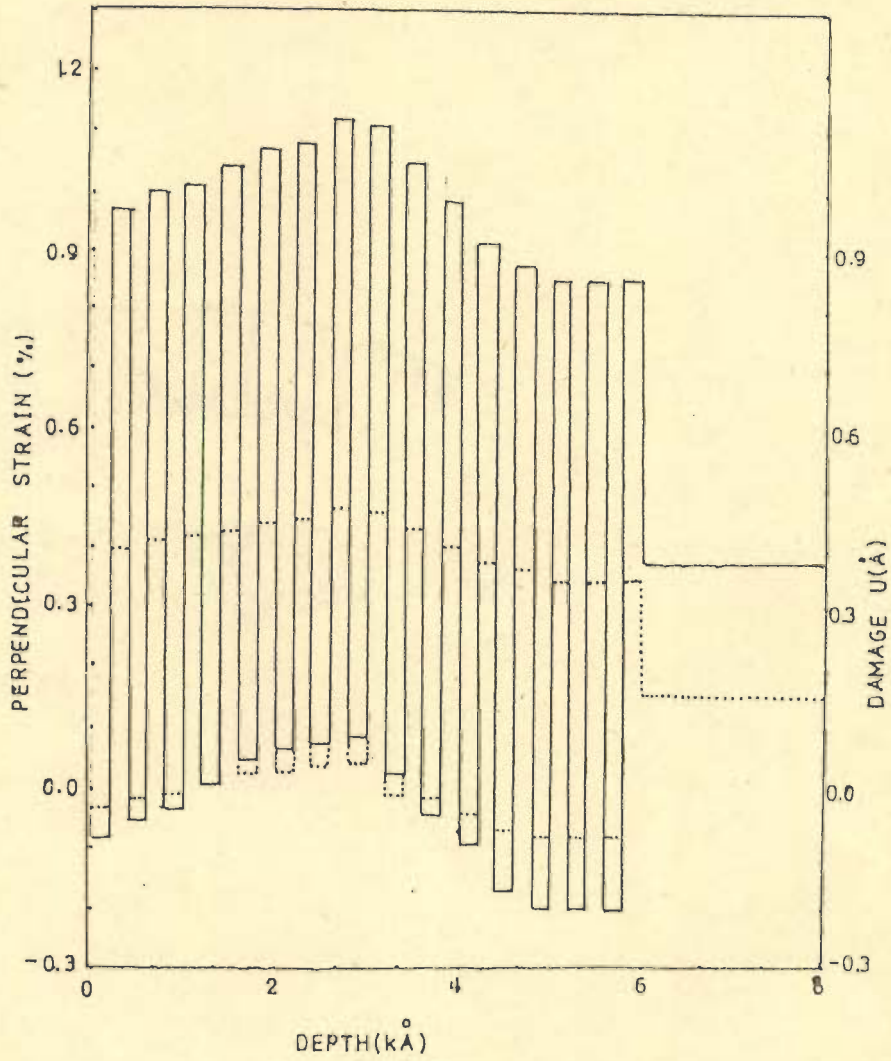


FIG. 7.2

$$|x(i)|^2 = \frac{\int |x(\theta)|^2 g(\theta) d\theta}{\int g(\theta) d\theta} \quad (7.5)$$

where $g(\theta) \approx e^{-\theta^2/\Delta^2}$

The half width of the Gaussian convolution was 12 arc sec.

This model has been used for the interpretation of X-ray rocking curve including damage and strain depth distribution for an ionimplanted superlattice reported by Myers et al [91]. In the simulation the close fit to experimental rocking curve achieved by taking $U = 0.392\epsilon$. Comparison of experimental and simulated rocking curve is shown in Figure 7.1. Strain/damage versus depth distribution profile obtained as shown in Figure 7.2.

7.4 X-RAY ROCKING CURVE ANALYSIS

The data available for the Be implanted GaAsP/GaP SLS structure have been used to calculate theoretical rocking curve. First a possible strain distribution is assumed by considering the previously mentioned general behaviour of the experimental rocking curve and the projected range [142]. Then calculated and experimental curves are compared, any deviation from the experimental curve is used to modify

the assumed strain distribution. This procedure is repeated until a good agreement between theoretical and experimental is obtained. The final strain/damage depth distribution is shown in Figure 7.2. The strain varies from +0.85% in the GaAsP to -0.20% in the GaP layers of the SLS. The GaP layer must be compressed along the growth direction thereby accounting for negative sign for the absolute strain.

The general behaviour of rocking curves:

- (1) Total angular width of diffraction profile is related to the maximum strain.
- (2) The height of the envelope of the lower peaks is related to the strain gradient with respect to the depth.
- (3) The period of neighbouring peaks become smaller for a thicker ion-implanted layer.

For this implant, the best fit to the experimental rocking curve data did not require interdiffusion, calculation. This reflect a remarkable interfacial stability in the presence of extensive point defect production by the implanted ions. Also strain distribution in the buffer layer and unimplanted region of the SLS was not altered by the implant damage.

7.5 CONCLUSION

Dynamical model is more accurate than kinematical model, but for thin crystals both model show similar results [133]. In the present GaAsP/GaP Be implanted SLS best fit to experimental rocking curve is obtained, when maximum strain and the maximum damage occur at the same depth as could be seen in the Figure 7.2. This also proved that damage is linear with strain. In the present example $U = 0.392\varepsilon$ is obtained by simulation. No interdiffusion has been observed. As shown in Figure 7.1, the peaks are noticeably broadened due to the non-uniform depth distribution of strain introduced by the implant damage.

CHAPTER 8
DYNAMICAL SIMULATION USING
ABELES MATRIX METHOD

8.1 INTRODUCTION

Another new dynamical simulation technique involving a 2×2 matrix solution of Maxwell's equations has been developed in the present chapter. Variation of the refractive index along the growth direction (100) has been considered in the calculations.

A number of rocking curves are generated using this technique for various compositions, and number of periods for symmetric (400) reflections. Experimental rocking curves of InGaAs/GaAs and InGaAs/InP superlattices available in the literature [15,66,114] have been simulated. A comparison between the Takagi-Taupin and this Abeles-Takagi technique showed that the Abeles-Takagi model gives more sharp peaks, and needs less computation time compared to Takagi-Taupin model. From this comparison new conclusions are reached, in the present work concerning the superlattice peak broadening.

A change in characteristic matrix element calculation relating to the phase thickness have been incorporated and with this assumption, an experimental three crystal X-ray scan of InGaAs/InP superlattice have been analyzed. The results of this analysis is then compared with the kinematical step model reported in the literature [146].

8.2 ABELES MATRIX METHOD

Abeles' 2x2 matrix method is commonly applied to optics for the visible part of electromagnetic spectrum [6,9]. This method can also be applied to compute the reflectivity of a multilayer structure for X-rays, if variation of X-ray refractive index normal to any set of Bragg planes of interest is known [92]. This variation can be obtained from the complex X-ray structure factor, the real part of which is largely a measure of a Fourier component of electron density in a direction normal to the Bragg planes. The imaginary part is a measure of local average linear absorption coefficient.

Since the refractive index for X-rays within a crystal varies by a very small amount, a highly accurate closed-form solution for the matrix relating the electromagnetic field vectors on opposite sides of one cycle of the periodic structure can be obtained from a Fourier analysis of the complex refractive index or the structure factors [68].

If variation of optical parameters of a layered medium in the x and y directions can be neglected, field components of plane waves that are incident in the x-z plane must be of the form

$$f_j = \psi_j(z) \exp[i(kx - \omega t)] \quad (8.1)$$

The complex refractive index n at frequency ω is everywhere isotropic, and if the magnetic susceptibility is negligible, Maxwell's equation reduce to the form

$$\frac{\partial}{\partial z} \begin{bmatrix} E_x \\ H_y \end{bmatrix} = i \frac{\omega}{c} \begin{bmatrix} 0 & 1 - (1/n^2)(kc/\omega)^2 \\ n^2 & 0 \end{bmatrix} \begin{bmatrix} E_x \\ H_y \end{bmatrix} \quad (8.2(a))$$

and

$$\frac{\partial}{\partial z} \begin{bmatrix} E_y \\ -H_x \end{bmatrix} = i \frac{\omega}{c} \begin{bmatrix} 0 & 1 \\ n^2 - (kc/\omega)^2 & 0 \end{bmatrix} \begin{bmatrix} E_y \\ -H_x \end{bmatrix} \quad (8.2(b))$$

where E_i and H_j are electric and magnetic field components, and kc/ω is $\cos\theta_b$, where θ_b is the angle between the wave normal in vacuum and the layer surfaces.

Both the equations (8.2a,b) can be written

$$\frac{\partial}{\partial z} \begin{bmatrix} \psi_1 \\ \psi_2 \end{bmatrix} = i \frac{\omega}{c} \begin{bmatrix} 0 & a^2 \\ b^2 & 0 \end{bmatrix} \begin{bmatrix} \psi_1 \\ \psi_2 \end{bmatrix}$$

Or,

$$\frac{\partial}{\partial z} \bar{\psi} = i \frac{\omega}{c} [D] \bar{\psi} \quad (8.3)$$

If n varies with z then $[D]$ will be a function of z . If n is independent of z , then the new equation for a finite slab of thickness h is-

$$\begin{bmatrix} \psi_1 \\ \psi_2 \end{bmatrix}_{z+h} = \begin{bmatrix} \cos qh & i(a/b)\sin qh \\ i(b/a)\sin qh & \cos qh \end{bmatrix} \begin{bmatrix} \psi_1 \\ \psi_2 \end{bmatrix}_z \quad (8.4)$$

where $q = ab\omega/c$

Or,

$$\vec{\psi}(z+h) = [M]\vec{\psi}(z) \quad (8.5)$$

q is same for π and σ polarized radiation.

To find the matrix $[M]$ across a medium of varying refractive index, matrices of short intervals across which the variation is negligible may be multiplied together.

$$[M] = \prod_{j=1}^N [M(n_j, h_j)] \quad (8.6)$$

8.3 REFRACTIVE INDEX n FOR X-RAYS

The refractive index n_r for X-rays is a complex number whose imaginary part n_i is small and positive and whose real part n_r usually differs from unity by a small negative amount. At X-ray wavelengths shorter than and not too near the characteristic absorption wavelengths of atoms in the medium, the average value of the real and imaginary part of n is [9]

$$\bar{n}_r = 1 - \lambda^2 r_e \bar{\rho}_e / 2\pi; \quad \bar{n}_i = \mu_e \lambda / 4\pi \quad (8.7)$$

where r_e classical electron radius, $\bar{\rho}_e$ is the average number

of electrons per unit in the medium and μ_e linear absorption coefficient. If the electron density is Fourier analyzed in a direction normal to the surfaces then

$$n(z) = 1 - \frac{\lambda^2 r_e}{2\pi a^3} [F_0 + 2\sum_h (F_{ch} \cos \frac{2h\pi z}{a} + F_{sh} \sin \frac{2h\pi z}{a})] \quad (8.8)$$

where a is lattice, parameter, λ is X-ray wavelength, and $r_e = 2.818 \times 10^{-15} \text{Å}$. Since much of the X-ray absorption in a crystal occurs near atomic nuclei, the imaginary part also has Fourier components. These can be incorporated into the structure factor components by making F_{ch} and F_{sh} complex as has been used in the above equation 8.8. For zinc-blende lattice the Fourier coefficients are related to the complex conjugates of the usual X-ray structure factors F_{h00} (where h is the index along the growth direction), which pertain to an exponential Fourier expansion over the electron density [61,92], by

$$\begin{aligned} F_0 &= F_{000}^* \\ F_{ch} &= F_{\bar{h}00}^* + F_{h00}^* = 2F_{h00}^* \\ F_{sh} &= i(F_{h00}^* - F_{\bar{h}00}^*) = 0 \end{aligned} \quad (8.9)$$

No sine term appears because the zinc-blende lattice has inversion symmetry along the growth direction (100). The asterisks indicate complex conjugates.

8.4 ABELES-TAKAGI MODEL

In this model the superlattice substrate reflectivity is obtained from the Takagi-Taupin's derivation as described in chapter 5 using the equation (5.9)

$$x_0 = \frac{-B + (B^2 - A^2)^{\frac{1}{2}} \text{Sgn}(\text{Im}(s))}{A} \quad (8.10)$$

The Abele's matrix approach is then applied to calculate reflectivities of the superlattice periods.

In Abele's method the unit cell is subdivided into sublayers, each having a constant index of refraction but with a variation from sublayer to sublayer according to equation (8.8) for (400) reflection

$$n(z) = 1 - \frac{\lambda^2 r_e}{2\pi a^3} [F_0 + 2F_H \cos(\frac{8\pi z}{a})] \quad (8.11)$$

This variation of $n(z)$ along the growth direction can be formulated in a 2x2 matrix form Maxwell's differential equations (8.2), which can be integrated for an epilayer having a uniform index of refraction. A matrix is thereby obtained which produces the field present at the bottom of layer when it operates on a vector comprised of the field at the top.

$$\begin{bmatrix} \psi_1 \\ \psi_2 \end{bmatrix}_{\text{Top}} = \begin{bmatrix} M \end{bmatrix} \cdot \begin{bmatrix} \psi_1 \\ \psi_2 \end{bmatrix}_{\text{Bottom}} \quad (8.12)$$

A superlattice period usually consists of a succession of homogeneous layers of alternately different refractive indices n_1 and n_2 and thickness t_1 and t_2 . Assuming medium to be non-magnetic and setting [10,53] equation

$$\beta_i = \frac{2\pi}{\lambda} n_i t_i \cos\theta_i; \quad i=1,2,3,\dots,N \quad (8.13)$$

The characteristic matrix for a superlattice is given by

$$[M]_i = \begin{bmatrix} \cos\beta_i & j\frac{1}{n_i} \sin\beta_i \\ jn_i \sin\beta_i & \cos\beta_i \end{bmatrix} \quad (8.14)$$

For complete N periods of the SLS structure the characteristic matrix $[M]$ of individual period is multiplied N times.

$$[M]^N = \prod_{i=1}^N [M]_i$$

The reflectivity then obtained as

$$R = \left| \frac{M_{11}^N + M_{12}^N - M_{21}^N - M_{22}^N}{M_{11}^N + M_{12}^N + M_{21}^N + M_{22}^N} \right|^2 X_o \quad (8.15)$$

The reflectivity so obtained is convoluted according to Zachariassen's equation (3.216) [152].

Rocking curves are generated for various $\text{In}_x\text{Ga}_{1-x}\text{As}/\text{GaAs}$ and $\text{In}_x\text{Ga}_{1-x}\text{As}/\text{InP}$ superlattices, where the effect of a change in composition x and thicknesses of the well L_W and of the

barrier L_B have been studied. Figures 8.1 to 8.6 show the rocking curves generated. The following salient points are noted.

- (1) Abeles'-Takagi approach gives much narrower peaks than the Takagu-Taupin's approach.
- (2) Computation time for this technique is nearly half of that of Takagi-Taupin's model.
- (3) Figure 8.1 and 8.2 where the change in composition show the change in peak position and peak height.
- (4) Profiles obtained by changing barrier and well widths are shown in Figures 8.3 to 8.6. It is clearly seen that a small variation in well or barrier width changes the profile, satellite peaks vary in amplitude and position both.

8.5 COMPARISON OF EXPERIMENTAL AND SIMULATED ROCKING CURVES

Experimental rocking curves of InGaAs/GaAs and InGaAs/InP superlattice structures reported in the literature [15, 66] are analyzed using this new model as shown in Figure 8.7 and 8.8. The intensities of various order satellite peaks for InGaAs/GaAs SLS are compared in Table 8.1.

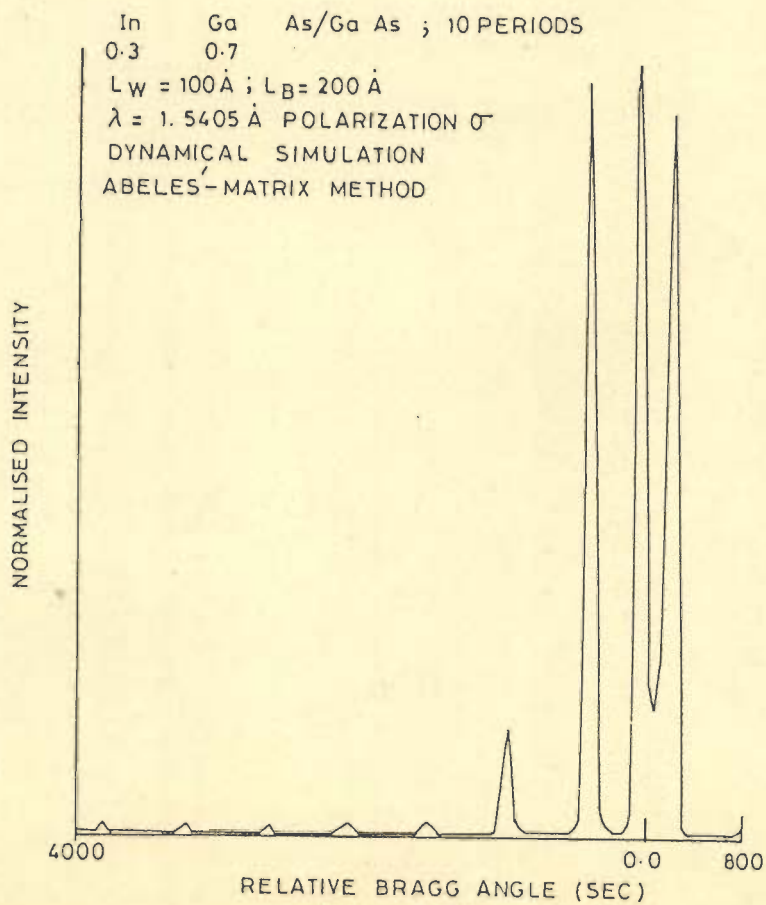
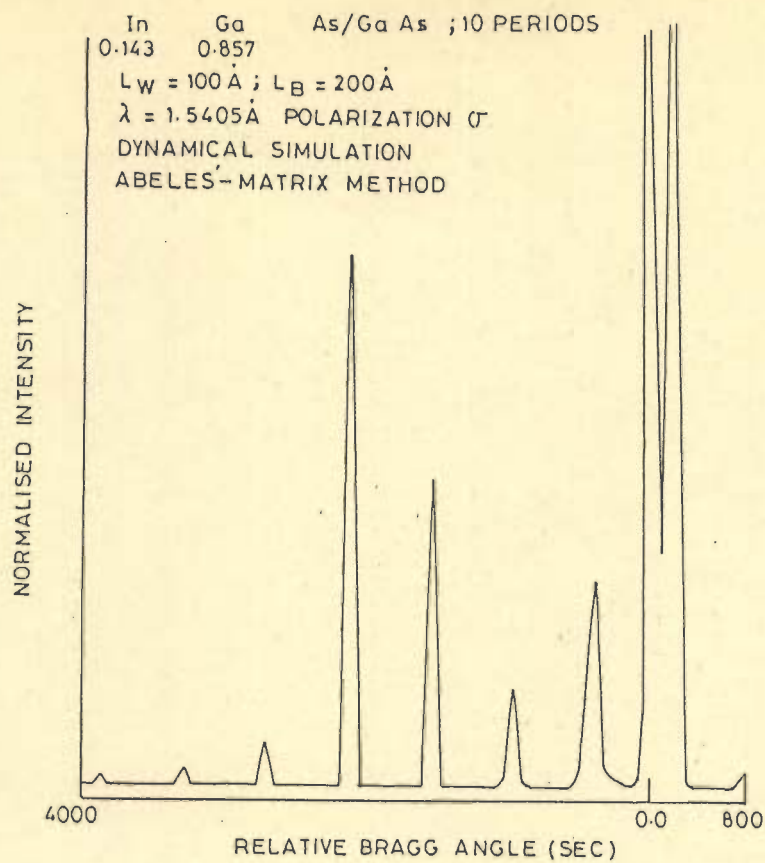


FIG. 8.1 & 8.2

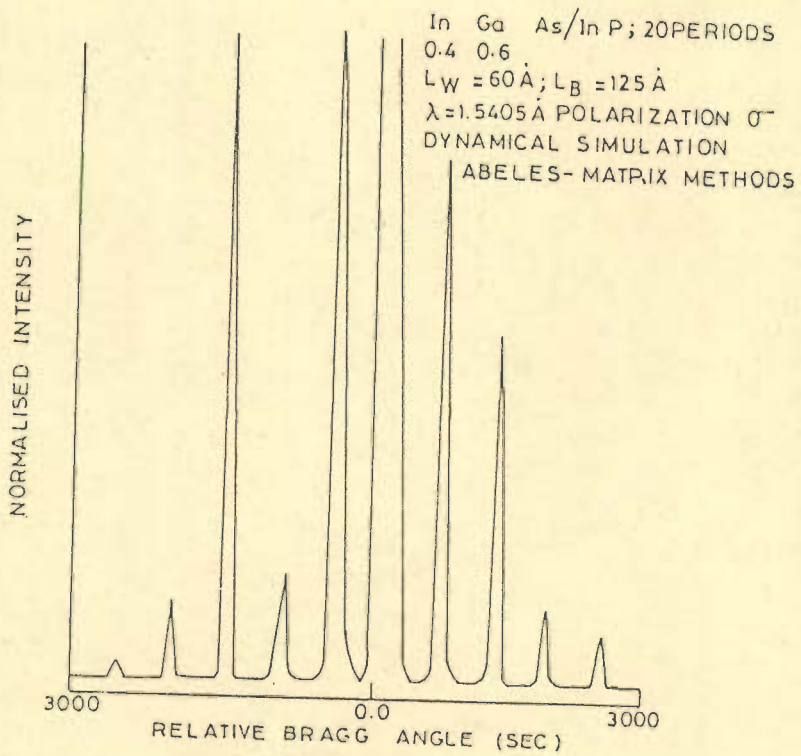
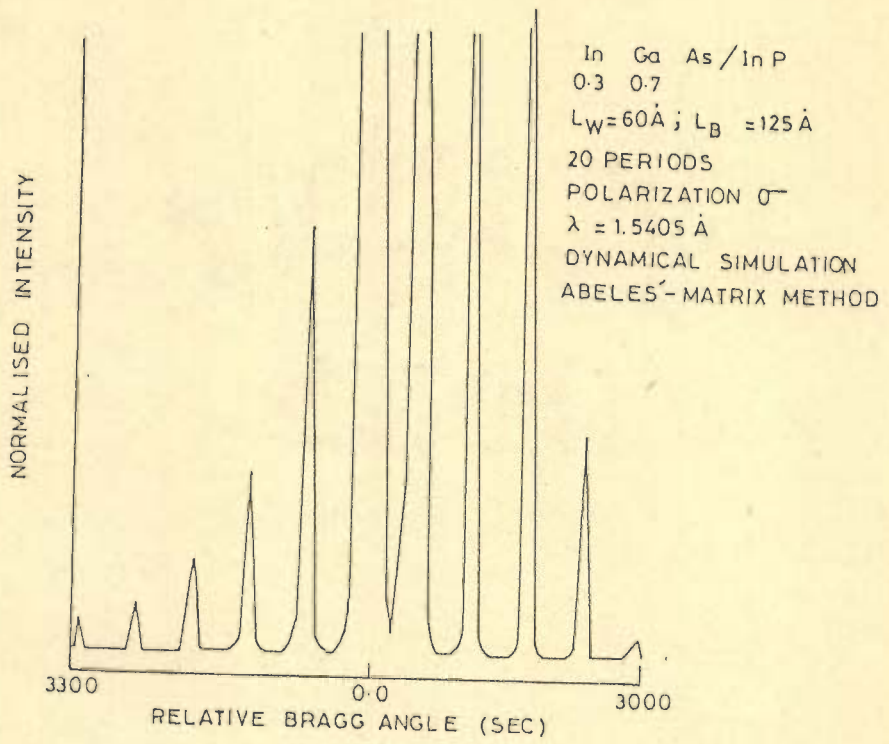


FIG. 8.3 & 8.4

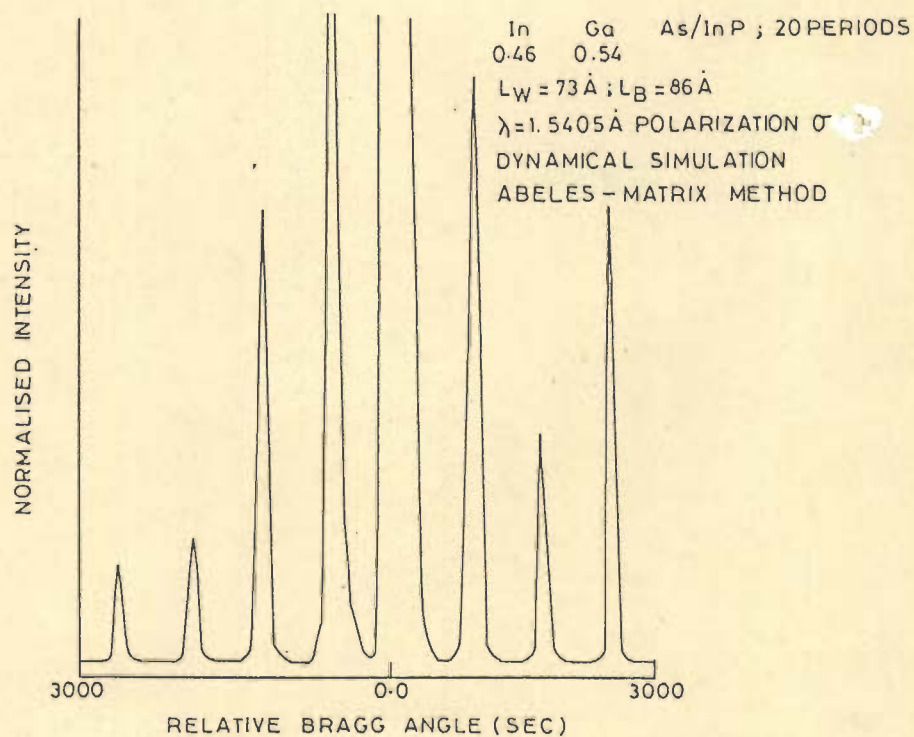
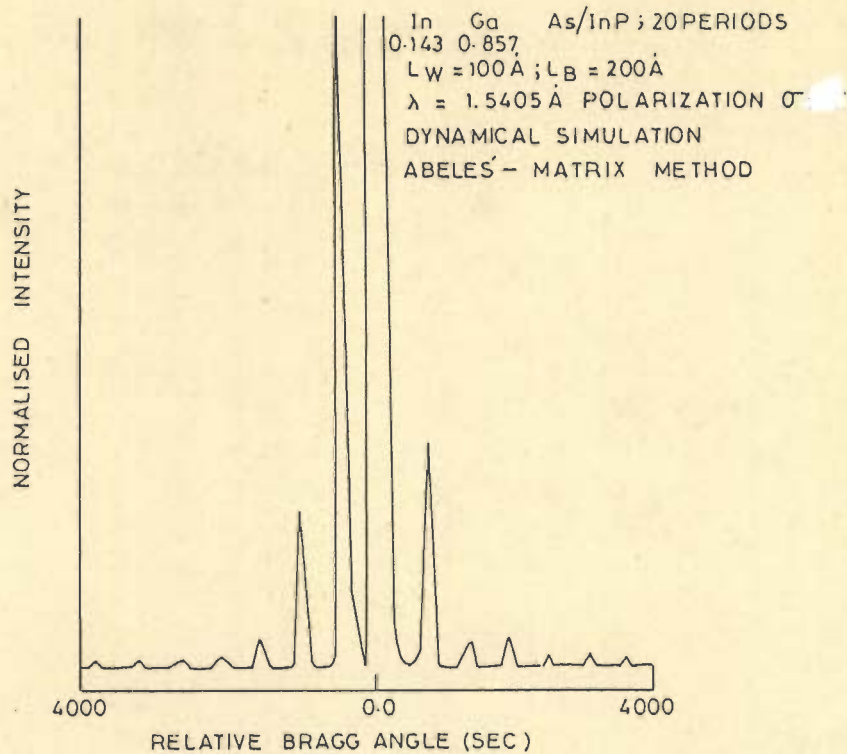


FIG. 8.5 & 6.6

InGaAs/GaAs SLS:

Figure 8.7 shows experimental (solid line), simulated (dotted line) Takagi-Taupin method, and Abeles-Takagi method (dashed line) comparison [134]. In the experimental curve in addition to the substrate peak other seven superlattice peaks are clearly visible. Their spacing yield an average superlattice period thickness 600\AA . The location of zero order peak is same in both the simulation methods but the amplitude in case of Abeles-Takagi method is higher. Figure 8.7 also shows that the zero order peak is less intense in experimental as well as in simulated curves compared to other higher order peaks this is due to the combination of large strain modulation and large thickness of the period. Sometimes this situation presents the practical problem of identifying the zero-order peak, than Abeles-Takagi model is of help to identify the zero order peak.

InGaAs/InP superlattice:

This superlattice has been analyzed using both the methods. Figure 8.8 shows the comparison of experimental and simulated curves. The presence of higher order peaks confirms the composition modulation. A large zero order peak present due to less strain and thickness modulation. Positive higher order peaks are less intense in the experimental curve but in the simulated curves they are clearly

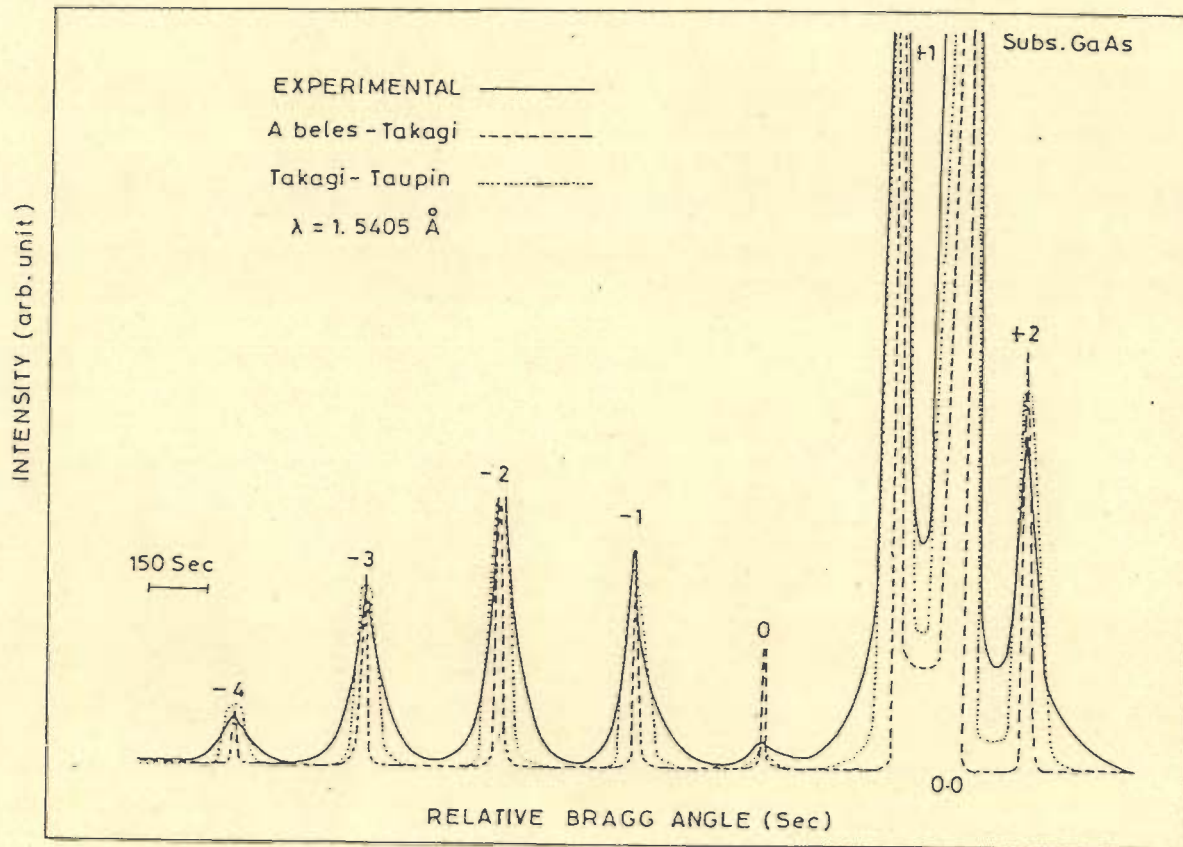


FIG. 8.7 COMPARISON OF EXPERIMENTAL AND CALCULATED ROCKING CURVES

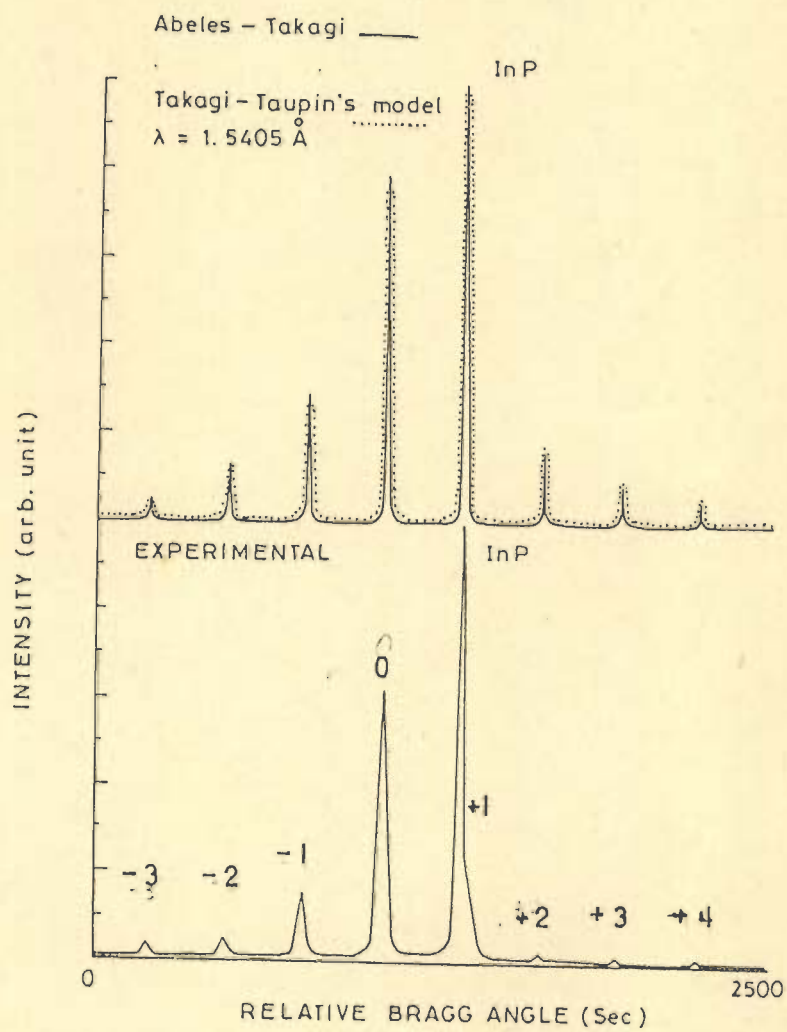


FIG. 8.8 COMPARISON OF EXPERIMENTAL AND CALCULATED ROCKING CURVES

Table 8.1 : Comparison between relative diffraction intensity of each satellite peak

Structural details	Satellite order	Experimentally measured intensity [66]	Kinematically calculated intensity [66]	Dynamically calculated intensity	
				Takagi-Taupins method [129]	Abeles'-Takagi method [134]
$\text{In}_x\text{Ga}_{1-x}\text{As}$	+2	0.26	0.416	0.402	0.471
x=0.143	+1	1.0	1.0	1.0	1.0
	0	0.02	0.02	0.020	0.131
100Å well	-1	0.25	0.206	0.223	0.236
200 Å barrier	-2	0.29	0.301	0.299	0.294
10 periods	-3	0.18	0.227	0.199	0.212
	-4	0.08	0.107	0.093	0.088

Table 8.2

Comparison of InGaAs/InP Superlattice Satellite Peaks

Sample	Sate- llite ord- ers	Experimentally measured intensity	Takagi-Taupin's model calcula- ted	Abele's-Takagi model calcula- ted
$\text{In}_x\text{Ga}_{1-x}\text{As}$ InP	+4	0.011	0.023	0.025
$L_W=100\text{\AA}$	+3	0.015	0.026	0.026
$L_B=500\text{\AA}$	+2	0.018	0.069	0.061
$x=0.495$	+1	1.0	1.0	1.0
Number of periods	0	0.601	0.632	0.635
=32	-1	0.063	0.071	0.071
	-2	0.035	0.039	0.039
	-3	0.021	0.021	0.021

visible. Satellite peak comparison has been presented in Table 8.2.

8.6 THREE CRYSTAL X-RAY SCAN SIMULATION

The three crystal X-ray patterns have been analyzed by computer simulation using kinematical step model [146]. In this section the Abeles-Takagi approach have been used to simulate a three crystal X-ray scan of InGaAs/InP superlattice [135] structure reported in the literature [146]. A comparison is made between step model and Abeles-Takagi model results. Table 8.3 compares the results obtained from these two models.

To simulate three crystal X-ray scan, equation (8.13) and (8.14) have been used. The phase condition β_i is expressed as

$$\beta_i = 2k_0 n_i t_i \sin\theta_i + \phi_1 + \phi_2 = 2n\pi \quad (8.16)$$

where ϕ_1 and ϕ_2 are the phase shifts at the interfaces between InGaAs and InP and between InP and InGaAs respectively. Assuming the phase shift inside each cladding layer in the direction perpendicular to the surface of the substrate is $\pi/2$ [67]. Using this assumption and getting another value of β_i as $0.5\beta_i$, and numerically calculation equations (5.9), (8.13) and (8.14) for substrate and epilayer reflectivity respectively. The final reflectivity is obtained from equation (8.15).

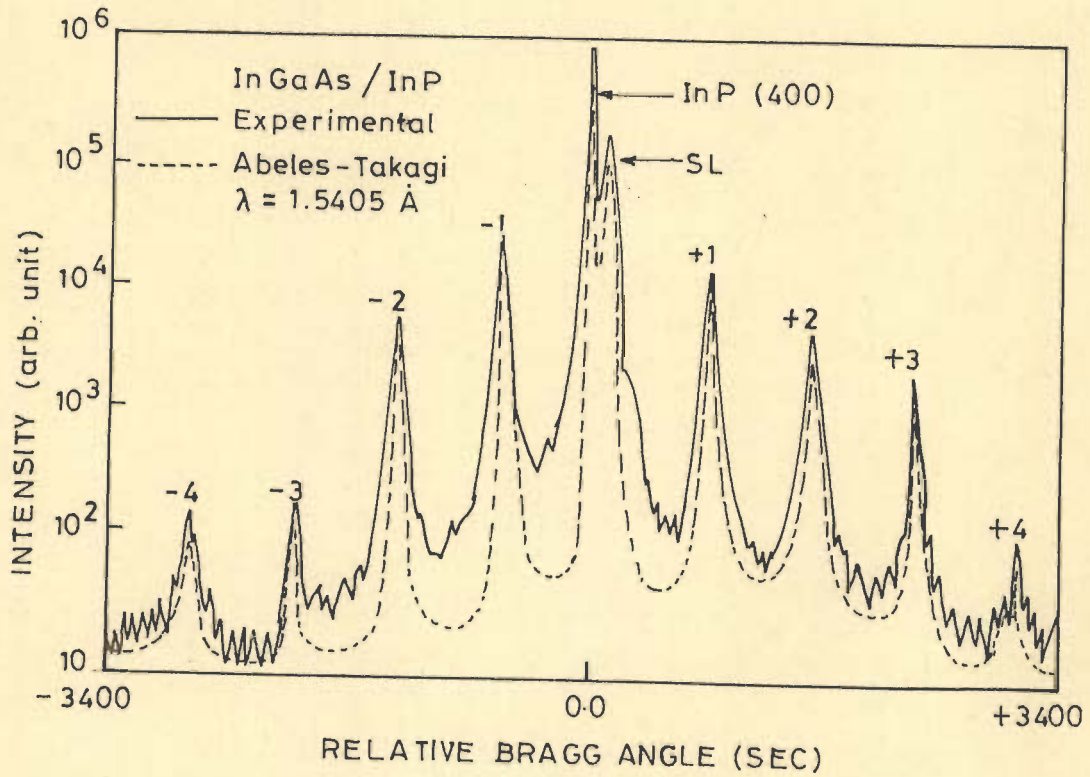


FIG. 8.9 COMPARISON OF EXPERIMENTAL AND SIMULATED 3-CRYSTAL X-RAY SCAN

Table 8.3 : Structural details of InGaAs/InP superlattice structure obtained from simulation

Kinematical step model [146]		Abeles'-Takagi dynamical model [135]
No. of periods	20	20
No. of Molecular layers of well	19	19
No. of molecular layers of Barrier	32	33
Composition x in $\text{In}_x\text{Ga}_{1-x}\text{As}$	0.47	0.467

This intrinsic reflectivity obtained for the superlattice structure is similar to three crystal X-ray scan. A close fit has been obtained from the available growth data.

Figure 8.8 shows a comparison made between experimental three crystal X-ray scan and simulated scan of InGaAs/InP superlattice. In the Figure 8.9 the +3 order satellite intensity is much stronger than -3 order peak, kinematical step model also shows the same result. From this technique satellite peak shape obtained is more close to the shape of experimental peak. The presence of stronger higher-order peak in the simulated profile show the abruptness of the interfaces.

8.7 CONCLUSION

The effect of composition variation has been observed to change the satellite peak position and thier amplitude in the same way as has been observed in kinematical and Takagi-Taupin dynamical models. For a small variation in thickness of well and barrier, the present model is found to be more sensitive, than kinematical and Takagi-Taupin dynamical models.

The experimental rocking curve for InGaAs/GaAs SLS simulated by all the three models show the same

angular position, for same growth parameters. Experimental curve has wider satellite peaks. This peak broadening is due to mosaic structure formed by the misfit dislocations. The epilayer thickness sensitivity of the model has been used to simulate three crystal X-ray scan of the superlattice structure.

CHAPTER 9
GENERAL DISCUSSION AND CONCLUSION

There is a strong motivation to develop InGaAsP/InP material systems because of their potential application as sources for transmission through low loss optical fibres. Significant advances have been made in recent years in the development of strained layer materials and devices. Strained-layer InGaAs-GaAs lasers have been fabricated using molecular beam epitaxy (MBE) and metalorganic chemical vapour deposition (MOCVD) reported in the literature. These lasers have threshold current and photoexcitation power densities comparable to lattice-matched structures. Recently it has been demonstrated by Camaras et al that strained-layer superlattices can be grown almost free of defects at heterointerfaces to make possible stimulated emission. Further tests indicate that strained layers with a longer life may be possible.

In the present thesis the quantum-wells and strained-layer superlattices grown by MBE and MOCVD have been studied. It has also been found necessary to have a knowledge of growth process for the characterization of InGaAsP systems superlattices. Numerous presently available methods of characterization like PL, TEM, AES, RBS, X-ray diffraction etc. have been reviewed. X-ray diffraction is a nondestructive and is capable of measuring strain from 10^{-8} upwards. However, the experimental X-ray diffraction method can not reveal the details of individual layers inside a superlattice. The present thesis discusses kinematical and

dynamical simulation techniques, which are developed to simulate experimental rocking curves using a computer program. The techniques are nondestructive and can provide more accurate inside details superlattice structures.

For the detailed study a number of rocking curves have been simulated using a kinematical model. A variation in the composition x for $\text{In}_x\text{Ga}_{1-x}\text{As}/\text{GaAs}$ SLS results in a change in the satellite peaks position and amplitude, while a variation in the number of periods and epilayer thicknesses changes the peak amplitude with peak position remaining the same. By fitting experimental curves using the kinematical model details of the actual structure have been obtained. However, kinematical model has its own limitations. In a particular example $\text{InGaAs}/\text{GaAs}$ SLS with period thickness 300\AA , by increasing the number of periods beyond 10 same rocking curve is observed. Also the substrate peak is missing.

Therefore a dynamical model has been developed incorporating the extinction effect. The rocking curves generated with this model however, takes more computation (CPU) time. For different composition x the rocking curves generated show variation in satellite peaks position and their amplitudes. In this simulation substrate peak is clearly visible, and beyond 10 periods upto 150 periods, satellite peaks with varying amplitudes exists.

A number of experimental rocking curves are simulated and a close fit achieved. An experimental rocking curve of InGaAs/GaAs SLS reported in the literature has been simulated by both the techniques. The simulations show that the dynamical results are more accurate and close to experimental. A close fit of InGaAs/InP superlattice rocking curve shows that this simulation technique can identify the carryover of As into the InP barriers and the concentration and distribution of As are easy to determine.

Further more the effects of thermal annealing Zn diffusion, and ionimplantation processes on the superlattices have been studied using this computer simulation technique. In a thermally annealed InGaAs/GaAs SLS experiment performed by Joncour et al rocking curves for different annealing time 15,24,39,55,72 hours at 850°C have been obtained. In the present studies, the dynamical model has been modified and rocking curves for these thermally annealed SLS are simulated by assuming a suitable In-Ga interdiffusion coefficient D . Finally a value of D for each annealing time has been obtained after achieving a close fit to experimental curves, these values are then compared with those obtained from kinematical simulations. Comparison show both the results are nearly same, the slight variation may be due to the thin superlattice structure.

The same model when applied to Zn diffused InGaAs/GaAs SLS rocking curve simulation, D obtained after achieving a close fit to the experimental results of Laidig et al, have proved that Zn diffusion enhances the interdiffusion or intermixing 10 to 20 times that of thermally annealed SLS. The diffusion depth profiles have also been obtained. Interdiffusion coefficient D for In-Ga obtained from, direct experimental rocking curves measurement using Chan's modified model, have been compared with those obtained from the simulation techniques, were found close. Disordering or intermixing of superlattice periods due to thermal annealing and Zn diffusion also have been studied.

Beryllium implanted GaAsP/GaP SLS rocking curve reported by Myers et al has been simulated using modified dynamical model, and characterized in this thesis. The present dynamical model gives similar results as reported by Myers et al using kinematical theory. Match to the experimental rocking curve provides damage and strain depth distribution within the implanted layers. The linear expansion of the layers due to point defect generation for the 1×10^{15} Be/cm² implant is determined to be 0.29%. The Beryllium implantation effects observed in the present simulation studies, directly reflect the stability of GaAsP/GaP SLS, this is because no interdiffusion or intermixing of superlattice periods have been included in the simulation.

A new technique of dynamical simulation based on Abeles' matrix method has been used to generate rocking curves. Significant results obtained in this simulation studies, are sharp satellite peaks and less computation time compared to Takagi-Taupin model. Experimental rocking curves reported in the literature are simulated and perfect match to experimental results have been obtained. In this simulation it was found that intensity of the satellite peaks and their relative positions are very much sensitive to epilayer thickness of the superlattice period. Even $\pm 1\text{\AA}$ changes the rocking curve reasonably. Therefore as far as the superlattice period thickness is concerned this method found to be more accurate in predicting well and barrier thicknesses.

This technique have also been successfully applied to three crystal X-ray scan simulation. Looking to the satellite peak amplitude and effect of slight well or barrier thickness variation sensitivity. A little change in phase thickness due to interfaces has been incorporated in the characteristic matrix element calculations, which results in a close fit to the experimental three crystal X-ray scan. The results obtained from this new technique have been compared with those obtained from kinematical step model. Significant differences have been observed, the satellite peaks are of similar nature as in the experimental results.

REFERENCES

1. Arnold, G.W., Picraus, S.T., Peercy, P.S., Myers, D.R., and Dawson, L.R., "Structural integrity of ion-implanted $\text{In}_{0.2}\text{Ga}_{0.8}\text{As}/\text{GaAs}$ strained-layer superlattice", *Appl. Phys. Lett.*, Vol. 45, pp 382-384, Aug. 1984.
2. Auvray, P., Baudet, M., and Regreny, A., "X-ray diffraction study of intentionally disordered GaAlAs-GaAs superlattices", *J. Appl. Phys.*, Vol. 62, pp. 456-460, July 1987.
3. Anderson, K.A., Donelley, J.P., Wang, C.A., Woodhouse, J.D., and Hans, H.A., "Compositional disordering of GaAsAlGaAs multiple quantumwells using ion-bombardment at elevated temperatures", *Appl. Phys. Lett.* Vol. 53, p 1632-1634, 1988.
4. Amelinckx, S., Gevers, R., and Van Landuyt, I., "Diffraction and imaging techniques in Material science", North-Holland Pub. Col. Amsterdam 1970.
5. Ashkin, M., and Kuriyama, M., "Quantum theory of X-ray diffraction by a crystal", *Jpn. Phy. Soc.*, Vol 21, pp. 1549-1558, 1966.
6. Abeles, F., *Ann. de Physique*, Vol. 5, pp. 596-640, 1950.
7. Ashkin, A., and Gershenzon, M., "Reflection and guiding of light at p-n junction", *J. Appl. Phys.*, Vol. 34, pp. 2116-2119, 1963.

8. Bulman, G.E., Myers, D.R., Zipperian, T.E., Dawson, R.L., Wiczer, J.J. "Photocurrent multiplication in ionimplanted lateral InGaAs/GaAs strained layer superlattice photo-detectors", *Appl. Phys. Lett.* Vol. 47, pp. 733-735, 1985.
9. Bereman, D.W., "Dynamical theory of X-ray diffraction in flat, focussing and distorted crystals by Abeles' matrix method", *Phy. Rev. B.* Vol. 14, pp. 4313-4317, Nov. 1976.
10. Born, M. and Wolf, E., *Principles of Optics*, 6th ed. Pergo-man, New York, 1980.
11. Bour, D.P., Shealy, J.R., and Mckernan, S., "GaInP/GaAs inter-faces by organometallic vapor-phase epitaxy", *J. Appl. Phys.*, Vol. 63, pp. 1241-1243, Feb. 1988.
12. Burgeat, P.J. and Taupin, D., "Application de la Theorie... Cristaux de Silicium", *Acta. Cryst.* A24, pp. 99-102, 1968.
13. Batterman, B.W., and Cole, H., "Dynamical diffraction of X-rays by perfect crystals", *Rev. of Mod. Phys.*, Vol. 36, pp. 681-717, 1964.
14. Bruson, A., Piecuch, M., and Marchal, G., "Interdiffusion and chemical ordering in composition modulated FeSi/Si amorphous films", *J. Appl. Phys.*, Vol. 58, pp. 1229-1233, 1985.

15. Barnett,S.J., Brown,G.T., Courtney,S.J., Brass,S.J., and Taylor,L.L., "A study of layer composition fo InGaAs/ InP multiple-quantum wells grown by MOCVD using double-crystal X-ray diffraction theory and experiment", J. Appl. Phys., Vol. 64, pp. 1185-1191, 1988.
16. Bedair,S.M., Katsuyama,T., Timmons,M., and Tischler,M.A., "A new GaAsP-InGaAs strained layer superlattice light emitting diode", IEEE Elect. devi. Lett., Vol EDL-5, pp. 45-47, 1984.
17. Chapman,L.D., Colella,R., and Bray,R., "X-ray diffraction studies of acoustoelectrically amplified phonons", Phy. Rev. B., Vol. 27, pp. 2264-2277, 1981.
18. Camras,M.D., Holonyak,N.Jr., Burnham,R.D., Streifer,W., Scrifres,D.R., Paoli, T.L., and Lindstrom,C., "Wavelength modification of AlGaAs quantum-well heterostructure lasers by layer interdiffusion", J. Appl. Phys., Vol 54, pp. 5637-5641, Oct. 1983.
19. Cook,H.E., and Hilliard,J.E., "Effect of Gradient Energy on Diffusion in Gold-Silver Alloys", J. Appl. Phys. Vol. 40, pp. 2191-2205, Apr. 1969.
20. Cromer,D.T., and Liberman,D., "Relativistic calculation of Anomalous scattering factors for X-rays", The J. Chem. Phys. Vol. 53, pp. 1891-1898, 1970.

21. Camras, M.D., Brown, J.M., Holonyak, N.Jr., Nixon, M.A., and Kaliski, R.W., "Stimulated emission in strained-layer quantum-well heterostructures", J. Appl. Phys., Vol. 54, pp. 6183-6189, Nov. 1983.
22. Cole, H., and Stemple, N.R., "Effect of crystal perfection and Polarity on Absorption Edges seen in Bragg Diffraction", J. Appl. Phys., Vol. 33, pp. 2227-2233, 1962.
23. Chu, X., and Tanner, B.K., "Double crystal X-ray rocking curves of multiple layer structures", Semocond. Sci. Technol., Vol. 2, pp. 765-771, 1987.
24. Clements, B.M., and Gay, J.G., "Effect of layer thickness fluctuations on superlattice diffraction", Phys. Rev. B, Vol. 35, pp. 9337-9340, June 1987.
25. Chang, L.L., "A review of recent advances in semiconductor superlattices", J. Vac. Sci. Technol. B1(2), pp. 120-125, Apr. 1983.
26. Crank, J., "The Mathematics of Diffusion", (London:OUP), 1956.
27. Cullity, B.D., "Elements of X-ray diffraction", Addison-Wesley, Pub. Co. Inc. USA, 1978.
28. Dobisz, E.A., Tell, B., Craighead, H.G., and Tamargo, M.C., "Disordering of AlAs-GaAs superlattices by Si and S implantation at different implant temperatures", J. Appl.

- Phys., Vol. 60, pp. 4150-4153, Dec. 1986.
29. Deppe, D.G., and Holonyak, N.Jr., "Atom diffusion and impurity-induced layer disordering in quantum well III-V semiconductor heterostructures", J. Appl. Phys., Vol. 64, pp. R93-R111, 1988.
 30. Davey, S.T., Scott, E.G., Wakefield, B., and Davies, G.J., "Characterization of GaInAs/AlInAs multiple quantum wells by Raman scattering", Semicond. Sci. Technol., Vol. 2, pp. 683-686, 1987.
 31. Drummond, T.J., Gourley, P.L., and Zipperian, T.E., "Quantum-tailored solid-state devices", IEEE Spectrum June 1988, pp. 33-37.
 32. Devine, R.L.S., and Moore, W.T., "Extrinsic photoluminescence from InGaAs/GaAs pseudomorphic single quantum wells", Solid-State. Comm. Vol. 65, pp. 19-21, 1988.
 33. Dumond, W.M., Jesse, "Theory of the use of more than two successive X-ray crystal reflections to obtain increased resolving power", Phy. Rev., Vol. 52, pp. 872-883, 1937.
 34. Daniel, C. Bertlet, Jung-Kuei Hsu, and Kei May Lau, "Tailoring of hole eigenenergies in strained GaAsP/AlGaAs single quantum wells grown by MOCVD", Appl. Phys. Lette., Vol. 53, pp. 2501-2503, 1988.

35. Epelboin, Y., Riglet, P., "Boundary conditions in the numerical integration of Takagi-Taupin equations", Phys. Stat. Solidi (a), Vol. 54, pp. 547-556, 1979.
36. Esaki, L., "A bird's eye view on the evolution of semiconductor superlattices and quantum wells", IEEE J. Quant. Electro. Vol. QE-22, pp. 1611-1624, 1986.
37. Eer Nisse, E.P., Journal of Applied Physics, Vol. 45, pp. 167-171, 1974.
38. Fritz, J., Dawson, L.R., Osbourn, G.C., Gourley, P.L., and Biffeld, R.M., 10th International Symposium on GaAs and Related Compounds, Inst. Phys. Conf. Ser. vol. 65, pp. 241-250, 1982.
39. Fewster, P.F., and Curling, C.J., "Composition and lattice-mismatch measurement of thin semiconductor layers by X-ray diffraction", J. Appl. Phys., Vol. 62, pp. 4154-4158, Nov. 1987.
40. Fleming, R.M., Wcwhan, D.B., Gossard, A.C., Wiegmann, W., and Logan, R.A., "X-ray diffraction study of interdiffusion and growth in $(\text{GaAs})_n (\text{AlAs})_m$ multilayers", J. Appl. Phys., Vol. 51, p. 357, 1980.
41. Fritz, I.J., Picraux, S.T., Dawson, L.R., Drummond, T.J., Laidig, W.D., and Anderson, N.G., "Dependence of critical layer thickness on strain for InGaAs/GaAs SLS", Appl. Phys. Lett. Vol. 46, p. 967, 1985.

42. Fukui, T., and Saito, H., "(InAs), (GaAs), Layered crystal grown by MOCVD", Jpn. J. Appl. Phys., Vol. 23, pp. 1521-23, 1984.
43. Fekete, D., Chan, K.T., Ballantyne, J.M. and Eastman, L.F., "Graded index separate confinement InGaAs/GaAs strained layer quantumwell laser grown by MOCVD", Appl. Phys. Lett. Vol. 49, pp. 1659-1660, 1986.
44. Feng, M., Cook, L.W., Tashima, M.M., Stillman, G.E., and Blattner, R.J., "Auger profile study of the influence of lattice mismatch on the InGaAsP/InP heterojunction interface", Appl. Phys. Lett., Vol. 34, pp. 697-699, 1979.
45. Fujii, T., Hiyamizu, S., Yamakoshi, S., and Ishikawa, T., "MBE growth of extremely high quality GaAs-AlGaAs GRIN-SCH lasers with a superlattice buffer layer", J. Vac. Sci. Technol. B., Vol. 3, pp. 776-778, 1985.
46. Gourley, P.L., Biefeld, R.M., and Zipperian, T.E., "Single crystal optical interference filters and integrated high reflector/photodiode using multilayers of GaP and GaAsP", Appl. Phys. Lett., Vol. 49, pp. 242-244, Aug. 1986.
47. Gourley, P.L., and Biefeld, R.M., "Growth and photoluminescence characterization of a GaAsP/GaP strained-layer superlattice", J. Vac. Sci. Technol., Vol. 21, pp. 473-475, Aug. 1982.

48. Givens, M.E., Coleman, J.J., Zmudzinski, C.A., Bryan, R.P., Emanuel, M.A. and Milelr, L.M., "The effect of various buffer-layer structures on the material quality and dislocation density of high composition AlGaAs laser material grown by metalorganic chemical vapour deposition", J. Appl. Phys., Vol. 63, pp. 5092-5097, May 1986.
49. Gourley, P.L., Hohimer, J.P., and Biefeld, R.M., "Lasing transitions in GaAs-GaAsP SLS with $x=0.1-0.5$ ", Appl. Phys. Lett., Vol 47, 0. 582, 1985.
50. Gosel, U., and Morehead, F., "Diffusion....", J. Appl. Phys., Vol 52, pp. 4617, 1981.
51. Halliwell, M.A.G., Lyons, M.H. and Hill, M.J., "The interpretation of X-rays rocking curves from III-V semiconductor device structures", J. Cryst. Growth., Vol. 68, pp. 523-531, 1984.
52. Hearne, M.T., Rogers, T.G., and Tuck, B., "Exact solutions for substitutional-interstitial diffusion in semiconductors", Semicond. Sci. Technol., Vol. 3, pp. 456-460, 1988.
53. Hirayama, Y., Horikoshi, Y., and Okamoto, H., "Interdiffusion of Al and Ga in Si-implanted GaAs-GaAl superlattices", Jpn. J. Appl. Phys., Vol. 23, pp. 1568-1572, Dec. 1984.

54. Hetherington, C.J.D., Barry, J.M., Humphreys, C.J., Grange, J., and Wood, C., "High resolution electron microscopy of semiconductor quantum well structures", Materials Research Society, Boston, 1984.
55. Hill, M.J., Tanner, B.K., Halliwell, M.A.G., and Lyons, M.H., "Simulation of X-ray Double-Crystal Rocking Curves of Multiple and Inhomogeneous Heteroepitaxial Layers", J. Appl. Cryst., Vol. 18, pp. 446-451, 1985.
56. Halliwell, M.A.G., Juler, J., and Norman, A.G., "Measurement of grading in heteroepitaxial layers", Inst. Phys. Conf. Ser. No. 67, pp. 365-370, IOP, 1983.
57. Halliwell, M.A.G., Lyons, M.H., Tanner, B.K. and Ilczyszyn, P., "Assessment of epitaxial layers by automated scanning double axis diffractometry", Journal of Cryst. Growth, Vol. 65, pp. 672-678, 1983.
58. Holonyak, N.Jr., Kolbas, R.M., Dupuis, R.D., and Dapkus, P.D., "Quantumwell heterostructure lasers", IEEE Quantum Elect., Vol. QE-16, pp. 170-186, 1980.
59. Horning, R.D. and Staudenmann, J.L., "X-ray vibrational studies on (100) oriented CdTe crystals as a function of temperature (8-350K)", Phy. Rev.B, Vol. 34, pp. 3970-3979, 1986.
60. Imai, A., Kobayashi, M., Dosho, S., Kongai, M., and Takahashi, K., "Interdiffusion in ZnSe-ZnTe strained-layer super-

- lattices", J. Appl. Phys., Vol. 64, pp. 647-650, July 1988.
61. Ibers, J.A., and Hamilton, W.C., eds. International Tables for X-ray crystallography, Vol. IV, Kynoch, Birmingham, England, 1974.
 62. Ishibashi, T., Suzuki, Y., Okamoto, H., "Photoluminescence of an AlAs/GaAs superlattice Growth by MBE in the 0.7-0.8 μm wavelength region", Jpn. J. Appl. Phys., Vol. 20, pp. L623-L626, Sept. 1981.
 63. Imanaka, K., Sato, F., Imamoto, H., and Shimura, M., "High-Efficiency Laser with Strained Superlattice Buffer Layer", IEEE Photonics Technol. Lett., Vol. 1, pp. 8-10, 1989.
 64. Iikawa, F., Motisuke, P., Cerdeira, F., Socilotti, M.A., Musut, P.A., and Roth, A.P., "Effects of thermal annealing on the confined electronic states of $\text{In}_x\text{Ga}_{1-x}\text{As}/\text{GaAs}$ strained-layer-superlattices", Superla-Microst., Vol. 5, pp. 273-278, 1989.
 65. Itaya, A., Suematsu, Y., Katayama, S., Kishino, K., and Arai, S., "Low threshold current density (100) GaInAsP/InP DH lasers for wavelength 1.3 μm ", Jpn. J. Appl. Phys., Vol. 18, pp. 1795-1800, 1979.
 66. Joncour, M.C., Charasse, M.N., and Burgeat, J., "X-ray diffraction studies of thermal treatment of GaAs/InGaAs strained superlattices", J. Appl. Phys., Vol. 58, pp. 3373-3376, Nov. 1985.

67. Joseph,A., Philip,B., "Reflectance and Phase Envelops of an Iterated Multilayer", J. Opti. Soc. America, Vol. 56, pp. 1760-1762, Dec. 1966.
68. James,R.W., "The optical principles of the diffraction of X-rays", G.Bell and Sons Ltd., London 1967.
69. Jusserand,B., and Sapriel,J., "Raman investigation of anharmonicity and disorder-induced effects in $\text{Ga}_{1-x}\text{Al}_x\text{As}$ epitaxial layers", Phys. Rev. B. Vol. 24, pp. 7194-7205, 1981.
70. James,F. Smith, and David,C.H., "Thin Film Characterization", Solid State Technology, Nov. pp. 135-140, 1986.
71. Jou,M.J., Cherng, Y.T., and Stringfellow,G.B., "Organometallic vapour-phase epitaxial growth and characterization of metastable alloy 'InPSb"', J. Appl. Phys., Vol. 64, pp. 1472-1475, 1988.
72. K.Oe., Shinoda,Y., and Sugiyama,K., "Lattice deformations and misfit dislocations in InGaAsP/InP double-heterostructure lasers", Appl. Phys. Lette., Vol. 33, pp. 962-964, 1978.
73. Koren,U., Miller,B.I., Tucker,R.S., Eisenstein,G., Bar-Joseph,I., Miller,D.A.B., and Chemla,D.S., "High frequency InGaAs/InP multiple quantumwell buried-mesa electroabsorption optical modulator", Elec. Lett. Vol. 23, pp. 621-622, 1987.

74. Kaliski, R.W., Nam, D.W., Deppe, D.G., Holonyak, N.Jr., Hsieh, K.C., and Burnham, R.D., "Thermal annealing and photoluminescence measurements on AlGaAs-GaAs quantum-well heterostructures with Se and Mg sheet doping", J. Appl. Phys., Vol. 62, pp. 998-1005, August 1987.
75. Kawabe, M., Matsuura, N., Shimizu, N., Hasegawa, F., and Nannichi, Y., "Disordering of Si-doped AlAs/GaAs Superlattice by Annealing", Jpn. J. Appl. Phys., Vol. 23, L623-L624, Aug. 1984.
76. Kervarec, J., Baudet, M., Caulet, J., Auvray, P., Emery, J.Y., and Regreny, A., "Some Aspects of the X-ray Structural Characterization of GaAlAs/GaAs superlattices", J. Appl. Cryst., Vol. 17, pp. 196-205, 1984.
77. Karnigaki, K., Sakashita, H., Kato, H., Nakayama, M., Sano, N., and Terauchi, H., "X-ray diffraction analysis of buffer layer effects on lattice dislocation of strained layer superlattices", J. Appl. Phys., Vol. 62, pp. 1124-1127, Aug. 1987.
78. Kubota, K., Ohnishi, T., and Shiimoto, T., "Current oscillation in modulation-doped GaInAs/n-GaAs strained-layer superlattices", J. Appl. Phys., Vol. 58, pp. 2402-2403, 1985.
79. Kato, N., "Pendellosung Fringes in Distorted Crystals I. Fermat's Principle for Bloch Waves", Jpn. J. Phys. Soc., Vol. 18, pp. 1785-1791, 1963.

80. Katsuyama, T., Yang, Y.J., and Bedair, S.M., "Lifetime test for high current injection strained layer superlattice light emitting diode", IEEE Elect. Dev. Lett., Vol. EDL-8, pp. 240-242, 1987.
81. Koren, U., Koch, T.L., Presting, H., and Miller, B.I., "InGaAs/InP multiple quantum well waveguide phase modulator", Appl. Phys. Lett., Vol. 50, pp. 368-370, 1987.
82. Larson, B.C. and Barhorst, J.F., "X-ray study of lattice strain in boron implanted laser annealed silicon", J. Appl. Phys., Vol. 51, pp. 3181-3185, June 1980.
83. Laidig, W.D., Holonyak, N., J.R., Coleman, J.J. and Dapkus, P.D., "Induced disorder of AlAs-AlGaAsGaAs quantum-well heterostructures", J. Electro. Mate. Vol. 11, pp. 1, Jan. 1982.
84. Laidig, W.D., Holonyak, N.Jr., and Camras, M.D., "Disorder of an AlAs-GaAs superlattice by impurity diffusion", Appl. Phys. Lett., Vol. 38, pp. 776-778, May 1981.
85. Laidig, W.D., Lee, J.W., Chiang, P.K., Simpson, L.W., Bedair, S.M., "Disorder of an InGaAs-GaAs superlattice by Zn diffusion", J. Appl. Phys., Vol. 54, pp. 6382-6384, Nov. 1983.
86. Leonard, R., Weisberg, and Joseph, B., "Diffusion with Interstitial Substitutional Equilibrium, Zinc in GaAs", Phy. Rev. Vol. 131, pp. 1548-1552, 1963.

87. Lee, K.H., Park, H.H. and Stevenson, D.A., "Impurity diffusion enhancement of interdiffusion in an InGaAsP-GaAs heterostructure", J. Appl. Phys. Vol. 65, pp. 1048-1051, Feb. 1989.
88. Logini, R.L., "Diffusion mechanism", Solid. State. Elect., Vol. 5, pp. 127-138, 1962.
89. Laidig, W.D., Caldwell, P.J., Lin, Y.F., and Peng, C.K., "Strained-layer quantumwell injection lasers", Appl. Phys. Lett., Vol. 44, pp. 653-655, 1984.
90. Laidig, W.D., Peng, C.K. and Lin, Y.F., "Effects of strain and layer thickness on the growth of InGaAs-GaAs strained layer superlattices", J. Vac. Sci. Technol., Vol. B2, pp. 181-185, 1984.
91. Myers, D.R., Picraux, S.T., Doyle, B.L., Arnold, G.W., and Biefeld, R.M., "Characterization of ion-implantation doping of strained-layer superlattices. I. structural properties", J. Appl. Phys., Vol. 60, pp. 3631-3640, Nov. 1986.
92. Macrander, A.T., Mimami, E.R., and Berreman, D.W., "Dynamical X-ray rocking curve simulations of nonuniform InGaAs and InGaAsP using Abeles matrix method", J. Appl. Phys., Vol. 60, pp. 1364-1368, Aug. 1986.
93. Meehan, K., and Holonyak, N.Jr., "Wavelength modification of room temperature continuous quantum-well heterostructure laser diodes by thermal annealing", J. Appl. Phys., Vol. 54, pp. 7190-7191, Dec. 1983.

94. Macrander, A.T., Schwartz, G.P. and Gualtieri, G.J., "X-ray and Raman characterization of AlSb/GaSb strained layer superlattices and quasiperiodic Fibonacci lattices", J. Appl. Phys., Vol. 64, pp. 6733-6744, 1988.
95. Moroni, D., Dupont-Nivet, E., Andre, J.P., and Potillon, J.N., "Optical studies of misfit strain effects in GaInP epitaxial layers on (001) GaAs substrate", J. Appl. Phys., Vol. 63, pp. 5188-5190, 1988.
96. Makita, K., and Taguti, K., "Crystallinity and interdiffusion in InP/InGaAs quantum wells grown by hybride VPE", Superlattices and micro., Vol. 4, pp. 101-106, 1988.
97. Moon, R.L., Antypas, G.A., and James L.W., "Band gap lattice constant of GaInAsP as a function of alloy composition", J. Electro. Mate., Vol. 3, pp. 635-644, 1974.
98. Naokatsu, S., Hiromu, K., Masaaki, N., Shigeaki, C., and Hikaru, T., "Mono and Bilayer superlattices of GaAs and AlAs", Jpn. J. Appl. Phys., Vol. 23, pL640-41, 1984.
99. Nakajima, K., Yamaguchi, A., Alata, K., and Kotani, T., "Composition dependence of the band gap of InGaAsP quaternary solids lattice matched on InP substrates", J. Appl. Phys. Vol. 49, pp. 5944-5950, 1978.
100. Nahory, R.E., Pollack, M.A., Johnston, W.D., Jr., and Barns, R.L., "Band gap versus composition and demonstration

- lattice emitter", *Electro. Lett.*, Vol. 23, pp. 936-938, Aug. 1987.
109. Pamulapati, J., Oh, J.E., Debbar, N., and Bhattacharya, P., "A critical examination of the MBE growth of $\text{In}_x\text{Ga}_{1-x}\text{As}/\text{GaAs}$ strained quantum well structures", *J. Appl. Phys.*, Vol. 65, pp. 1361-1363, Feb. 1989.
110. Ploog, K., "Molecular Beam Epitaxy of III-V compounds", in *Crystal/Growth, Properties, and Applications*, L.F. Boschke, ed., Springer-Verlag, Heidelberg, W.Germany, 1979.
111. Pape, I.J., Likam Wa P., David, J.P.R., Claxton, P.A. and Robson, R.N., "Disordering of GaInAs/InP multiple quantum well layers by sulphur diffusion", *Electron. Lett.*, Vol. 24, pp. 1217-18, 1988.
112. Pavesi, L., Martelli, F., Martin, D., and Reinhart, F.K., "Photoluminescence enhancement in post growth hydrogenated GaAlAs and GaAs/GaAlAs multilayer structures", *Appl. Phys. Lett.*, Vol. 54, pp. 1522-1524, 1989.
113. Plano, W.E., Nam, D.W., Major, J.S.Jr., Hsieh, K.C., and Holonyak, N.Jr., "Column III and V ordering in InGaAsP and GaAsP grown on GaAs by MOCVD", *Appl. Phys. Lett.*, Vol. 53, pp. 2537-2539, 1988.
114. Quillec, M., Goldstein, L., Le Roux, G., Burgeat, J., and Primot, J., "Growth conditions and characterization of InGaAs/GaAs strained layers superlattices", *J. Appl. Phys.* Vol. 55, pp. 2804-2808, Aug. 1984.

115. Richardson, J.H., "Optical microscopy for the materials sciences", Marcel Dekker Inc., N.Y. 1971.
116. Razegi, M., Acher, O., and Launay, F., "Disorder of a GaInAsP-InP quantum well by Zn diffusion", *Semicond. Sci. Technol.*, Vol. 2, pp. 793-796, 1987.
117. Reynolds, S., Vook, D.W., and Gibbons, J.F., "Open tube Zn diffusion in GaAs using diethylzinc and trimethylarsenic: Experimental and model", *J. Appl. Phys.*, Vol. 63, pp. 1052-1059, Feb., 1988.
118. Razeghi, M., Duchemin, J.P., "Low pressure-MOCVD growth of GaInAs-InP heterojunction and superlattices", *J. Vac. Sci. Technol. B* 1(2), pp. 262-265, Apr. 1983.
119. Rosenberg, J.J., Benlamri, M., Kirchner, P.D., Woodall, J.M., and Pettit, G.D., "An InGaAs/GaAs pseudomorphic single quantum well HEMT", *IEEE Elect. Dev. Lett.*, Vol. EDL-6, pp. 491-493, 1985.
120. Ramdas, A.K., "Modulation photoluminescence, and Raman spectroscopy of semiconductor heterostructures", *Superlattices and Microstruc.*, Vol. 4, pp. 69-76, 1988.
121. Razeghi, M., Omnes, F., Defour, M., and Maurel, Ph., "High quality GaInAsP/InP heterostructures grown by low-pressure metalorganic chemical vapour deposition on silicon substrate", *Appl. Phys. Lett.*, Vol. 52, pp. 209-211, 1988.,

122. Renter,W., "Electron probe microanalysis", Surface Science, Vol. 25, p. 80-120, 1971.
123. Speriosu,V.S., "Kinematical X-ray diffraction in nonuniform crystalline films : Strainand damage distribution in ion implanted garnets", J. Appl. Phys., Vol. 52, pp. 6094-6103, Oct. 1981.
124. Speriosu,V.S., and Vreeland,T.Jr., "X-ray rocking curve analysis of superlattices", J. Appl. Phys., Vol. 56, pp. 1591-1600, Sept. 1984.
125. Swaminathan,S., "Ph.D. Thesis, Department of Engineering University of Warwick, Coventry, U.K., 1985.
126. Speriosu,V.S., Paine,B.M., and Nicolet,M.A., "X-ray rocking curve study of Si-ionimplanted GaAs, Si and Ge", Appl. Phys. Lette., Vol. 40, p. 604, 1982.
127. Seki,H.,and Koukitu,A., "Thermodynamic analysis of molecular beam epitaxy of III-V semiconductors", J. Cryst. Growth, Vol. 78, pp. 342-352, 1986.
128. Shrivastava,M.C., and Swaminathan, S., "SEM study of thermal degradation of indium phosphide", Microelectronics Journal (U.K.), Vol. 19, No. 1, p. 48-51, 1988.
129. Shrivastava,M.C., and Swaminathan,S., "Characterization of InGaAs/GaAs superlattice structures by X-ray double

- crystal diffraction", *Microelectronics Journal* (U.K.), Vol. 19, No. 5, p. 29-33, 1988.
130. Swaminathan, S., and Shrivastava, M.C., "Modelling of annealing effects on III-V semiconductor superlattices", National seminar on GaAs and III-V compound semiconductors, held at I.I.T. Kharagpur during 29-30, April 1988, p. 5.5.
131. Swaminathan, S., and Shrivastava, M.C., "Rocking curve simulation of thermally annealed and Zn diffused InGaAs/GaAs superlattice structures", International conference and intensive tutorial course on semiconductor materials, held during 8-16 December 1988 Delhi University, Delhi.
132. Shrivastava, M.C., and Swaminathan, S., "Interdiffusion in InGaAs-GaAs strained layer superlattices", 17th Yugoslav Conference on microelectronics, Nis, Yugoslavia, May 9-11, 1989 (accepted for presentation).
133. Shrivastava, M.C., and Swaminathan, S., "Characterization of Be-implanted GaAsP/GaP strained layer superlattice structure", *Thin Solid Films* (U.K.) (revised and submitted).
134. Shrivastava, M.C., and Swaminathan, S., "Abeles'-Takagi approach for dynamical X-ray rocking curve analysis of superlattice structures", *Semiconductor Science and Technology* IOP (U.K.), Vol. 4, pp. 495-497, 1989.

135. Shrivastava, M.C., and Swaminathan, S., "Three crystal X-ray scan simulation of superlattice structures using Abeles-Takagi dynamical approach", *Electro. Lett.*, Vol. 25, No. 14, 1989.
136. Dingle, R., Stomer, H., Gassard, A.C., and Wiegmann, W., "High mobility.....", *Appl. Phys. Lett.*, Vol. 33, pp. 665-671, 1978.
137. Cho, A.Y., "Recent Developments in MBE", *J. Vacu. Sci. Technol.* Vol. 16, pp. 275-278, 1979.
138. Tell, B., Leheny, R.F., Lio, A.S.H., Bridges, T.J., Burkhardt, E.G., Chang, T.Y., and Beebe, E.D., "Beryllium implantation doping of InGaAs", *Appl. Phys. Lett.*, Vol. 44, pp. 438-440, Feb. 1984.
139. Tuck, B., "Some explicit solutions to the nonlinear diffusion equation", *J. Phys. D : Appl. Phys.* Vol. 9, pp. 1559-1569, 1976.
140. Topper, L., and Ploog, K., "Improved assessment of structural properties of AlGaAs/GaAs heterostructures and superlattices by double crystal X-ray diffraction", *Phy. Rev. B*, Vol. 33, pp. 5565-5575, Apr. 1986.
141. Takagi, S., "A dynamical theory of diffraction for a distorted crystal", *J. Phy. Soc. Japan*, Vol. 26, pp. 1239-1253, May 1969.

142. Takeuchi, T., Ohta, N., Sugita, Y., and Fakuwara, A., "Determination of strain distribution in ion-implanted magnetic bubble garnets applying X-ray dynamical theory", *J. Appl. Phys.* Vol. 54, pp. 715-721, 1983.
143. Taupin, D., *Bull. Soc. Franc. Miner. Crystallogr.* Vol. 87, pp. 469-473, 1964.
144. Tanner, B.K., and Bowen, D.K., "Characterization of crystal Growth Defects by X-ray Methods", Plenum, N.Y., p. 474, 1980.
145. Tadashi, M., "A method of obtaining a highly parallel and monochromatic X-ray beam by successive diffraction", *J. Appl. Cryst.*, Vol. 7, pp. 254-259, 1974.
146. Vandenberg, J.M., Hamm, R.A., Panish, M.B., and Temkin, H., "High resolution X-ray diffraction studies of InGaAs(P)/InP superlattices grown by gas-source molecular-beam epitaxy", *J. Appl. Phys.*, Vol. 62, pp. 1278-1283, Aug. 1987.
147. Van Gorp, G.J., Van Dongen, T., Fontijn, G.M., Jacobo, J.M., and Tjaden, D.L.A., "Interstitial and substitutional Zn in InP and InGaAsP", *J. Appl. Phys.*, Vol. 65, pp. 553-560, 1989.
148. Wada, O., Sanada, T., Nobuhara, N., Kuno, M., Makiuchi, M., and Fujii, T., "Very low threshold current AlGaAs/GaAs quantum lasers suitable for optoelectronic integration",

- Instt. Phys. Conf. Ser. No. 79, pp. 685-690, 1986.
149. Wie, C.R., Tombrello, T.A., and Vreeland, T.Jr., "Dynamical X-ray diffraction from nonuniform crystalline films : Application to X-ray rocking curve analysis", J. Appl. Phys., Vol. 59, pp. 3743-3746, June 1986.
150. Watt, M., Sotomayor, C.M., Halton, P.D., Vass, H., Claxton, P. A., and Roberts, J.S., "Raman scattering from GaInAs-InP quantum well structures", Superlattices and Microstructures, Vol. 3, pp. 75-78, 1987.
151. Wood, T.H., Burrus, C.A., Miller, D.A.B., Chenla, D.S., Damen, T.C., Gossard, A.C., and Weigmann, W., "High speed optical modulation with GaAs/GaAlAs QW in p-i-n diode structure", Appl. Phys. Lett., Vol. 44, pp. 16-18, 1984.
152. Zachariasen, W.H., Theory of X-ray Diffraction in Crystals
Dover, New York, 1967.
153. Matthew, J.W. and Blakeslee, A.E., "Defects in epitaxial multilayers", J. Cryst. Growth, Vol. 27, pp. 118-122, 1974.
154. Black, J.F., Summers, C.J., and Sherman, B., "Spatial variation of radiative recombination in GaAsP wafer revealed by photoluminescence image", Appl. Phys. Lett., Vol. 19, pp. 28-35, 1971.

PUBLICATIONS

1. Shrivastava M.C., and Swaminathan S., "Characterization of InGaAs/GaAs superlattice structures by X-ray double crystal diffraction", Microelectronics Journal (U.K.), Vol.19, No.5, pp. 29-33, 1988.
2. Swaminathan S., and Shrivastava M.C., "Rocking curve simulation of thermally annealed and Zn diffused InGaAs/GaAs superlattice structures", International conference and intensive tutorial course on semiconductor materials, held during 8-16 December 1988, Delhi University, Delhi.
3. Shrivastava M.C., and Swaminathan S., "Abeles'-Takagi approach for dynamic X-ray rocking curve analysis of superlattice structures", Semiconductor Science and Technology IOP (U.K.), Vol.4, pp. 495-497, 1989.
4. Shrivastava M.C., and Swaminathan S., "Three crystal X-ray scan simulation of superlattice structures using Abeles-Takagi dynamic approach", Electro. Lett. (U.K.), Vol.25, pp. 933-934, 1989.
5. Shrivastava M.C., and Swaminathan S., "Interdiffusion in InGaAs-GaAs strained layer superlattices", 17th Yugoslav Conference on Microelectronics, Nis. Yugoslavia, May 9-11, 1989.
6. Shrivastava M.C., and Swaminathan S., "Characterization of Be-implanted GaAsP/GaP strained layer superlattice structure", Thin Solid Films(U.K.) (revised and submitted).



- of Vegard's law for InGaAsP lattice matched to InP", Appl. Phys. Lett., Vol. 33, pp. 659-661, 1978.
101. Osbourn, G.C., Biefeld, R.M. and Gourley, P.L., "A GaAsP/GaP strained layer superlattice", Appl. Phys. Lett., Vol. 41, pp. 172-174, July 1982.
 102. Osbourn, G.C., "Strained-layer superlattices from lattice mismatched materials", J. Appl. Phys., Vol. 53, pp. 1586-1589, March 1982.
 103. Osbourn, G.C., "Strained-layer superlattices : A brief review", IEEE J.Q.E. Vol. QE-22, pp. 1677-1681, 1986.
 104. Olsen, G.H., "Vapour phase growth of (In,Ga) (As,P) Quaternary Alloys", IEEE J. Quantum Electronics, Vol. QE-17, pp. 128-132, 1981.
 105. Oatley, C.W., "Scanning Electron Microscopy", Cambridge University Press, (UK), 1972.
 106. Paine, B.M., Hurvitz, N.N. and Speriosu, V.S., "Strain in GaAs low-dose ion implantation", J. Appl. Phys., Vol. 61, pp. 1335-1338, Feb. 1987.
 107. Pearsall, T.P., "GaInAsP alloy semiconductors", John Wiley & Sons, N.Y. 1982.
 106. Palmier, J.F., Sibille, A., Harmand, J.C., Dangla, J., "AlGaAs/GaAs bipolar transistors with a modulation-doped super-